UNIVERSITÀ DEGLI STUDI DI PALERMO

PhD program in "*Technology and Science for Human Health*"

Department of Health Promotion, Mother and Child Care, Internal Medicine and Medical Specialties

University of Palermo.

Biomechanical analysis of Ascending Thoracic Aortic Aneurysm (ATAA)

PhD CANDIDATE
Federica Cosentino, MS

MENTOR
Prof. Maurizio Leone

PhD PROGRAM COORDINATOR
Prof. Maurizio Leone

TUTORS
Prof. Salvatore Pasta
Prof. Gaetano Burriesci

XXXIII
2019/2020

Credo ut intelligam.

> *"For I do not seek to understand in order that I may believe, but I believe in order to understand. For this also I believe - that unless I believe I shall not understand*."

St. Anselm of Canterbury

Colossians 1:9-14

Philippians 2:12-14

Philippians 4:11-12

Acknowledgement

With my ultimate gratitude, I surrender this work to *God*, who is the source of my knowledge and strength. I sincerely appreciate the almighty God for His grace, strength, sustenance. Above all, I am grateful for the faithfulness and love that He gave to me from the beginning of my academic life up to this doctoral level. Thank you, *God*, for your protection.

I would like to thank all of the people who have contributed to my PhD work.

First, I would like to thank my supervisor, *Prof. Salvatore Pasta*, for his support. I would also like to thank my committee members, *Prof. Maurizio Leone* and *Prof.ssa Valeria Vetri* for their instructive advice, useful suggestions and their patience during the revision and improvement on my thesis.

I would like to extend my gratitude to *Prof. Antonio D'Amore* for accepting to be the reviewer of my thesis. I would like to thank you for encouraging my research and for allowing me to grow as a research scientist.

I have to thank the Institute of Biomechanics in Graz, for the opportunity of writing part of my thesis. Especially, I am glad for the trust of *Prof. Gerhard A. Holzapfel,* that is of great importance for me and deserves a special mention in these acknowledgements. The continuum mechanics and constitutive modelling fields are an extraordinary interesting at the Institute of Biomechanics, and I had been really happy to part of this fantastic department.

Mom and *Dad* thank you for always being a great example of hard work and determination. Your guidance helped me very much, and without it, I would never have finished - or even started - this work. Thank you for your constant love and encouragement, I know it was not easy to watch me move to another country. You have given me unwavering support in every

possible way. This work is the culmination of all the effort you put into my education throughout the years, for which I am eternally grateful.

Thank you, *Brother*. You ask me the right questions, you see solutions which I cannot. You have given me the necessary relaxing moments, the critical reflections and objective attitude to stay motivated and focused until finishing this thesis.

I would like to thank all my friends, in particular, *Emanuela, Laura, Francesca* with whom I have shared moments of deep anxiety but also of big excitement. Their presence was very important in this process. A warm word for my colleague and great friend *Arianna*, that always managed to make me feel special and who has always been a great source of support when I was very discouraged.

Last but not least, I may also thank my lovely boyfriend *Andrea*. All the words you say and all the things you do make me a better person. You have journeyed with me through the stresses and joys of qualifying exams, conferences, publications, and finally, my thesis and defence. Most of these required late nights and early mornings, resulting in time away from you, especially during this final year. Thank you not only for your understanding but especially for your persistence and unchanging support. I could not be more grateful to have you by my side during this season of my life. This work would not be what it is without you.

Abstract

According to the reports of the World Health Organisation (WHO), cardiovascular diseases are the number one cause of death worldwide. Specifically, arterial disease and degeneration are the major reasons for cardiovascular death and disability. Because these diseases are dependent on the changes of the mechanical properties of the arterial wall, it is very important to know as much as possible about the structural composition of arteries.

The human aorta is the biggest artery in the body and consists of three main parts, ascending aorta, aortic arch and descending aorta. The walls of the arteries consist of three layers, the intima, media and adventitia, where each of the layers has different physiological functions and therefore distinct mechanical properties. These were investigated using, i.e., uniaxial tensile, inflation or planar biaxial-testing.

Purpose of this thesis was to apply the biomechanical approach by mean of numerical and experimental test referring to patient-specific aortic geometries with ascending thoracic aortic aneurysms. However, despite the ample literature and the related scientific and industrial activity in this field, many different phenomena are not yet consolidated.

The PhD Thesis is then divided into two main sections: the first is composed by a brief introduction on ATAA, with some background about mechanical properties of soft tissues, the evolution of the constitutive model, some remarks of the continuum. The second section of the thesis is based on the different research activities developed during the PhD.

KEYWORDS: continuum mechanics; hyperelastic material; hyperelastic models; experimental identification, multiphoton imaging, Second-harmonic generation, fine element method.

.

Contents

List of Figures

List of Tables

1. Introduction and Motivation

1.1. Cardiovascular Disease

Cardiovascular disease (CVD) is the leading cause of death worldwide and is expected to account for more than 23 million deaths by 2030 [1]. Two of these diseases that occur in the thoracic aorta (TA), aneurysms (TAA) and dissections (TAD), are rare but life-threatening events with poorly understood pathophysiologies.

CVD is closely linked to health inequalities, with more CVD-related deaths in women than men, more CVD-related deaths in middle-income than high-income countries, and pronounced declines in coronary mortality in countries with the most advanced contemporary care. With the ageing population, CVD prevalence is expected to increase and often co-exist with other diseases, leading to multi-morbidity. Major risk factors for CVD including obesity and diabetes are becoming more prevalent.

CVD is also a heavy economic burden for both public and private institutions. By 2030, the total global cost of CVD is set to rise from approximately US$863 billion in 2010 to a staggering US$1,044 billion (World Heart Federation, 2020), (see Figure 1).

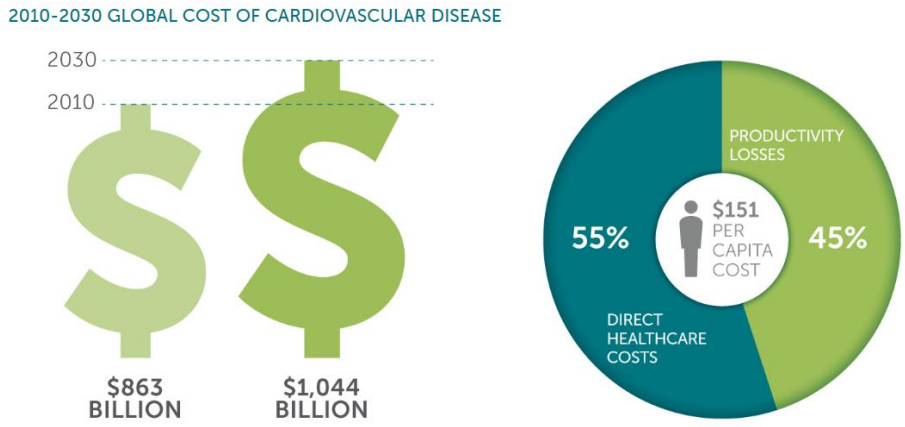

Figure 1 – The economic costs. Source: WEF/Harvard School of Public Health -The Global Economic Burden of Non-communicable Diseases

The projected increase in healthcare costs is illustrated in Figure 2, which displays the total healthcare costs from CVD for the period through to 2020. By the end of the decade, the six countries combined will face CVD-related healthcare costs of €98.7 billion. Hence, there is a rise in per capita costs in each of the individual countries. Sweden and Germany face a per capita cost of €455 and €417, respectively. Costs will also rise in Italy (€297), the UK (€264) and France (€244).

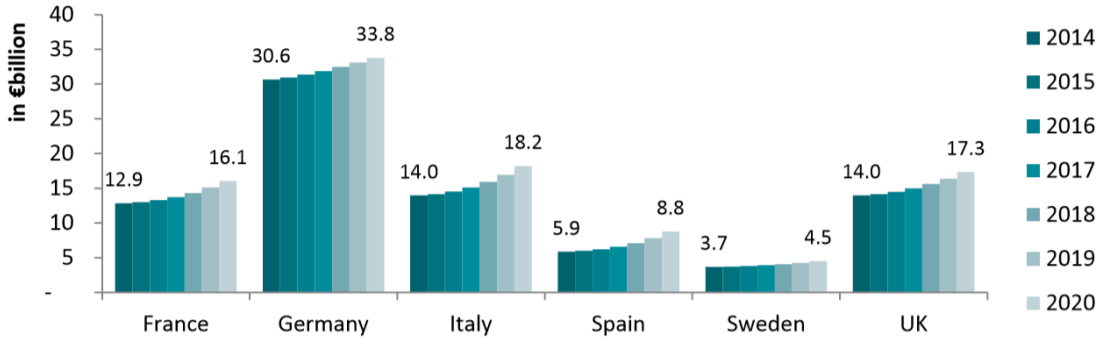

Figure 2 – Healthcare cost of CVD, forecast 2014-220, in £billion

Among the diseases affecting the cardiovascular system (CVS), it is possible to distinguish between those affecting the heart (i.e. cardiomyopathies, heart failure, heart valve diseases) and those affecting the aorta and the other vessels of the CVS (i.e. aortic aneurysm, aortic dissection, coronary artery diseases). Although many different diseases merit biomechanical study, here we simply list a few.

Atherosclerosis is characterized by a focal accumulation of lipids, extra cells and proteins, calcium, and necrotic debris within the intimal layer of arteries. In most cases, this accumulation causes a narrowing of the lumen (i.e., stenosis) which thereby compromises distal blood flow. One of the primary complications, however, is that atherosclerotic plaques can rupture and then clot - this can result in either the complete occlusion of the blood vessel or the shedding of a clot which occludes a smaller, distal vessel. Consequences can include myocardial infarction (heart attack) or stroke (brain attack).

Heart Failure is characterized by a marked decrease in cardiac output, increased venous pressures, or both; this results in elevated ventricular pressures that over distend the ventricles and thereby diminish their ability to pump blood. Heart failure is generally classified according to whether the right or left ventricle is affected. Left heart failure leads, for example, to pulmonary edema and hence breathlessness - sometimes called congestive heart failure.

Hypertension is defined as the persistent elevation of blood pressure. Normal systemic pressure is ≈ 120/80 mmHg (systolic/diastolic) and systemic hypertension is generally defined as pressures above 160/90 mmHg; pulmonary hypertension is generally defined as pressures above 30/12 mmHg. Hypertension may not have a known cause (called essential or idiopathic) or it may result from other diseases (then called secondary hypertension), such as renal, endocrine, or central nervous system diseases. The primary importance of hypertension is that it is a major risk factor for other, potentially fatal, diseases, including aneurysms, end-stage renal disease, stroke, sudden cardiac death, etc.

Myocardial Infarction, or heart attack, is defined as the death of myocardium (necrosis) due to a lack of oxygen (ischemia). If one survives a heart attack, the necrotic tissue is generally removed and replaced with a 'collagen patch', which in some cases may form an aneurysm. As noted above, atherosclerosis is the most common cause of heart attacks.

Stroke, strictly speaking, is any sudden or severe attack, as, for example, a sun-stroke or heat-stroke. Commonly, however, by the term stroke, we imply the death of a portion of the brain due to the lack of oxygen, and thus it is sometimes referred to as a brain attack in analogy with a heart attack. As noted above, strokes are often caused by the rupture and clotting of an atherosclerotic plaque. In addition, however, strokes may also be caused by the

shedding of an embolus from the heart or a proximal vessel or by the rupture of an intracranial malformation or aneurysm.

Valvular heart disease is any cardiovascular disease process involving one or more of the four valves of the heart (the aortic and mitral valves on the left side of the heart and the pulmonic and tricuspid valves on the right side of the heart). Often It is necessary for the surgical replacement of one of the heart valves; prosthetic heart valves are among the most successful implants in cardiovascular surgery.

Aneurysms are focal dilatations that result from a local weakening of a pressure distended organ. Within the vasculature, the two most common forms are abdominal aortic aneurysms (AAA), ascending thoracic aortic aneurysm (ATAA) and intracranial saccular aneurysms. These types of lesions have very different etiologies, the former often related to atherosclerosis and the latter not; both generally involve the proteolytic breakdown of portions of the extracellular matrix, however. When possible, AAAs are typically treated via the surgical replacement by a synthetic arterial graft; among many others, Albert Einstein died of a ruptured AAA.

Among these pathologies described above, the thesis concerns the biomechanics of aneurysm of the ascending thoracic aorta (ATAA).

A study from Olmsted County, MN,[2] demonstrated annual age- and sex-adjusted incidences per 100 000 people of 3.5 (95% CI, 2.2–4.9) for thoracic aortic aneurysm rupture and 3.5 (95% CI, 2.4–4.6) for acute aortic dissection [3]. The Global Burden of Disease Study 2016 used statistical models and data on incidence, prevalence, case fatality, excess mortality, and cause-specific mortality to estimate disease burden for 315 diseases and injuries in 195 countries and territories. The highest age-standardized mortality rates

attributable to aortic aneurysm are estimated for Northern and Eastern Europe, southern and tropical Latin America, and Oceania Figure 3.

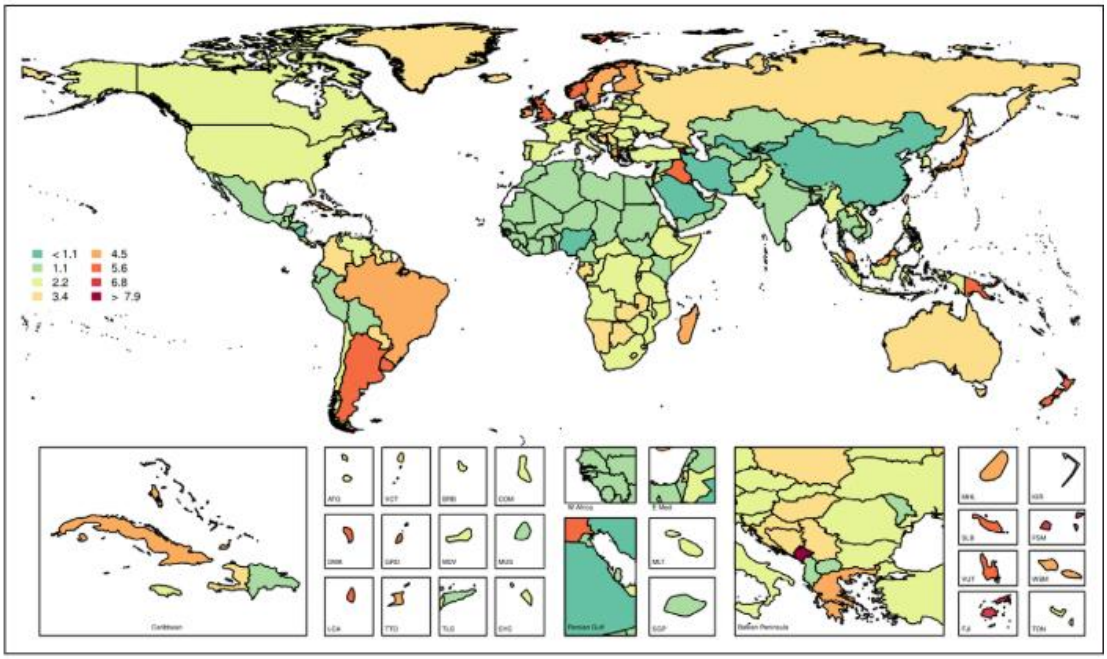

Figure 3 – Age-standardized prevalence of peripheral artery disease per 100 000, both sexes, 2016. Country. Source by E. Benjamin et al. [1]

1.2. Soft tissues

Biological tissues are roughly divided into: (i) *hard tissues* like bone and tooth, and (ii) *soft tissues* such as skin, muscle, blood vessel, and lung. Hard tissues contain mineral, whereas soft tissues do not. Because of this, they have very different mechanical properties.

One of the major differences in mechanical properties is that soft tissues are much more deformable than hard tissues. Therefore, infinitesimal deformation theories that are applied to metals and hard plastics cannot be used for soft tissues; instead, finite (large) deformation theories that are useful for rubber elasticity are often used to describe the mechanical behaviour of soft tissues [4]. This section deals with the basic mechanical properties of

biological soft tissues and their mathematical formulation, including several biomechanical features unique to soft tissues.

Soft connective tissues of our body are complex fibre-reinforced composite structures. Their mechanical behaviour is strongly influenced by the concentration and structural arrangement of constituents such as *collagen* and *elastin*, the hydrated *matrix of proteoglycans*, and the topographical site and respective function in the organism.

Collagen. Collagen is a protein which is very important for vertebrate physiology. It is a macromolecule with a length of about 280 nm. The rod-like shape of the collagen molecule comes from three polypeptide chains which are composed in a right-handed triple-helical conformation. Most of the collagen molecule consists of three amino acids; glycine (33%), which enhances the stability of the molecule, proline (15%) and hydroxyproline (15%). Collagen molecules are linked to each other by covalent bonds building collagen fibrils. Depending on the primary function and the requirement of the strength of the tissue the diameter of collagen fibrils varies (the order of magnitude is 1.5 nm; see Nimni and Harkness (1988) [5]). Collagen appears as concentrically arranged fibres in the structure of blood vessels. More than 12 types of collagen have been identified [6]. The most common collagen is type I, which can be isolated from any tissue. It is the major constituent in blood vessels. The intramolecular crosslinks of collagen give the connective tissues the strength, which varies with age, pathology, etc. They shrink upon heating due to breakdown of the crystalline structure (at 65 a C, for example, mammalian collagen shrinks to about one-third of its initial length, Fung (1993 [7]), p. 263). Collagen fibres represent the main load-carrying elements of arterial walls that render the material properties anisotropic.

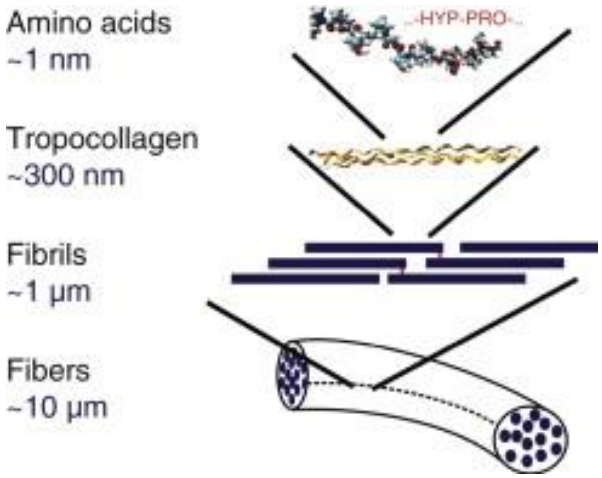

Figure 4 – Schematic view of the hierarchical features of collagen (Buehler 2008) [8]

Elastin. Elastin is another major component of certain soft tissues, such as arterial walls and ligaments. It is a protein, which is a major constituent of the extracellular matrix of connective tissue. It is present as thin strands in soft tissues such as skin, lung, ligamenta flava of the spine and ligamentum nuchae (the elastin content of the latter is about 5 times that of collagen). The long flexible elastin molecules build up a three-dimensional (rubber-like) network, which may be stretched to about 2.5 of the initial length of the unloaded configuration. In contrast to collagen fibres, this network does not exhibit a pronounced hierarchical organization. As for collagen, 33% of the total amino acids of elastin consist of glycine. However, the proline and hydroxyproline contents are much lower than in collagen molecules. The mechanical behaviour of elastin may be explained within the concept of entropic elasticity. Elasticity arises through entropic straightening of the chains, i.e. a decrease of entropy, or an increase of internal energy (see, for example [9, Ch. 7.1]). Elastin is essentially a linearly elastic material (tested for the ligamentum nuchae of cattle). It displays very small relaxation effects (they are larger for collagen).

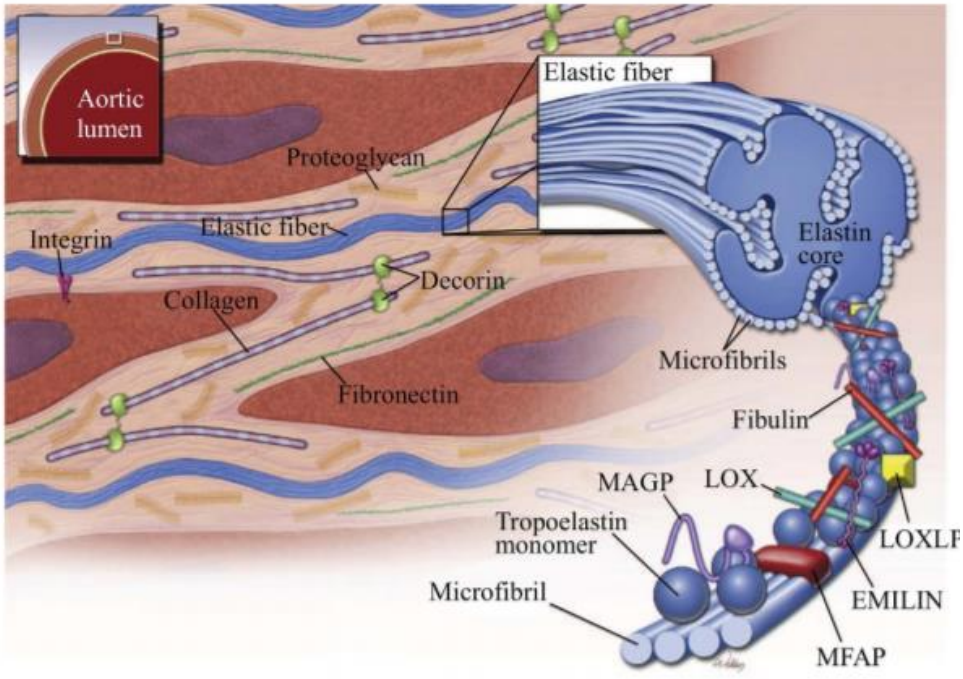

Figure 5 – Elastic fibre structure in the medial layer of the aorta: (a) elastin core consists of tropoelastin monomers connected by fibulins and cross-linked by lysyl oxidase (LOX) and lysyl oxidase-like protein (LOXLP). Microfibrils contain fibrillins, microfibril-associated glycoprotein (MAGP) and microfibril-associated protein (MFAP). The core is attached to microfibrils by elastin microfibril interface-located proteins (EMILINs) forming an elastic fibre; reprinted from [10]*, Copyright 2013)-*

Proteoglycans. PGs consist of GAGs that are linked to a core protein and are mainly found in the ECM although some PGs extend across the cell membrane or are directly attached to it by anchors [11]. GAGs are negatively charged and hydrophilic unbranched polysaccharide chains composed of repeating disaccharide units. They can be divided into four groups by their sugars and links between the sugars: (i) chondroitin sulfate and dermatan sulfate, (ii) heparan sulfate, (iii) keratan sulfate and (iv) hyaluronan (also known as hyaluronic acid or hyaluronate). PGs take part in ECM remodelling and cell adhesion-migration-proliferation by interacting with or functioning as cell surface receptors to growth factors, matrix remodelling enzymes and other ECM components [12]. PGs secreted by vascular endothelial cells can serve as structural organizers of the basal lamina by attaching to the other constituents or contribute to the selective filtration of the basal lamina. Proteoglycans can either promote or prevent processes depending on the type of cells they are interacting with and the

environment [12]. For example, vascular endothelial cells switch to synthesizing chondroitin sulfate/dermatan sulfate-based PG rich ECM from heparan sulfate-based PG rich ECM when cell migration is induced [13]. Although its role in the aortic wall remains unclear, aggrecan is mainly found in the outer region of the developing wall [14].

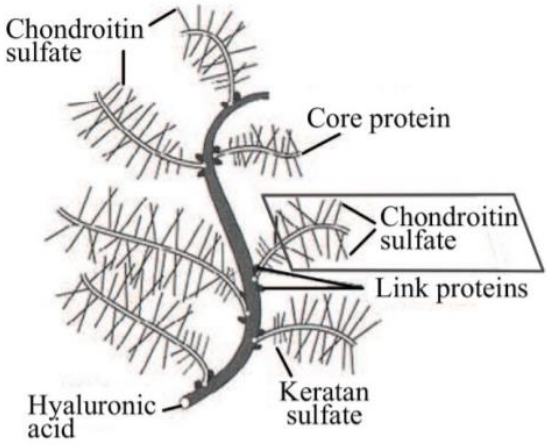

Figure 6 – Sketch depicting the structure of a large proteoglycan aggregate consisting of keratan sulfate and chondroitin sulfate attached to the core protein, for example, aggrecan or versican, that are attached to hyaluronan molecule via linking proteins [15] *(2012)*

1.3. Healthy aortic wall

The aorta, the main artery of the human circulatory system, carries oxygenated blood from the heart to the periphery of the human body. The aorta is spanned by a unidirectional blood flow ejected by the left ventricle (LV); flow direction is maintained constant by the aortic valve, which opens and closes allowing blood flow from the LV to the ascending aorta ad avoiding the blood backflow inside the heart.

The aorta can be divided into different parts, including the aortic root, ascending aorta, aortic arch and descending aorta. The aortic root is directly connected to the left ventricle of the heart, and it comprises of the aortic valve, interleaflet triangles, sinuses of Valsalva and sino-tubular junction [16], as illustrated in Figure 7.

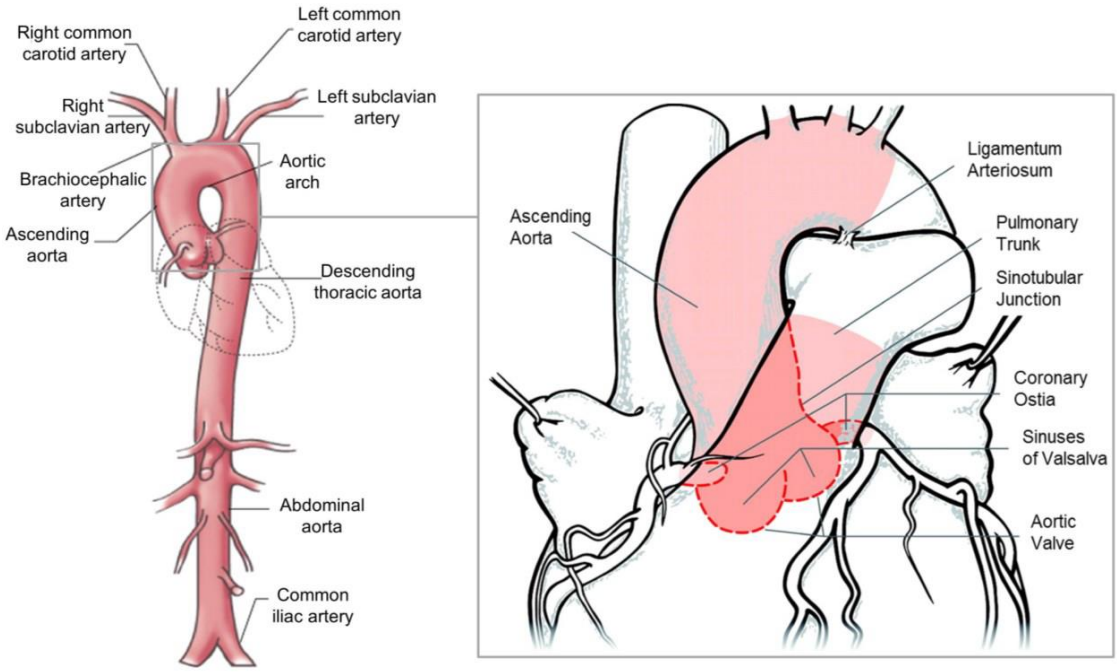

Figure 7 – The structure of the human aorta (modified from Tadros et al. 2009 [17]*)*

The sinuses (right, left and non-coronary) are aortic root bulges connected to the three aortic valve leaflets and the sino-tubular junction. The aortic valve leaflets separate the LV volume to aortic volume and with their motion, allow the blood to flow from the LV to the aorta, during systole and prevent the backflow of blood into the LV during diastole when the pressure inside aorta becomes higher than the intra-ventricular pressure.

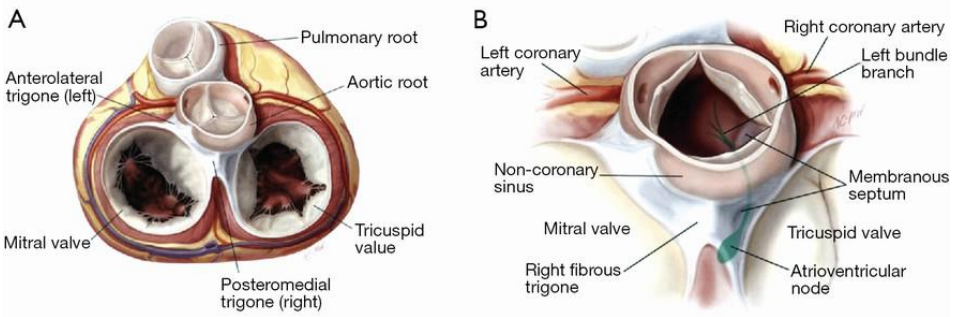

Figure 8 – (A, B) Anatomical connections of the aortic root and the pulmonary, mitral and tricuspid valves. [From Carpentier et al.*, 2010* [18] *].*

Microscopic examination has revealed that arterial tissue is heterogeneous and consists of three main layers: intima (the innermost layer), media and adventitia (the outermost layer), as illustrated in Figure 10. The mechanical properties of arterial walls are strongly influenced by the concentration and structural arrangement of constituents such as collagen and elastin, the hydrated matrix of proteoglycans, and the topographical site and respective function in the organism:

- The ***tunica intima*** is the innermost layer of the artery. It consists of a single layer of endothelial cells and a portion of connective tissue. In general, the endothelial cells tend to be elongated in the direction of the blood flow. It acts as a semipermeable membrane, through which nutrients and chemical signals can reach the cells in the vessel wall from the bloodstream. The intima has also a key role in regulating the active response of the vessel: as a membrane, it is the conduit through which pressure regulating agents reach the media. Additionally, it is known that the intima produces NO (nitric oxide), which relaxes smooth muscle cells in the media and thus helps control the vascular tone. Despite its great functional importance, due to its small thickness (~80 nm) in young arteries, the intima is usually neglected when considering the different layer contributions to the global mechanical resistance of the vessel wall. The mechanical contribution of the intima may become significant for aged arteries (arteriosclerosis) (the intima becomes thicker and stiffer); see, for example, Schulze-Bauer et al. (2001) [19]. In addition, it is important to note that pathological changes of the intimal components (atherosclerosis) are associated with significant alterations in the mechanical properties of arterial walls, differing significantly from those of healthy arteries.
- The ***tunica media*** is the middle layer of the artery and consists of a complex three-dimensional network of smooth muscle cells, elastin and collagen fibrils. It is

responsible for aortic behaviour. The media is separated from the intima and adventitia by the so-called internal elastic lamina and external elastic lamina (absent in cerebral blood vessels), respectively. In muscular arteries, these laminae appear as prominent structures, whereas in elastic arteries they are hardly distinguishable from the regular elastic laminae. The close interconnection between the elastic and collagen fibrils, elastic laminae, and smooth muscle cells together constitute a continuous fibrous helix. The helix has a small pitch so that the smooth muscle cells in the media are almost circumferentially oriented. This structured arrangement gives the media high strength, resilience and the ability to resist loads in both the longitudinal and circumferential directions. From the mechanical perspective, the media is the most significant layer in a young healthy artery. Due to the high content of smooth muscle cells, it is the media that is believed to be mainly responsible for the viscoelastic behaviour of an arterial segment.

- The ***adventitia*** is the outermost layer of the artery. It consists of a dense network of type I collagen fibres with scattered fibroblasts, elastin and nerves. The adventitia is surrounded continuously by loose connective tissue. The fibres of the adventitia confirming the hypothesis that the adventitia serves as a protective sheath, preventing rupture of the vessel due to an acute increase in pressure. The wavy collagen fibrils are arranged in helical structures and serve to reinforce the wall. They contribute significantly to the stability and strength of the arterial wall. The adventitia is much less stiff in the load-free configuration and at low pressures than the media. However, at higher levels of pressure, the collagen fibres reach their straightened lengths and the adventitia changes to a stiff 'jacket-like' tube which prevents the artery from overstretching and rupture.

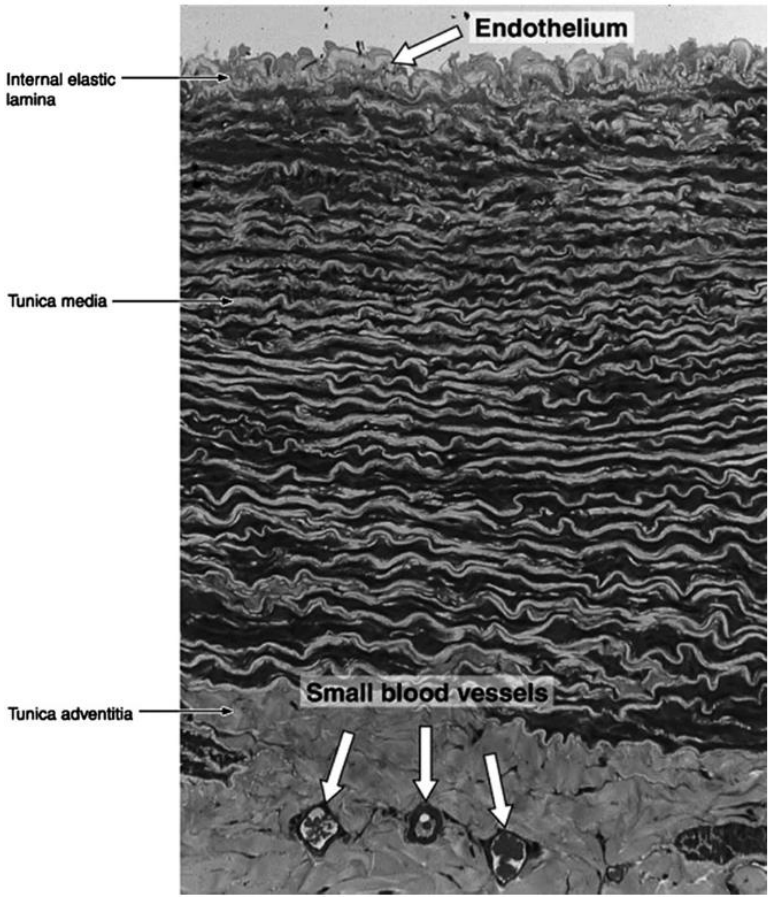

Figure 9 – Transverse section of the wall of a large elastic artery demonstrating the well-developed tunica media containing elastic lamellae.

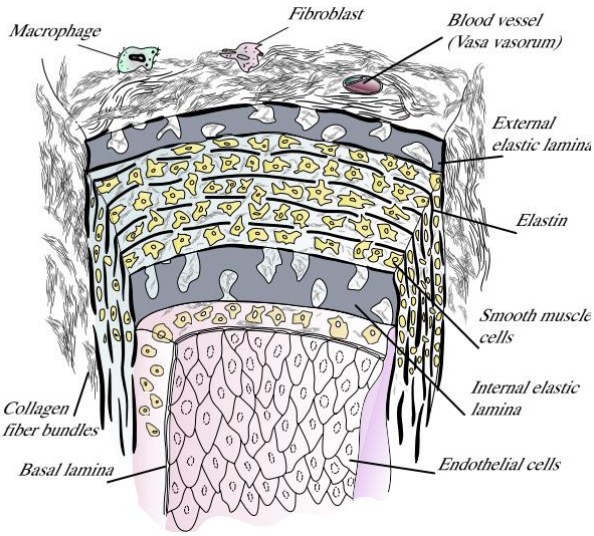

Figure 10 – Schematic representation of an elastic artery. Adapted from Rhodin [20].

1.4. Aortic Aneurysm

The average normal aortic diameter lies between 20 and 25 mm [21] but can reach up to 35 mm and still considered normal [22]. Typically, an ascending aorta diameter equal to or greater than 40 mm indicates dilatation, while a diameter equal to or exceeding 1.5 times the normal expected diameter is considered an aneurysm [10-11].

According to the morphology, aneurysms can be either saccular or fusiform, the latter being more common in the aorta. They can also be classified according to the aortic segment involvement as thoracic, thoracic- abdominal or abdominal (Figure 11).

A thoracic aortic aneurysm is asymptomatic in the vast majority of patients, usually being diagnosed via an imaging study carried out for another purpose (echocardiogram (ECHO) or CT scan). In the few patients who do have premonitory symptoms, these usually take the form of chest pain; if no other causes for chest pain are found, the pain can fairly be presumed to originate from the thoracic aneurysm. Ascending thoracic aortic aneurysms are perceived as a 'silent killer' with 95% of the incidents not diagnosed until complications such as dissection or rupture occur [24]. ATAAs are particularly lethal with an estimated mortality rate as high as 62% in patients with ATAAs larger the 6 cm [25].

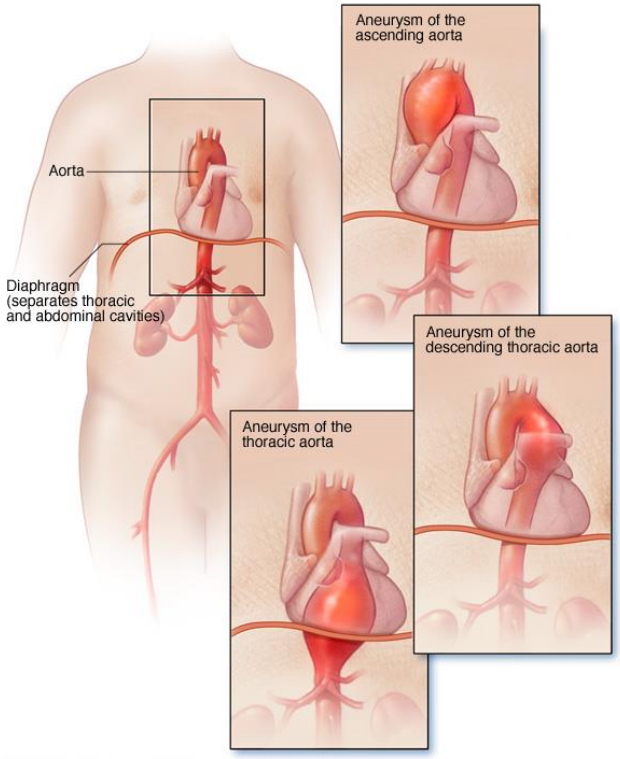

Figure 11 – Representation of various type of aortic aneurysm. Illustration adapted from https://www.mayoclinic.org

Aortic aneurysm occurs when the arterial wall loses its structural integrity due to medial degeneration and gives way to the distending forces of the pulsatile intraluminal pressure (as in Marfan syndrome) or excessive stress (hypertension). The formation of aortic aneurysm is associated with the local production of enzymes and matrix metalloproteinases (MMPs), which are capable of degrading the extracellular matrix of the aortic wall, including elastic fibres and interstitial collagens. This results in medial degeneration, characterised by elastic fibre loss from the medial layer, loss of vascular smooth muscle cells and proteoglycans deposition.

ATAAs are associated with several predisposing factors, such as the presence of a congenital defect like the bicuspid aortic valve (BAV), or the presence of connective tissue disorder such as Marfan or Ehlers syndrome.

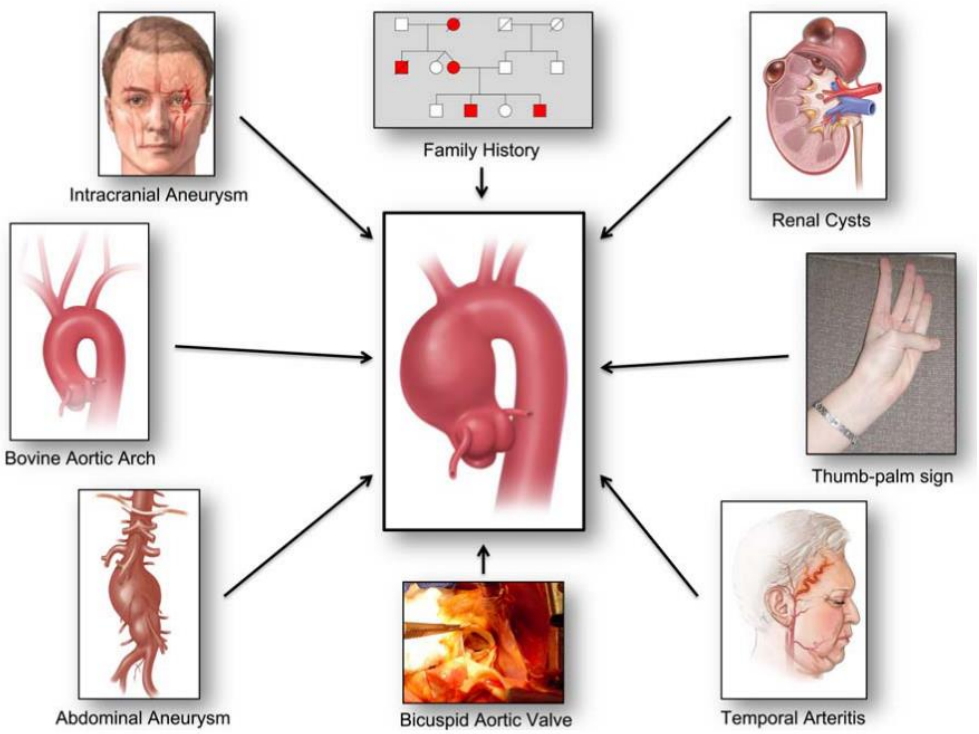

Figure 12 – Paradigm of "Guilt by Association" for the detection of silent thoracic aortic aneurysms

The choice of the best treatment for ATAA is an ongoing debate since the physician has to deal with the risk of leaving the aneurysm untreated and the risk connected to treat the aneurysms surgically. Elective surgical procedures are often contraindicated due to high risk connected to surgery and patients' general condition; adversely, if left untreated, ATAAs may suddenly rupture or dissect leading to a mortality rate as high as 96%. Understanding when these complications may happen is the most critical part of the clinical decision process about elective surgical repair. Currently, the gold standard to evaluate the timing of operation for patients with ATAA is based on the maximum aortic diameter criterion suggested by Coady at al.[26]. This criterion prescribes that if AoAs diameter is above 6 centimetres, for both ATAA and AAA, an elective surgical procedure should be operated. The clinical decision is also supported by the evaluation of aneurysm growth rate; it has been reported an average

aneurysm growth of 0.1cm/year for TAAs, with an average of 0.19 cm/year for descending thoracic aortic aneurysms and 0.07 cm/year for ATAAs [23].

Despite diameter criterion is widely used in clinical practice worldwide, aneurysm rupture with a diameter value below 6 centimetres is not infrequent. Moreover, following the European guidelines, ATAA associated with BAV should be replaced at 5.0 cm if ATAA growth more than 0.2 cm/year or in presence of risk factor like hypertension [23]. Della Corte et al. [27] proposed a classification scheme of the dilated aorta in which the aortas were divided on the base of their dilatation pattern (i.e. non-dilated, ascending phenotype and root phenotype). Another classification proposed by Schaefer et al. [28] classify the aorta in three groups (i.e. Type N, Type A and Type E) according to the commonly observed shapes of aortic dilatations.

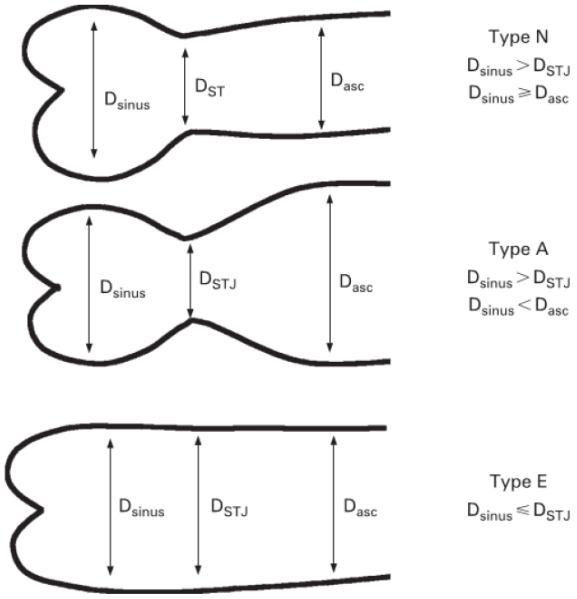

Figure 13 – Aortic shapes. Schematic of three aortic shapes that are all-inclusive. D_{sinus}, diameter at the sinus of Valsalva; DSTJ, diameter at the sino-tubular junction; D_{asc}, diameter in the mid ascending aorta. Schaeffer et al 2014 [28]

Several attempts have been made to establish if the mechanism based on ATAA is genetic or hemodynamic in origin (Figure 14). The genetics theory supports the idea that ATAA is a

direct consequence of aortic wall weakness and that this weakness is due to abnormal regulatory pathways of extracellular matrix degeneration within the aortic media. This idea is supported by the observation that BAV and TAV had histological and molecular differences. On the other hand, the hemodynamic theory is based on the idea that abnormal flows inside the aorta, like those introduced by BAV, may impose high loads on the aortic wall that promote the aneurysm generation and growth. This theory is supported by the observation that different phenotype of BAV leads to different aortic dimension. However, it is possible to speculate that both hemodynamic and genetic may be responsible for aneurysm growth.

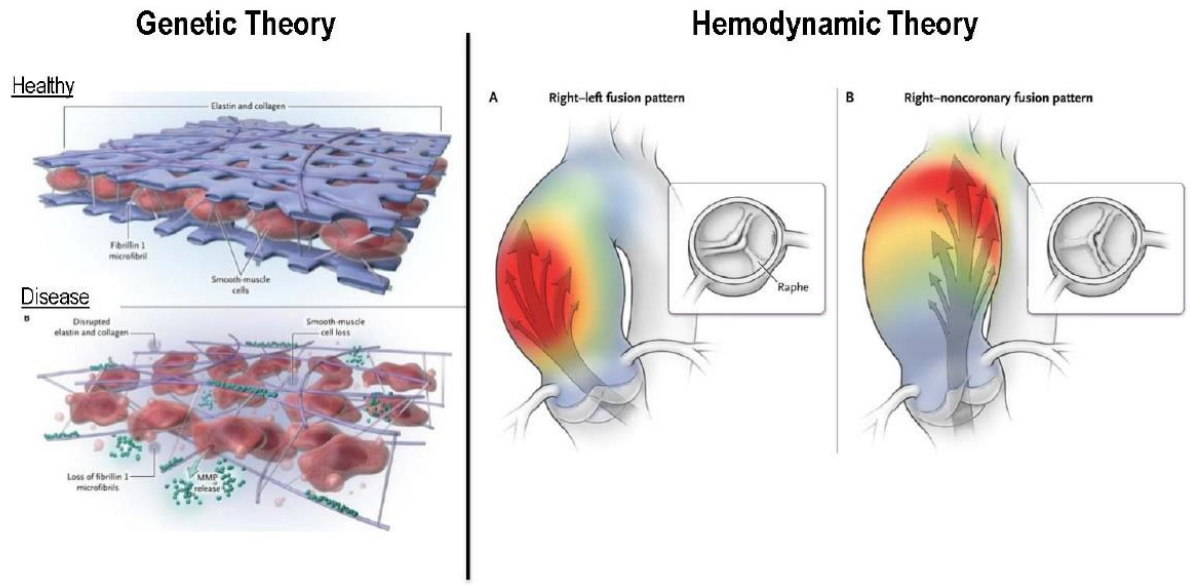

Figure 14 – Representation of the genetic and hemodynamic theory based on ascending thoracic aortic aneurysms (figure of Verma et al 2014 [29]*)*

1.5. Arterial Mechanics

The mechanical behaviour of blood vessels has been a subject of research for over 100 years, with the first report of Roy [30] dating back to the late 19th century.

1.5.1. Residual Stresses

A salient characteristic of the vascular mechanical behaviour is the existence of residual stresses in an otherwise unloaded vessel. If an arterial ring is cut radially it springs open and an axial strip excised from the artery bends away from its vessel axis. These observations expose the existence of residual stresses in the wall, both in the axial and circumferential direction. It was Bergel in 1960 [31], who first reported about residual stresses in arteries. The fact that the vascular ring opens when cut radially implies that the luminal part is under compression, while the external part is under tension. In vivo, however, the internal pressure equilibrates these stresses, and the whole wall supports a more uniform level of stress throughout the radius [23-24]. It has been demonstrated that elastin is largely responsible for the residual stress [34]. These effects are manifested externally, in that the internal elastic lamina is wavier in histological samples of the load-free state than those of the stress-free configuration or under in vivo conditions [35]. The existence of residual stresses immediately suggests the question about a stress-free configuration and its measure. Chuong and Fung [33] suggest the opening angle of the vascular sample as the only measure to quantify the residual circumferential deformation of the vessel. This is a popular measure due to its simplicity and is routinely found in the literature. Besides, it has been shown that a single cut releases most of the residual stresses, and that the opening angle is relatively insensitive to the exact location [25-27]. Contrasting these findings, it has been shown that the opening angle is different for each layer [26-27]. Matsumoto et al. [39] have found that even in this macroscopic stress-free configuration, the lamellar unit in the aorta is subject to residual stresses at the microscopic level. All these results are mutually compatible if the stress-free configuration is considered as a boundary value problem: if the boundary conditions change

(for example, the vessel layers are separated), the equilibrium configuration will change accordingly.

1.5.2. Anisotropy

One fundamental characteristic of the soft tissue is its marked anisotropy, indicated by different behaviour in the circumferential and axial directions. Most researches agree that the mechanical response of arterial tissue is anisotropic with respect to the load-free configuration, based on the comparison of the material parameters associated with circumferential and axial directions [29 – 32].

1.5.3. Incompressibility, Viscoelasticity and Pseudo elasticity

Most biological soft tissues have a water content of more than (70 - 80) % justifying the usual assumption that it is incompressible. Therefore, they hardly change their volume (isovolumic) even if the load is applied, and they are almost incompressible. The incompressibility assumption is applied to most biological soft tissues (Carew et al. (1968) [44] and Chuong and Fung (1984) [33]). The incompressibility assumption is very important in the formulation of constitutive laws for soft tissues because the sum of all principal (logarithmic) strains is always zero.

1.5.4. Mechanical Behaviour

The tensile response of soft tissue is nonlinear stiffening and tensile strength depends on the strain rate. In contrast to hard tissues, soft tissues may undergo large deformations. Some soft tissues show viscoelastic behaviour (relaxation and/or creep), which has been associated with the shear interaction of collagen with the matrix of proteoglycans [45] (the matrix provides viscous lubrication between collagen fibrils). Figure 15 shows a schematic diagram

of a typical J-shaped stress-strain (traction) curve for soft tissue. In detail, the curve describes the stress-strain behaviour for the skin which is representative of the mechanical behaviour of many soft connective tissues (collagenosis).

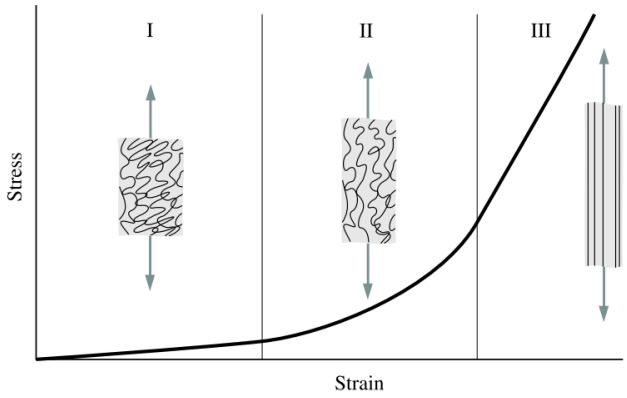

Figure 15 – Schematic diagram of a typical stress-strain curve for skin showing the associated collagen fibre morphology.

This form, representative for many soft tissues, differs significantly from stress-strain curves of hard tissues or other types of (engineering) materials. Also, Figure 15 shows how the collagen fibres straighten with increasing stress. The deformation behaviour for skin may be studied in three phases I, II and III:

Phase I. In the absence of loading the collagen fibres, which are woven into the rhombic-shaped pattern, are in relaxed conditions and appear wavy and crimped. Unstretched tissue behaves approximately isotropically. Initially, low stress is required to achieve large deformations of the individual collagen fibres without requiring a stretch of the fibres. In phase I the tissue behaves like a very soft (isotropic) rubber sheet, and the elastin fibres are mainly responsible for the stretching mechanism. The stress-strain relation is approximately linear, the elastic modulus of tissue in phase I is low (0.1-2 MPa).

Phase II. In phase II, as the load is increased, the collagen fibres tend to line up with the load direction and bear loads. The crimped collagen fibres gradually elongate and they

interact with the hydrated matrix. With deformation, the crimp angle in collagen fibrils leads to a sequential uncrimping of fibrils.

Phase III. In phase III, at high tensile stresses, the crimp patterns disappear and the collagen fibres become straighter. They are primarily aligned with one another in the direction in which the load is applied. The straightened collagen fibres resist the load strongly and the tissue becomes stiff at higher stresses. The stress-strain relation becomes linear again. Beyond the third phase, the ultimate tensile strength is reached and fibres begin to break.

The mechanical properties of soft tissues depend strongly on the topography, risk factors, age, species, physical and chemical environmental factors such as temperature, osmotic pressure, pH, and on the strain rate. The material properties are strongly related to the quality and completeness of experimental data, which come from in vivo or in vitro tests having the aim of mimicking real loading conditions. Therefore, to present specific values for the ultimate tensile strength and strain of a specific tissue is a difficult task.

Table 1 attempts to present ranges of values of mechanical properties and collagen/elastin contents (% dry weight) in some representative organs mainly consisting of soft connective tissues.

Material	Ultimate tensile strength [Mpa]	Ultimate tensile strain [%]	Collagen (% dry weight)	Elastin (% dry weight)
Tendon	\	10-15	75 - 85	< 3
Ligament	50-100	10-15	70-80	ott-15
Aorta	0.3 – 0.8	50-100	25-35	40-50
Skin	1-20	30-70	60-80	05-10
Articular Cartilage	9 – 40	60 -120	40-70	-

Table 1 – Mechanical properties [7] *and associated biochemical data of some representative organs mainly consisting of soft connective tissues.*

2. Project aims

The structure of the present thesis consists of n.4 chapters: 1) Introduction and Motivation 2) Background Knowledge 3) On the role of material properties in ascending thoracic aortic aneurysms, 4) Multiscale Biomechanical investigation of ATAA

Chapter 1 gives the motivation and objectives of this thesis and the contributions to science and technology; Chapter 2 provides the background knowledge on which this thesis is based. Chapter 3-4 deal with the determination of the mechanical behaviour and the constitutive modelling of human arteries disease by means experimental and computational model.

1. "*On the role of material properties in ascending thoracic aortic aneurysms*" aimed to evaluate differences in ATAA-related stress predictions resulting from the elastostatic analysis based on the optimization of arbitrary material properties versus the application of patient-specific material properties determined from ex-vivo biaxial testing.

   Cosentino, F. et al. (2019). *On the role of material properties in ascending thoracic aortic aneurysms*. Computers in Biology and Medicine, 109, 70-78.

2. "*Multiscale Biomechanical investigation of ATAA*" studies the macro-and microscopic mechanical tensile behaviours of human aortas using a biaxial tensile testing device and second harmonic generation. The results showed a relation between the orientation of the collagen fibres on the macroscopic stress and strain. This may be attributed first to a straightening, second to a reorientation of the collagen fibres.

These chapters, taken collectively, provide a versatile foundation for further work in the space of cardiovascular tissue failure.

3. Background Knowledge

3.1. Remarks on Continuum Mechanics

Continuum mechanics is the branch of mechanics dealing with the analysis of the kinematics and the mechanical behaviours of materials in terms of strain and stress. A fundamental assumption is the "*continuous medium hypothesis*": namely, that the real space occupied by a fluid or a solid can be approximately regarded as continuous without voids between the particles of matter. In the following section, a short introduction into continuum mechanics is given based on the work of Holzapfel et al.[9], which does help in explaining the theories in a clear and intelligible way. For further information and reading material concerning the topics covered, the works from Cowin and Doty [46], Ogden [47] and Ogden and Fu [48] they are warmly suggested.

Macroscopic systems often can be described successfully with a continuum approach. The fundamental assumption therein states that a body, denoted by $\mathcal{B}$, may be viewed as having a continuous (or a piecewise continuous) distribution of matter in time and space. The body is imagined as being a composition of a (continuous) set of particles (or continuum particles or material points), represented by $P \in \mathcal{B}$ as shown in Figure 16.

To characterize this body, it is defined a rectangular coordinate system with origin 0. While the continuum body $\mathcal{B}$ moves in space from one instant of time to another, it occupies a continuous sequence of geometrical regions denoted by $\Omega_0, \ldots, \Omega$. As a result, every particle $P \in \mathcal{B}$ corresponds to a so-called geometrical point owning a position in regions $\Omega_0, \ldots, \Omega$. Region Ω_0 corresponds at the undeformed configuration of the body $\mathcal{B}$ and at initial time $t=0$ is referred to as the *initial configuration*. Assuming that the region Ω_0 of space moves to a

new region Ω which is occupied by the continuum body $\mathcal{B}$ at a subsequent time $t>0$. The configuration of $\mathcal{B}$ at t is the so-called *deformed configuration*.

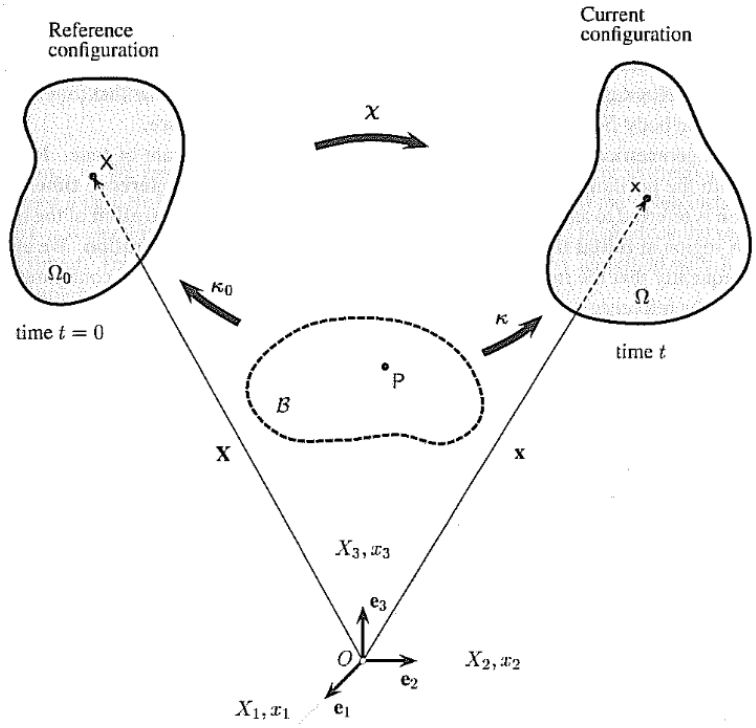

Figure 16 – Configuration and motion of a continuum body, adapted from Nonlinear Solid Mechanics [9]

Assuming that the map $\chi = \kappa_0(P, t)$ is a one-to-one correspondence between a particle $P \in \mathcal{B}$ and the point $X \in \Omega_0$ that $\mathcal{B}$ occupies at the given instant of time $t=0$. Moreover, let the map κ act on $\mathcal{B}$ to produce the region Ω at time t. The place $x = \kappa(P, t)$ that the particle P (evidently identified with X and t) occupies at t is described by (in symbolic and index notation):

$$x = \kappa[\kappa_0^{-1}(X, t)] = \chi(X, t) \qquad \textit{Equation 1}$$

The motion χ is assumed to be uniquely invertible. Consider $(x,\ t)$, the position of point X, which is associated with the place x at time t, is specified uniquely be Equation 1 as:

$$X = \chi^{-1}(x, t) \qquad \textit{Equation 2}$$

with the inverse motion denoted by χ^{-1}. For a given time $\mathbf{t}$, the inverse motion Equation 2 carries points located at Ω to points in the reference configuration Ω_0. In Equation 1 Equation 2 respectively the pairs $(\mathbf{X}, \mathbf{t})$ and $(\mathbf{x}, \mathbf{t})$ denoted independent variables.

3.1.1. Deformation Gradient and Strain Tensors

In continuum mechanics, the matter is assumed to be continuously distributed. Therefore, multiple phases can have coinciding positions. To describe the deformation of an arbitrary body with volume Ω and surface $\partial\Omega$ a tensor called deformation gradient $\mathbf{F}$ is introduced. Thus, we distinguish between the referential (undeformed) Ω_0 and current configuration (deformed) Ω with coordinates $\mathrm{X}(t)$ and $\mathrm{x}(\mathrm{X};t)$, respectively. The deformation gradient is given by:

$$\mathbf{F} = \frac{\partial \chi(\mathbf{X}, t)}{\partial \boldsymbol{X}} = Grad(\mathbf{x}(\mathbf{X}, t)) \qquad \textit{Equation 3}$$

where $Grad\,\mathbf{x}(\mathbf{X};\ t)$ represents the gradient operator applied to the map $\chi(\mathbf{X};\ t)$. The quantity F is crucial in nonlinear continuum mechanics and is a primary measure of deformation, called the deformation gradient. In general, F has nine components for all t, and it characterizes the behaviour of motion in the neighbourhood of a point. It is well known that the determinant of F, commonly noted J, represents the volume change between the reference and the current configurations:

$$\mathrm{J} = det(\mathbf{F}) = \frac{d\mathrm{V}}{\partial V_0} > 0 \qquad \textit{Equation 4}$$

In Equation 4, dV and dV_0 denote infinitesimal volume elements defined in the reference and current configurations called material (or undeformed) and spatial (or deformed) volume elements, respectively. Further, it can be assumed that the volume is a continuous (or at least a piecewise continuous) function of continuum particles so that $dV = dX_1 dX_2 dX_3$ and $dv =$

$dx_1 dx_2 dx_3$ (continuum idealization). The deformation gradient can be further decomposed into two tensors, one related to pure rotation and another to pure deformation. This decomposition, defined as polar decomposition, can be written as:

$$\mathbf{F} = \mathbf{RU} = \mathbf{VR} \qquad \textit{Equation 5}$$

Here, $\boldsymbol{R} \epsilon Orth^{+}$ is a unique rotation tensor (with the property that $\boldsymbol{R^T R} = \boldsymbol{R R^T} = \boldsymbol{I}$), while $\boldsymbol{U}$ is the right stretch tensor and $\boldsymbol{V}$ is the left stretch tensor. The two stretch tensors, both positive definite and symmetric (i.e. $\boldsymbol{U} = \boldsymbol{U^T}$ and $\boldsymbol{V} = \boldsymbol{V^T}$) and represent a pure deformation. Moreover, they can be diagonalized, and their spectral decomposition is given by:

$$\boldsymbol{U} = \lambda_1 \boldsymbol{N_1} \otimes \boldsymbol{N_1} + \lambda_2 \boldsymbol{N_2} \otimes \boldsymbol{N_2} + \lambda_3 \boldsymbol{N_3} \otimes \boldsymbol{N_3} \qquad \textit{Equation 6}$$

$$\boldsymbol{V} = \lambda_1 \boldsymbol{n_1} \otimes \boldsymbol{n_1} + \lambda_2 \boldsymbol{n_2} \otimes \boldsymbol{n_2} + \lambda_3 \boldsymbol{n_3} \otimes \boldsymbol{n_3} \qquad \textit{Equation 7}$$

They measure local stretching or contraction alone their mutually orthogonal eigenvectors, which is a change of local shape. The right stretch tensor $\mathbf{U}$ is defined with respect to the reference configuration while the left stretch tensor $\mathbf{V}$ acts on the current configuration.

As seen also through the polar decomposition of $\mathbf{F}$, the deformation gradient tensor, although containing all the useful information needed to describe the deformation behaviour of a body, is not a suitable deformation measure due to the presence of rotation. For this reason, it is necessary to define other measures, based only on its pure deformation part, as the *left* and *right Cauchy-Green tensors*, respectively $\mathbf{C}$ and $\boldsymbol{b}$. These two tensors are defined as

$$\mathbf{C} = \mathbf{F}^{\mathbf{T}}\mathbf{F} = \mathbf{U}^{\mathbf{T}}\mathbf{R}^{\mathbf{T}}\mathbf{R}\mathbf{U} = \mathbf{U}^{\mathbf{2}} \qquad \textit{Equation 8}$$

$$\mathbf{b} = \mathbf{F}\mathbf{F}^{\mathrm{T}} = \mathbf{V}\mathbf{R}\mathbf{R}^{\mathbf{T}}\mathbf{V}^{\mathbf{T}} = \mathbf{V}^{\mathbf{2}}$$ *Equation 9*

$\mathbf{C}$ and $\mathbf{b}$ are respectively a Lagrangian and an Eulerian strain tensor. It is possible to introduce the mutually orthogonal and normalized set of eigenvectors $\boldsymbol{N_a}$ and their corresponding eigenvalues λ_{a}, $\mathrm{a} = 1, 2, 3$, of the material tensor $\mathbf{U}$ as:

$$\boldsymbol{U}\boldsymbol{N_a} = \lambda_a \boldsymbol{N_a}\,, |\boldsymbol{N_a}| = \mathbf{1}$$ *Equation 10*

Furthermore, by means of the combination of Equation 8 Equation 9 and Equation 10, it is possible to obtain the eigenvalue problem for right Cauchy-Green tensor $\mathbf{C}$ as:

$$\mathbf{C}\mathbf{N}_{\mathbf{a}} = \mathbf{U}^{\mathbf{2}}\mathbf{N}_{\mathbf{a}} = \lambda_{\mathrm{a}}^{2}\mathbf{N}_{\mathbf{a}}$$ *Equation 11*

It is necessary to solve homogeneous algebraic equations for the unknown eigenvalues λ_a, $\mathrm{a} = 1, 2, 3$ and unknown eigenvectors $\mathbf{N}_{\mathbf{a}}$, $\mathrm{a} = 1, 2, 3$, in the form:

$$(\mathbf{C} - \lambda_{\mathrm{a}}^{2}\mathbf{I})\mathbf{N}_{\mathbf{a}} = \mathbf{0}$$ *Equation 12*

To obtain the eigenvalues, the characteristic polynomial of $\mathbf{C}$ must be solved:

$$\lambda_a^3 - I_1\lambda_a^2 + I_2\lambda_a - I_3\,,\ \mathrm{a}=1,2,3$$ *Equation 13*

with the three principal invariants I_a of the right Cauchy-Green deformation tensor $\mathbf{C}$:

$$I_1(\boldsymbol{C}) = tr(\boldsymbol{C})$$ *Equation 14*

$$I_2(\boldsymbol{C}) = \frac{1}{2}(tr(\boldsymbol{C})^2 + tr(\boldsymbol{C}^2)$$ *Equation 15*

$$I_3(\boldsymbol{C}) = \det(\boldsymbol{C})$$ *Equation 16*

In these equations, the right Cauchy-Green deformation tensor $\mathbf{C}$ can be replaced by the left Cauchy-Green deformation tensor $\mathbf{b}$. The eigenvalues of the symmetric tensor $\mathbf{U}$ are λ_a, called the principal stretches, while for the symmetric tensor $\mathbf{C}$, which is found to be the squares of the principal stretches denoted by λ_a. Stretch ratios are defined as the square root of the eigenvalues of $\mathbf{C}$ (equal to those of $\mathbf{b}$) and are classically denoted as λ_a, a = 1, 2, 3. Using this ratio, principal invariants can be expressed as:

$$I_1(\boldsymbol{C}) = tr(\boldsymbol{C}) = \lambda_1^2 + \lambda_2^2 + \lambda_3^2 \qquad \textit{Equation 17}$$

$$I_2(\boldsymbol{C}) = \frac{1}{2}(tr(\boldsymbol{C})^2 + tr(\boldsymbol{C}^2) = \lambda_1^2\lambda_2^2 + \lambda_1^2\lambda_3^2 + \lambda_2^2\lambda_3^2 \qquad \textit{Equation 18}$$

$$I_3(\boldsymbol{C}) = \det(\boldsymbol{C}) = \lambda_1^2\lambda_2^2\lambda_3^2 \qquad \textit{Equation 19}$$

The invariant I_1, I_2 and I_3 are used as quantities for isotropic deformation. The invariant I_1 represents a line change measure, I_2 an area change measure, whereas I_3 is used for volumetric change descriptions. There are other adoptable deformation measures, such as the Green-Lagrange strain tensor or the Euler-Almansi strain tensor, respectively defined as:

$$\mathbf{E} = \frac{\mathbf{1}}{\mathbf{2}}(\mathbf{C} - \mathbf{I}) \qquad \textit{Equation 20}$$

$$\boldsymbol{e} = \frac{\mathbf{1}}{\mathbf{2}}(\mathbf{I} - \mathbf{b^{-1}}) \qquad \textit{Equation 21}$$

One of the major advantages arising from the use of the Green-Lagrange strain measure derives directly from the logarithm properties and is based on the additive decomposition of the applied deformation history. In fact, by considering a deformation of a fibre, say λ, as the result of the combination of two stretches (in this case $\lambda_1 = \frac{l}{l_1}$ and $\lambda_0 = \frac{l}{l_0}$, where l_1 can be

considered as an intermediate length of the fibre in its change of length from l_0 to l), it is possible to write the correspondent Hencky (true strain) is defined as:

$$\epsilon = \ln\frac{l}{l_0} = \ln\frac{l}{l_0}\frac{l_1}{l_0} = \ln\lambda_1 + \ln\lambda_0 \qquad \textit{Equation 22}$$

3.1.2. Stress Measures

Motion and deformation give rise to interactions between the material and neighbouring material in the interior part of the body. One of the consequences of these interactions is stress, which has a physical dimension force per unit of area.

By focusing the attention on a deformable body $\mathcal{B}$ which occupies an arbitrary region Ω with a boundary $\partial\Omega$ at a time t, it is at first necessary to define *external forces* as forces acting on parts of the boundary, and as *internal forces* the ones within the interior part of the domain. Now, let the body be cut by a plane passing through a given point $x \in \Omega$; this plane, which can be indicated as π, cuts the body in two parts. By considering the interaction of the two portions, it is possible to realize that forces are transmitted across the plane surface.

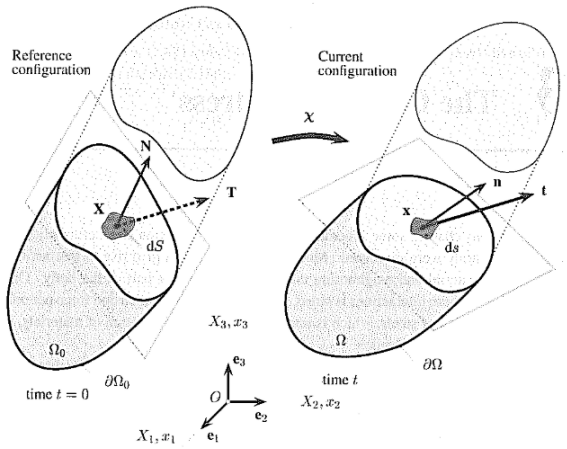

Figure 17 – Traction vectors acting on infinitesimal surface elements with outward unit normal, adapted from Nonlinear Solid Mechanics.

The infinitesimal resultant force acting on a surface element of the area dS is df. In this way, it is possible defined Cauchy surface traction as:

$$\boldsymbol{t}(\boldsymbol{x},t)=\frac{df}{dS} \qquad \textit{Equation 23}$$

The traction vector in Equation 23 persists on all surfaces passing through the point P that have the same normal vector $\boldsymbol{n}$. It is possible at this point to recall the Cauchy stress theorem, which asserts that there exists a second-order tensor $\sigma(\boldsymbol{x},t)$ so that the traction vector $\boldsymbol{t}$ is a linear function of $\boldsymbol{n}$, so that:

$$\tau(\boldsymbol{x},t,\boldsymbol{n})=\sigma(\boldsymbol{x},t)\boldsymbol{n} \qquad \textit{Equation 24}$$

Through equilibrium of the angular momentum, it also is possible to show that the second-order tensor $\sigma(\boldsymbol{x},t)$, generally called *Cauchy stress tensor*, is symmetric. It is defined through the Eulerian description, and can be represented as:

$$\boldsymbol{\sigma}(\boldsymbol{x},t)=\sigma_{ij}\boldsymbol{n_i}\otimes\boldsymbol{n_j} \qquad \textit{Equation 25}$$

By multiplying the Cauchy stress tensor by the Jacobian J it is possible to obtain the *Kirchhoff stress tensor*, τ:

$$\boldsymbol{\tau}=J\boldsymbol{\sigma} \qquad \textit{Equation 26}$$

Instead, by following the same treatise as for the Cauchy stress tensor through an Eulerian description, it is possible to obtain the first Piola-Kirchhoff stress tensor by doing so through a Lagrangian description:

$$\mathbf{P}=\mathrm{P_{ij}}\mathbf{n_i}\otimes\mathbf{N_j} \qquad \textit{Equation 27}$$

It is important to notice also that the first Piola-Kirchhoff stress tensor is not symmetric. The second Piola-Kirchhoff stress tensor, instead, is symmetric and defined as:

$$\mathbf{S}=\mathbf{F}^{-1}\mathbf{P} \qquad \textit{Equation 28}$$

A fundamental relationship between the first Piola-Kirchhoff stress tensor $\mathbf{P}$ and the second Piola-Kirchhoff stress tensor $\mathbf{S}$ is found as follows:

$$\boldsymbol{P} = \boldsymbol{FS} \qquad \textit{Equation 29}$$

To obtain the stress tensors, we need a material law describing the relation of stress and strain.

3.2. Constitutive model for arteries

A constitutive model is a mathematical characterization of materials intrinsic relationship between force and deformation (or stress and strain), and along with appropriate governing equations, capable of describing the mechanical behaviour of the material under specific conditions. Appropriate constitutive relations are needed for computational modelling of stress-strain states in arteries.

A hyperelastic material behaviour law is a type of constitutive model for ideally elastic material for which the stress-strain relationship derives from a strain energy density function W [70]. *Hyperelasticity theory* states that for any solid there exists a strain energy function W which depends only on the deformation. So, hyperelastic constitutive relations represent a mathematical description of stress and strain components that are derived from strain energy density function W. At any referential position $\boldsymbol{X}$ of the tissue, we postulate the existence of a Helmholtz free-energy function Ψ. We assume the decoupled form

$$\Psi = \mathrm{U}(\mathbf{X};\ \mathrm{J}) + \bar{\psi}(\mathbf{X}, \bar{\mathbf{C}}, \boldsymbol{A}_1, \boldsymbol{A}_2) \qquad \textit{Equation 30}$$

where U is a purely volumetric (dilatational) contribution and $\bar{\psi}$ is a purely isochoric (volume-preserving) contribution to the free energy ψ. Here $\mathbf{C} = \mathbf{F}^{\mathrm{T}}\mathbf{F}$ denotes the modified right

Cauchy Green tensor, $\mathrm{J}>\det\mathrm{F}$ denoting the local volume ratio. In addition $\boldsymbol{A_1}, \boldsymbol{A_2}$ are a set of two (second-order) tensors which characterize the anisotropic properties of the tissue at any $\boldsymbol{X}$. The structure tensors $\boldsymbol{A_1}$ and $\boldsymbol{A_2}$ are defined as the tensor products $a_{0i} \otimes a_{0i}$, where $a_{0i}, i = 1,2$, are two unit vectors characterizing the orientations of the families of collagen fibers in the (undeformed) reference configuration of the tissue (see Figure 18)

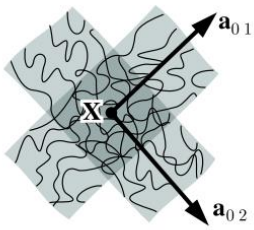

Figure 18 – Arrangement of collagen fibers in the reference configuration characterized by two directions [43]

Since arteries do not change their volume within the physiological range of deformation, we now focus attention on the description of their isochoric deformation behaviour characterized by the energy function $\overline{\Psi}$. We suggest the simple additive split:

$$\overline{\Psi} = \overline{\Psi}_{iso}(\mathbf{X}; I_1) + \overline{\Psi}_{aniso}(\mathbf{X}; I_4, I_6) \qquad \textit{Equation 31}$$

where $\overline{\Psi}_{iso}$ associated with isotropic deformations and apart $\overline{\Psi}_{aniso}$ associated with anisotropic deformations. To define the energy function $\overline{\Psi}$, we used the following invariant:

$$\begin{aligned} \mathrm{I}_1 &= \mathbf{C}\colon \mathrm{I} \\ \mathrm{I}_4(\mathbf{C}, a_{01}) &= \mathbf{C}\colon \mathrm{A}_1 \\ \mathrm{I}_6(\mathbf{C}, a_{02}) &= \mathbf{C}\colon \mathrm{A}_2 \end{aligned} \qquad \textit{Equation 32}$$

The invariant I_4 and I_6 re squares of the stretches in the directions of a_{01} and a_{02}, respectively. Isotropy is described through the invariant I_1 and anisotropy through I_4 and I_6. If we neglect the change of area for the body, we call this the nominal stress or first Piola-Kirchhoff stress tensor $\mathbf{P}$. The first Piola-Kirchhoff stress tensor is a quantity with its force

defined in the actual configuration and its area defined in the referential configuration $\boldsymbol{\Omega_0}$. Thus, the first Piola-Kirchhoff stress tensor is unsymmetrical and defined via:

$$\mathbf{P} = \frac{\partial \Psi}{\partial \boldsymbol{F}} = \sum_{\mathrm{i}} \frac{\partial \Psi}{\partial I_i} \frac{\partial I_i}{\partial \boldsymbol{F}} \qquad \textit{Equation 33}$$

Finally, the true stress tensor also called Cauchy stress tensor $\boldsymbol{\sigma}$ describes the actual stress referred to the actual surface. The Cauchy stress is obtained through:

$$\boldsymbol{\sigma} = J^{-1}\boldsymbol{P}\boldsymbol{F} \qquad \textit{Equation 34}$$

The strain-energy function Ψ can be composed of various energy functions as long as the laws of thermodynamics are fulfilled. The second law of thermodynamics states that energy can never be created and dissipation is either zero or positive. Neglecting thermal effects the internal dissipation is given by:

$$\mathrm{D_{int}} = \mathbf{P}\colon \dot{\mathbf{F}} - \dot{\psi} \geq 0 \qquad \textit{Equation 35}$$

If the internal dissipation is zero, the process is completely reversible without entropic effects. Hence, we find lossless Clausius-Planck equation:

$$\dot{\psi} = \mathbf{P}\colon \dot{\mathbf{F}} \qquad \textit{Equation 36}$$

Hyperelastic models can be classified into two types of formulation, depending on the approach to develop the strain energy function. The first kind of models are from the mathematical developments of W.

They are classically referred to as phenomenological models. Material parameters a generally difficult to determine and such models can lead to an error when they are used out of the deformation range in which their parameters were identified.

These include:

1. The Mooney Rivlin Model

$$W = C_1(I_1 - 3) + C_2(I_2 - 3) \quad \textit{Equation 37}$$

2. The Yeoh Model

$$W = C_1(I_1 - 3) + C_2(I_1 - 3)^2 + C_3(I_1 - 3)^2 \quad \textit{Equation 38}$$

3. The Biderman Model

$$W = C_{10}(I_1 - 3) + C_{01}(I_1 - 3) + C_{01}(I_1 - 3)^2 + C_{30}(I_1 - 3)^2 \quad \textit{Equation 39}$$

4. The Ogden Model

$$W = \sum_{n=1}^{N} \frac{\mu_n}{\alpha_n}(\lambda_1^{\alpha_n} + \lambda_2^{\alpha_n} + \lambda_3^{\alpha_n} - 3) \quad \textit{Equation 40}$$

The phenomenological based models are summarized in Table 2

Model	Year	Number of material parameters	Equation
Mooney Rivlin	1940	2	Equation 37
Odgen	1972	6	Equation 40
Biderman	1958	4	Equation 39
Yeoh	1990	3	Equation 38

Table 2 – List of the phenomenological-based models by the year of publication

The second kind of models are "*Physical models*". The main models being discussed in this section will be Neo-Hookean, Fung's and Holzapfel-Gasser-Ogden's strain energy models. The strain energy equations can be modified for 2-D as well as 3-D analysis. The following models will be presented in their 3-D form with the exception of the Fung model.

The Neo-Hookean model. The Neo-Hookean model is the simplest strain energy model; it describes the behaviour of rubber and takes a form that is closest to the typical stress-strain relationship seen in many metals. Assuming incompressibility:

$$W = c_1(tr\boldsymbol{C} - \mathbf{3}) \qquad \textit{Equation 41}$$

where

$$tr\boldsymbol{C} = 2(E_{11} + E_{22} + E_{33}) + 3 \qquad \textit{Equation 42}$$

and E_{11}, E_{22}, and E_{33} are the Green strains in the fibre and two cross-fibre directions. The Neo-Hookean model only has one material constant and displays a linear relationship between the Cauchy stress and right Cauchy-Green deformation, hence the name that is in reference to Hooke's Law. The Neo-Hookean has been shown to describe the isothermal behaviour of rubber for up to 30% deformation whereas Hooke's Law only applies for linear elastic behaviour of engineering metals, generally up to 0.2% strain. However, the Neo-Hookean model only describes the behaviour for isotropic materials, and therefore cannot be used to describe most soft tissue materials.

Fung Model. The Fung strain energy model was initially developed to describe the behaviour of skin tissue; however, it has also been determined that variations of this model can reliably describe other soft tissue behaviour such as heart valvular tissue [7]. The following is the generalized pseudo-elastic 2D Fung strain energy model. The strain energy function takes on an exponential form:

$$W = \frac{c_1}{2}[\exp(Q_F) - 1] \qquad \textit{Equation 43}$$

where Q_F is a quadratic function of the two principal strains of the material and shear strain.

$$Q_F = c_2E_{11}^2 + c_3E_{22}^2 + 2c_4E_{11}E_{22} + c_5E_{12}^2 + 2c_6E_{11}E_{12} + 2c_7E_{22}E_{12}$$ *Equation 44*

E_{11} is the Green strain along the fibre direction of the soft tissue while E_{22} is the Green strain in the cross-fibre direction. Shear strains E_{12} and E_{21} are equal because the Green strain tensor is symmetric by definition. The Fung model assumes soft tissue to be orthotropic and contains seven material constants; c_1 is a scaling factor usually in terms of membrane tension (N/m) or stress (N/m^2) while the other six constants are dimensionless. These parameters have no direct physical meaning.

The Holzapfel, Gasser, and Ogden model. The Holzapfel, Gasser, and Ogden (HGO) strain energy function was developed to model arterial behaviour [49]. While the Fung model is considered phenomenological, i.e. not derived directly from first principles and the material's microstructure, the HGO model was developed from theory regarding the mechanics of fibre-reinforced composites. The HGO strain energy function assumes the material to be orthotropic and was determined by modelling an artery as a thick-walled cylinder, with two families of collagen arranged in helices along its length [49]. The model is made from different layers with separated strain-energy functions [49]. Each layer is considered a composite with the collagen fibres acting as reinforcement. As each layer displays similar mechanical behaviour the same strain energy function was used but with different material constants [49]. The HGO model is split into two parts: the strain energy stored from isotropic deformations ψ_{iso} (the mechanical response from the non-collagenous matrix), and the strain energy from anisotropic deformations ψ_{aniso} from the collagen fibres [49]. The 3-D HGO strain energy equation for a layer of material is shown:

$$\psi(\boldsymbol{C}, \boldsymbol{A_1}, \boldsymbol{A_2}) = \psi_{iso}(I_1, I_2) + \psi_{aniso}(I_1, I_2 \ldots\ldots I_8)$$ *Equation 45*

where the families of collagenous fibers are characterized by the two (reference) direction vectors $a_{0,i}$, $i= 1,2$, with $|a_{0,i}|= 1$. Note that the invariants I_4 and I_6 are the squares of the stretches in the directions of a_{01} and a_{02}, respectively, so that they are stretch measures for the two families of (collagen) fibres and therefore have a clear physical interpretation. The anisotropy then arises only through the invariants I_4 and I_6, but this is sufficiently general to capture the typical features of arterial response. Finally, the two contributions ψ_{iso} and ψ_{aniso} to the function, ψ must be particularized to fit the material parameters to the experimentally observed response of the arterial layers. They used the (classical) neo-Hookean model to determine the isotropic response in each layer:

$$\psi_{iso}(I_1) = \frac{c}{2}(I_1 - 3) \qquad \textit{Equation 46}$$

where $c>0$ is a stress-like material parameter. The strong stiffening effect of each layer observed at high pressures motivates the use of an exponential function for the description of the strain energy stored in the collagen fibres, and for this, they proposed:

$$\psi_{aniso}(I_1, I_2) = \frac{k_1}{2k_2}\sum_{i=4,6}\{\exp[\,k_2(I_1 - 1)^2] - 1\} \qquad \textit{Equation 47}$$

where $k_1>0$ is a stress-like material parameter and $k_2>0$ is a dimensionless parameter.

3.3. Multiphoton Microscopy

The mechanical behaviour of the arterial wall is mainly governed by the organization and composition of the three major micro-structural components: collagen, elastin, smooth muscle cells. Research indicates that changes in the mechanical properties of healthy arterial walls play a role in arterial disease and degeneration (e.g., increased stiffening of vessel walls with age, atherosclerosis, etc.). Meaningful quantifications of these components in human arteries, therefore, are fundamental for a better understanding of the underlying mechanical

principles governing the biomechanical response of vessel walls. Previous studies have quantitatively shown increased collagen fibre straightness as a result of mechanical loading [36–38]. The changes in both collagen and elastin orientation have also been evaluated [51][39–40]. Recent advances in multiphoton technology have allowed investigation of the structure of the tissue.

Multiphoton microscopy is suitable for high resolution and long term imaging of living cells. The beneficial characteristics are its intrinsic three-dimensional resolution, high penetration depth, negligible out-of-focus photobleaching and reduced photodamage [55].

Multiphoton microscopy simultaneously uses two non-linear optical effects, *two-photon excitation* and *second harmonic generation*, for imaging biological tissues. Both types of nonlinear interactions occur in biological tissues without the addition of exogenous contrast agents. Two-photon excited fluorescence has been widely used for imaging cells and tissues (Denk et al. 1990 [56]; Masters et al., 1997 [57]; So et al., 1998 [58]; Squirrell et al., 1999 [59]; Diaspro and Robello, 2000 [60]; Masters and So, 2001 [61]). The second-harmonic generation has recently been employed for biological imaging applications (Guo et al., 1997[62]; Gauderon et al., 1998 [63]). The combination of TPF and SHG has been implemented for the study of cells (Campagnola et al., 2001 [64]; Moreaux et al., 2000a [65]), thin tissue sections (Campagnola et al., 2002 [66]), and for the more practical case of thick, unstained living specimens (Guo et al., 1999 [62]; Zoumi et al., 2002 [67]).

Collagen is a well-documented source of tissue SHG (Campagnola et al., 2001 [64]). Elastin is recognised as a significant source of extracellular matrix autofluorescence (Richards-Kortum and Sevick- Muraca, 1996 [68]), and in particular, its quantum yield is generally higher than the one of other endogenous molecules. Collagen and elastin are important determinants of

the mechanical properties of blood vessels. Their selective visualization is of fundamental interest for the determination of the microstructural origins of mechanical properties.

In this project, TPF and SHG were used to accomplish the selective visualization of the structural components of the arterial wall. Specifically, these methods were used selectively monitor the structural changes of collagen and elastin in thick tissues establishing a microstructural foundation for the observed mechanical properties.

3.3.1. Two-Photon Laser Scanning Fluorescence Microscopy

Two-Photon Laser Scanning Fluorescence Microscopy is a laser scanning microscopy in which contrast is obtained using the fluorescence signal of molecule excited by means a two-photon absorption event. In conventional fluorescence microscopy, fluorescence follows the absorption of a single photon by a molecule raising the molecule to an excited energy state. Two-photon fluorescence microscopy measures fluorescence following the simultaneous absorption of two low-energy photons by a molecule. This phenomenon was firstly predicted by Maria Goppert-Mayer in 1931 [69].

In Figure 19 is represented the Jablonski diagram where fluorescence is emitted from the excited electronic state of a molecule (s1) after excitation obtained by the absorption of single-photon (left) or two photons of lower energy (right). This event occurs because both the two photons interact with the excited molecule nearly simultaneously (about 10-16 s). Importantly, the absorption of the result is a quadratic dependence of the number of an absorbed photon on the excitation light intensity at the difference from the typical linear dependence of conventional fluorescence.

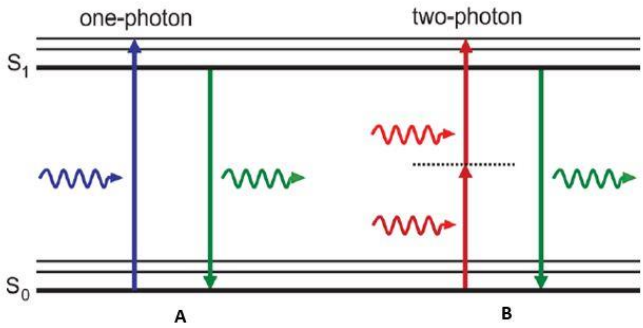

Figure 19 – Jablonski diagram for one-photon (A) and two-photon (B) excitation. Excitations occur between the ground state S0 and the vibrational levels of the first electronic excited state S1. One-photon excitation occurs through the absorption of a single photon. Two-photon excitation occurs through the absorption of two lower-energy photons via short-lived intermediate states. After either excitation process, the fluorophore relaxes to the lowest energy level of the first excited electronic states via vibrational processes. The subsequent fluorescence emission processes for both relaxation modes are the same.

Two-photon microscopy has been used to image the elastin in vascular tissue [56–61][67] The origin of elastin fluorescence is largely debated but it was suggested that the fluorescent cross-linking compound named pyrinoline is the major source of the intrinsic signally. This molecule can be excited in the UV range using an excitation wavelength around 340nm [76], its fluorescence signal is centred at about 400nm [70]. The two-photon cross-section was verified to be in the range of 700-740nm for this molecule. Imaging of elastin in arteries by TPLSM has been accomplished by several researchers [56–61][67]. The elastin in the aorta was examined using TPLSM by Parasassi et al [74]. More recently, Megens et al. [73] demonstrated the use of TPLSM for examining elastic and muscular arteries of mice. They showed that the fenestrae are visible in the internal elastic laminae as non-fluorescent cylindrical patches. The mean diameter of fenestrae was found to be larger in the muscular arteries, 2.1±0.2 µm than in elastic ones, 1.3±0.4 µm. Similarly, there was a significantly higher density of fenestrae in the muscular artery than in the elastic artery. These results indicate that it is possible to use TPF to provide reliable images of elastin structure for the examination of the fenestrae, not only in healthy tissue but in diseased vessels as well.

3.3.2. Second Harmonic Generation Microscopy

Second-harmonic generation (SHG) is a second-order coherent process in which two lower-energy photons are up-converted to one of exactly twice the incident frequency of an excitation laser. It is an instantaneous event that can be assimilated to a scattering phenomenon [77]. Importantly for SHG to occur the medium must lack inversion symmetry. This requires the molecules themselves and the molecules in bulk form to be non-centrosymmetric [63-64]. Imaging of collagen by SHG provides a maximum signal when an excitation wavelength of 700 - 740 nm is applied, although higher wavelengths may also origin the signal depending on the collagen fibril architecture. A high-power IR pulsed laser sources can be used to simultaneously produce imaging of aortic tissue. In Figure 20 is depicted as an example for Second Harmonic Generation of Collagen (green channel) acquired at TU of Graz (Austria).

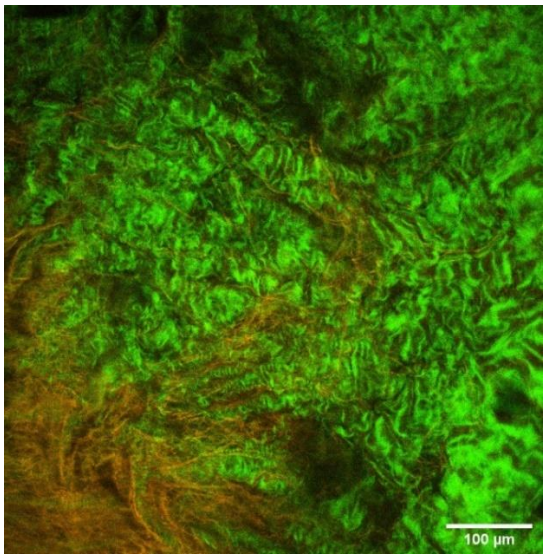

Figure 20 – Multiphoton images of human aorta. TPF of elastin in orange, SHG of collagen in green.

Williams et al. [79] have been able to use SHG to investigate type I collagen from rat tail tendon. They found that the resulting signal comes from the fibre shell, not the bulk of the material. Zoumi et al. [71] combined TPLSM with SHG to examine the effects of distension on

rabbit aorta and porcine coronary arteries. They found that there were significant changes in wall thickness and dimension between zero load, zero stress and distended vessels. Their results prove that multimodal microscopy can be applied to vascular biomechanics as well [71].

3.4. Fluorescence Lifetime Microscopy

Fluorescence lifetime imaging microscopy is a method for measuring and mapping fluorescence lifetimes with microscopic spatial resolution, providing a useful tool to detect, visualize, and investigate the structure and function of biological systems.

Fluorescence lifetime imaging is based on the measurement of the decay in fluorescence intensity across a sample. Functional information may be derived from fluorescence lifetime via its dependence on fluorophore radiative and non-radiative decay rates. It may be used to distinguish between different fluorophore molecules with overlapping spectra or to monitor local environmental perturbations that affect the non-radiative decay rate. This functionality has been exploited to quantify physiological parameters including pH (Sanders et al., 1995 [80]; Szmacinski and Lakowicz, 1993 [81]), [Ca^{2+}] (Lakowicz et al., 1992[82]), and pO_2 (Bambot et al., 1995 [83]). Importantly for the presented applications fluorescence lifetime does not depend on chromophore concentration, a variation of refraction index in the samples and scattering signal.

Fluorescence lifetime imaging (FLIM), in which a map of the spatial distribution of fluorophore lifetimes is displayed, thus provides a powerful functional imaging modality for biomedicine. One promising application is to study protein structure and function, utilizing the sensitivity of their endogenous fluorescence to the physiochemical properties of the environment.

3.4.1. Basic Theory

The fluorescence lifetime of a molecule is the average amount of time that elapses between the excitation state of a molecule and its return to the ground state. Even if fluorescence lifetime is usually referred to the properties of fluorophores as if they were in isolation, in reality, the processes of absorption and emission are studied on populations of molecules and the different properties of the members of the population are revealed by the macroscopic properties of the process. The decay rate of an initially excited population of molecules is described by the following rate equation:

$$\frac{dN(t)}{dt} = -(\Gamma + k)N(t) + f(t) \qquad \textit{Equation 48}$$

where $\mathrm{N(t)}$ is the number of excited molecules at time t, Γ and k are the radiative and non-radiative decay rate constant, and $f(t)$ is an arbitrary function of time describing the time necessary to the excitation of the molecules. The dimensions of Γ and k are sec^{1} and they indicate two substantially different processes. The radiative decay rate constant Γ represents the rate of the emission process, hence it is characteristic of the specific fluorophore molecule. Instead, the nonradiative decay rate constant k is the sum of the rates of all other deactivation processes that occur, so it depends on the fluorophore's interaction with the local environment.

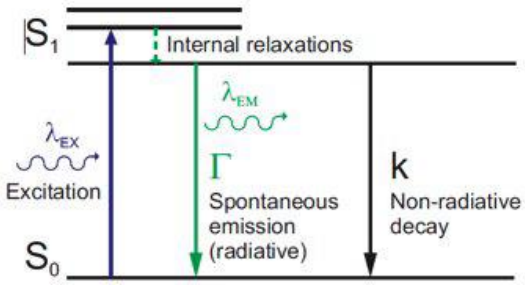

Figure 21 – Energy diagram of the absorption-emission process. The radiative decay rate constant Γ represents the rate of the emission process, hence it is characteristic of the specific fluorophore molecule. The nonradiative decay rate constant k is the sum of the rates of all other deactivation processes, so it depends on the fluorophore's interaction with the local environment.

If the excitation starts at t = 0, the decay equation becomes:

$$\frac{dN(t)}{dt} = -(\Gamma + k)N(t) \qquad \textit{Equation 49}$$

The integration of Equation 49 with the initial conditions $N(t=0) = N_0$ gives:

$$N(t) = N_0 e^{-\frac{t}{\tau}} \qquad \textit{Equation 50}$$

where

$$\tau = \frac{1}{\Gamma + k} \qquad \textit{Equation 51}$$

is the fluorescence lifetime, indicative of the average time a molecule spends in the excited state before returning to the ground state. Fluorescence lifetimes range typically from picoseconds to nanoseconds.

3.4.2. Phasor analysis of FLIM

Fluorescence Lifetime Imaging Microscopy (FLIM) is a fundamental technique in microscopy and it has been demonstrated to be an extremely useful tool to achieve a quantitative analysis of biological samples.

The outcomes of fluorescence experiments are intensity decay profiles. They are originated by the lifetime contribution of the different molecular species existing in the sample, each one of them having multiple lifetime components [71—72]. Also, different

conformations of the same molecule create different decay curve because molecular interactions change the lifetime value [72—73].

At every pixel of the image contributions of several fluorescent species are present, and each one of them can be multi-exponential. Besides, It is possible to collect the light just for a limited amount of time (100—200 μs per pixel) and this results in a small number of photons for every pixel (500—1000) [87].

The common way to analyse FLIM data collected in time domain consists of fitting the decay profile at every pixel using one or more exponential functions to match the different molecular species and their relative quantities with the correspondent decay times and amplitudes. This approach leads to several problems. Many of the fluorescent proteins usually used in microscopy give rise to very complex decay profiles [88]. In a small image, there are about 256x256 pixels and resolving the decay at each pixel requires to fit a function, this is a complex computational task that can be done only by experts [76—77]. Substantially, the approach of exponentials fitting has many limitations: it depends on the initial conditions used and on the hypothesis made on the sample; a proper interpretation of the multi-exponential decay is complex and the number of fitting parameters is high; the fit is very slow.

The phasor approach applied to FLIM is an innovative approach completely different from the fitting of exponentials, able to overcome many of the previous problems. The phasor approach uses a different representation of the decay where each molecular species has its unique identification and each process can be easily recognized. The decay of each pixel is represented in a graphical global view [78—79] and the algorithm used is fit-free and it does not require a priori knowledge on the system. Every chemical species has its own "fingerprint" and so complex systems can be interpreted straight-forward: the contribution of every

different species can be recognized and quantified. All this can be done through a fast analysis.

Phasor Transformations

The phasor plot is a graphical representation of all the raw fluorescence lifetime imaging microscopy (FLIM) data in a vector space. Each pixel in a FLIM image is transformed to a point in the phasor plot. A phasor is a vector described by a module m and a phase ϕ whose coordinates of the phasor in the phasor plot are respectively:

$$g_{i,j}(\omega) = m_{i,j}\cos(\emptyset_{i,j}) \quad \text{Equation 52}$$

$$s_{i,j}(\omega) = m_{i,j}\sin(\emptyset_{i,j}) \quad \text{Equation 53}$$

The component s and g can be obtained according to the following definition Equation 52 Equation 53, where $\mathrm{I_{i,j}(t)}$ is the fluorescence decay measured at a pixel location (i,j), and ω is the frequency of the excitation light and is equal to "$2\pi f$", where f is the basis repetition rate of the pulsed excitation light.

$$g_{i,j}(\omega) = \frac{\int_0^\infty I_{i,j}(t)\cos(\omega t)dt}{\int_0^\infty I_{i,j}(t)dt} \quad \text{Equation 54}$$

$$s_{i,j}(\omega) = \frac{\int_0^\infty I_{i,j}(t)\sin(\omega t)dt}{\int_0^\infty I_{i,j}(t)dt} \quad \text{Equation 55}$$

For a single-lifetime (τ) decays, g(w) and s(w) (Equation 54Equation 55) can be resolved analytically and result in Equation 56 -57:

$$g(\omega) = \frac{1}{1+(\omega\tau)^2} \quad \text{Equation 56}$$

$$s(\omega) = \frac{\omega\tau}{1+(\omega\tau)^2} \quad \text{Equation 57}$$

From these relationships, the lifetime of any single exponential decay is displayed on a semicircle curve centred at (g=0.5, s=0) with a radius of 0.5 in the phasor plot. The plot is called the Universal Circle. On it, for a fixed frequency, longer lifetimes tend to be displayed to the left and shorter lifetimes to the right (see Figure 22)

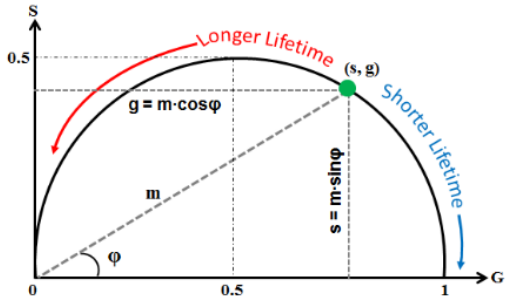

Figure 22 – Graphical representation of a phasor in the phasor plot. The universal circle and phasor are represented. The phasor is identified by its module m and its phase ϕ. g is the x-coordinate of the phasor and s is the y-coordinate of the phasor in the phasor plot.

Phasor Rules

It is important to note that the phasors follow the vector algebra so that multiple lifetime results from the linear combination of their components. Phasor analysis is pretty simple as only a few rules are established allowing the straightforward interpretation of FLIM data; these rules are really easy to apply and they are summarized in Figure 23-25 (E. Gratton, 2018).[93].

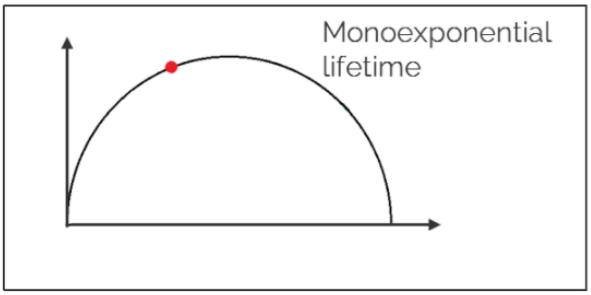

Figure 23 – Single exponential lifetime on the universal circle line

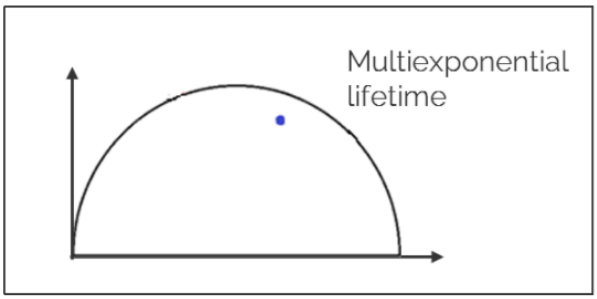

Figure 24 – Multi-exponential lifetime inside the universal circle

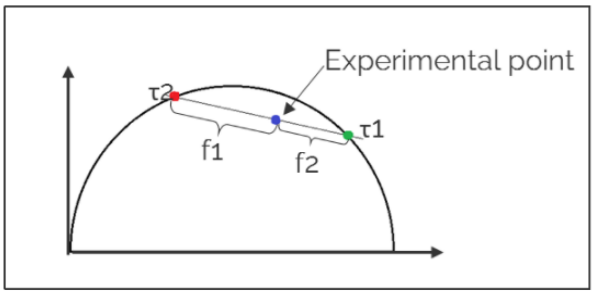

Figure 25 – Two single exponential lifetimes determined by the ratio of the linear combination for a multi-exponential lifetime

4. On the role of material properties in ascending thoracic aortic aneurysms

The content of this chapter was published as a research article in Computers in Biology and Medicine by Cosentino F. et al. 2019. My contribution was aiding in experimental testing and data processing, along with analyzing and processing simulation results.

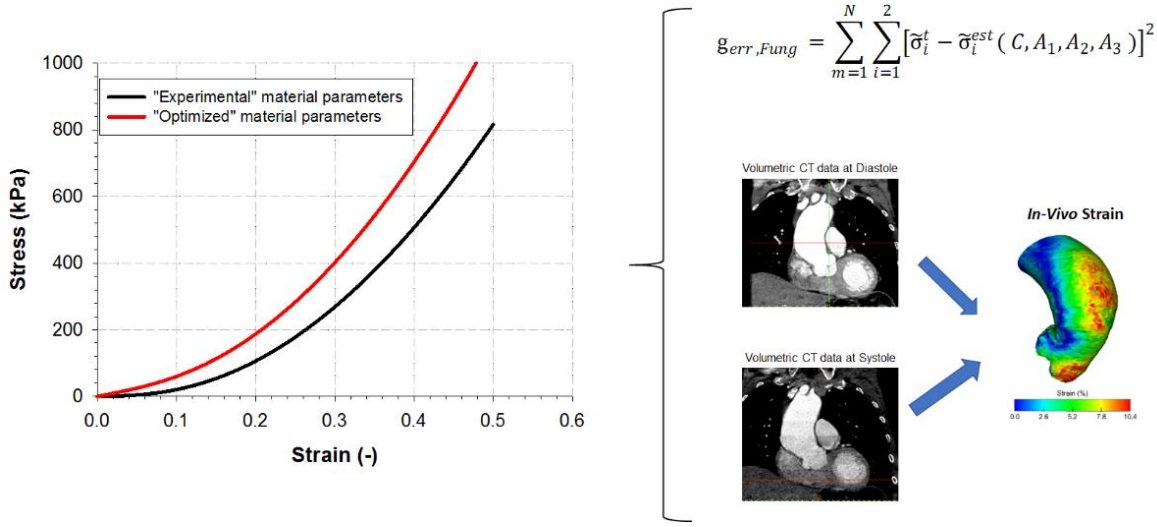

Figure 26 – Graphical Abstract

4.1. Introduction

The ability to obtain patient-specific material properties represent an important challenge for the biomechanical analysis of an Ascending Thoracic Aortic Aneurysm (ATAA). This study aimed to evaluate differences on ATAA-related stress predictions resulting from the elastostatic analysis based on the optimization of arbitrary material properties versus the application of patient-specific material properties determined from ex-vivo biaxial testing. Specifically, the elastostatic analysis relies on the fact that, if the aortic wall stress does not depend on material properties, the aorta has to be statistically determinate. FEAs were

carried out using both optimized and experimentally-derived material parameters to predict and compare the stress distribution using the mean absolute percentage error (MAPE).

4.2. Material and Methods

All nine patients included in this investigation had an electrocardiogram (ECG)-gated computed tomography angiography (angio-CT) for aortic size evaluation and elective surgery for ATAA repair at ISMETT IRCCS hospital institution. ECG-gated CT scans were reconstructed to obtain images at both diastolic and systolic cardiac phases, which were used for the estimation of the diastolic to systolic displacement field of the aortic wall. Aortic valve shape was classified as TAV and BAV based on reconstructed images parallel to the aortic valve plane. The presence of the raphe was used to group BAV according to the fusion of right and left cusps (AP) and the fusion of right and non-coronary cusp (RL). After surgical ATAA repair, excised aortic tissues were stored in a physiologic solution upon biaxial mechanical testing. Table 3 shows patient demographic information, pre-operative aortic diameter and thickness measurements. The study was approved by the local research ethics committee, and all patients signed informed consent before enrolment.

Patient ID	*Age*	*Gender*	*Aortic Valve*	*Type*	*Systolic Diameter (mm)*	*Diastolic Diameter (mm)*	*Thickness* (mm)
P.1	70	Male	BAV	AP	52.0	51.2	2.1
P.2	71	Male	TAV	/	50.4	50.8	1.9
P.3	67	Male	TAV	/	54.8	57.1	2.2
P.4	56	Male	BAV	RL	52.4	53.6	1.8
P.5	58	Male	TAV	/	42.3	45.2	2.2
P.6	67	Male	TAV	/	48.5	49.8	2.8
P.7	78	Male	TAV	/	46.5	47.8	2.1
P.8	63	Female	TAV	/	54.8	55.8	1.7
P.9	68	Male	TAV	/	44.7	45.1	2.3

Table 3 – Patient demographic information

To estimate material property for each patient it was performed equibiaxial mechanical testing using an ElectroForce TestBench system (TA Instrument, Boston, MA). In brief, square specimens (10x10mm) cut form the tissue region located along the major curvature of the aortic ring were extrapolated. Thickness was measured with a calibre for each sample. Five black markers were placed on the intimal tissue surface to evaluate engineering strains along testing directions using a digital video extensometer placed perpendicular to the testing area. During biaxial loading, the specimen was submerged in a bath with 0.9% physiologic saline solution under a controlled temperature of 37^{o}C. A small preload (0.5 grams) was set prior to the displacement-driven testing protocol. After preconditioning, a constant speed of 1mm/min was applied to the four electromagnetic motors to load the specimen under equibiaxial condition. Two 200N load cells were used to record the force along material directions. Data analysis to obtain stress and strain were calculated as defined in the constitutive modelling section.

Constitutive Modelling

FEAs were carried out using two specific classes of materials: a) the isotropic Yeoh material model in the two-term formulation and b) the orthotropic Fung-exponential model, which is often used in soft tissue biomechanics. Both models adopt the homogenous, incompressible and hyperplastic description of ATAA wall mechanics.

In short, the two-term Yeoh constitutive model involves a strain energy density function $W(I_1, I_2, \dots . I_n)$ with $I_k(k = 1,2, \dots . n)$ the $\mathrm{k^{th}}$ pseudo-invariant of the left Cauchy-Green strain tensor takes the form:

$$W(I_1, I_2, \dots I_n) = W(I_1) = c_1^{(Y)}(I_1 - 3) + c_2^{(Y)}(I_1 - 3)^2 \qquad \textit{Equation 58}$$

with $c_1^{(Y)}$ and $c_2^{(Y)}$ are material model parameters indicative of the mechanical properties of the ATAA wall. In the following we assume that the material undergoes a cylindrical state of strain along the principal directions $\mathbf{n}_1$ and $\mathbf{n}_2$ defined in terms of the principal stretches $\lambda_1 = \lambda_2 = \lambda$, applied to the wall of the ATAA. Kinematic incompressibility restraint, namely, $\det(\boldsymbol{B}) = \lambda_1^2\lambda_2^2\lambda_3^2 = 1$, yields the condition on the principal stretch$\lambda_3 = 1/\lambda^2$ along the principal direction $\mathbf{n}_3$ with $\boldsymbol{n_3^T n_j} = 0$ j=1,2.

The small thickness of the ATAA wall can be treated as a membrane so that the principal stress $\sigma_{33} = 0$ allowing for the straightforward evaluation of the Lagrange multiplier $\mathbf{p}$. In these circumstances the membrane Cauchy stresses read:

$$\sigma_{11} = \sigma_{22} = 2\left(\lambda^2 - \frac{1}{\lambda^4}\right)\frac{dW(I_1)}{dI_1} \qquad \textit{Equation 59}$$

From this equation it is possible to calculate the second Piola Kirchoff stress tensor explicitly:

$$S_{11} = S_{22} = 2\left(1 - \frac{1}{\lambda^6}\right)\frac{dW(I_1)}{dI_1} \qquad \textit{Equation 60}$$

and $S_{33} = 0$ according to the membrane stress state assumption. The free energy function for the Fung model of material hyperelasticity read:

$$W = \frac{c^F}{2}(e^Q - 1) \qquad \textit{Equation 61}$$

With

$$Q = (a_1\lambda_1^2 + 2a_4\lambda_1\lambda_2 + a_2\lambda_2^2) \qquad \textit{Equation 62}$$

where c is a material parameter $[\frac{\mathrm{N}}{\mathrm{m}^2}]$ and a_1, a_4, a_3 are dimensionless parameters. The Cauchy stresses obtained from Fung expression of free energy function are expressed as:

$$\sigma_{11} = 2\lambda_1^2 c_1^{(F)} e^Q (a_1\lambda_1 + a_3\lambda_2)$$ *Equation 63*

$$\sigma_{22} = 2\lambda_2^2 c_1^{(F)} e^Q (a_3\lambda_1 + a_2\lambda_2)$$ *Equation 64*

In the case of negligible shear stress, the normal components of the second Piola-Kirchoff stress tensors are related to the Cauchy stress by:

$$S_{11} = \frac{\sigma_{11}}{\lambda_1^2} = 2c_1^{(F)} e^Q (a_1\lambda_1 + a_3\lambda_2)$$ *Equation 65*

$$S_{22} = \frac{\sigma_{22}}{\lambda_2^2} = c_1^{(F)} e^Q (a_3\lambda_1 + a_2\lambda_2)$$ *Equation 66*

Inverse Method to Identify the ATAA Mechanical Properties from the "true" strain field

The elastostatic analysis for the evaluation of material constitutive parameters proposed by Liu et al. [94] is based on the main premise for which the stress distribution is statically determinate. Thus, for a given ATAA deformed configuration (ie, the peak of systole) and known loading condition (ie, the diastolic-to-systolic displacement field), different material parameters and constitutive models will give nearly the same stress field. In this way, an "almost-true" stress field at systole can be approximately obtained by an infinitesimal linear elastic model with sufficiently stiff material parameters. This fact has been theoretically justified by Miller and Lu [95] and numerically verified by Joldes et al. [96]. Given the constitutive model with an initial guess of material parameters (ie, $c_1^{(Y)}$ and $c_2^{(Y)}$ for Yeoh model and $c_1^{(F)}$, a_1, a_2, a_3 for the Fung model) by using the constitutive equations and deformation relationship between the two loading states, an optimization algorithm allows to find the "true" material parameters such that the difference between the estimated and

"almost-true" stress fields is minimized. Thus, the objective of the optimization process was to find a set of material parameters that minimize the difference between the "almost-true" systolic stress, $\tilde{\sigma}^{t}$, and estimated systolic stress, $\tilde{\sigma}^{est}$, for each element as:

$$g_{err,Yeoh} = \sum_{m=1}^{N} \sum_{i=1}^{2} \left[\tilde{\sigma}_i^t - \tilde{\sigma}_i^{est}(c_1^{(Y)}, c_2^{(Y)}) \right]^2 \quad \textit{Equation 67}$$

$$g_{err,Fung} = \sum_{m=1}^{N} \sum_{i=1}^{2} \left[\tilde{\sigma}_i^t - \tilde{\sigma}_i^{est}(c_1^{(F)}, a_1, a_2, a_3) \right]^2 \quad \textit{Equation 68}$$

where N is the number of elements used in each model and i is the component index of the principal stress. Equation 67 Equation 68 were used for the estimated systolic stress as determined from the Yeoh and Fung models, respectively.

The optimization was implemented in MATLAB (v2018, Mathworks, MA, USA). Nonlinear least-squares algorithm with trust-region-reflective was used for the optimization of Yeoh material parameters using $c_1^y > 0 \; and \; c_2^y > 0$ as lower bound. For the Fung-exponential form, physically meaningful and plausible material parameters were obtained by enforcing the convexity of the strain energy function and thus performing constrained minimization. For planar biaxial loading of soft tissue, strict convexity physically implies that the projections of the contour of $\mathrm{W(C)}$ on the $\lambda_1 - \lambda_2$ plane form a convex surface. It can be shown that if $c_1^{(F)} > 0$, then Eq. 65-66 is likely convex if and only if $a_1 > 0$, $a_2 > 0$ and $a_1 \, a_2 - a_3^2 > 0$

For the estimation of the "almost-true" systolic stress distribution, we selected a very stiff material for the aortic wall (E=2×10^4 GPa and v=0.49) to obtain Cauchy stress. As initial guess of material descriptors, we used the population-average material properties reported by Pasta et al. [97] for the two-term Yeoh model and by Azdani et al. [98] for the Fung model of ATAAs. For each optimization procedure, principal stresses were imported in MATLAB by

postprocessing of ABAQUS models, and the optimization was done to obtain the optimal material parameters.

Computational Study

Reconstructed angio-CT images were used to segment the ATAA wall at both end-diastolic and peak-systolic cardiac phases using the medical imaging software Mimics (Mimics v20, Materialise, Leuven, BE). Semi-automatic threshold-based segmentation of the aortic lumen allowed us to obtain a point cloud (resolution of 0.3 mm), which was triangulated to generate a surface mesh of both diastolic and systolic ATAA geometries. Using an algorithm previously developed by our group in MATLAB (v2018, Mathworks, MA, USA), the point cloud of the diastolic aortic-luminal surface was projected normally onto the systolic aortic-luminal surface to determine the displacement field as the Euclidean distance between closest points. The estimated diastolic-to-systolic displacement field was then implemented as a boundary condition in the FEA model for estimating wall stresses.

For each patient, FEAs were developed using the reconstructed ATAA geometry at diastole, which was meshed with quadrilateral and triangular membrane elements in ABAQUS/Explicit solver (v2018, SIMULIA Inc, Providence, RI). Grid convergence led an element size of 0.7 mm to obtain a reproducible stress analysis of the human thoracic aorta. Uniform material properties were adopted for the whole aortic wall while the thickness measured for each sample was used for each ATAA model. The diastolic-to-systolic displacement field was interpolated on the closest node of the structural mesh using MATLAB while the distal end of the descending aorta was fixed in all directions as a boundary condition. Material fibre direction was set using multiple cylindrical coordinate systems with origins in the centerline of the aneurysmal aorta. The ATAA wall was modelled using two

constitute formulations to assess the role of the isotropic- and anisotropic behaviour on the resulting stress distribution.

The density of the aortic tissue was 1060 kg/m3. In the Abaqus/Explicit solver, ATAA wall mechanics was modelled as a quasi-static process while the energy was monitored to ensure the ratio of kinetic energy to internal energy remains less than 10%. The adequate time step was applied while an element by element stable time increment estimate, coupled with a "variable mass scaling technique," reduced the computational cost of each simulation. Mass scaling was performed by scaling the masses of elements whose stable time increments was less than the user-supplied time increment of 1x10^7 so that the element stable time increment for these elements becomes equal to the user-supplied time increment. This approach has a minor effect on stress analysis. The numerical strategy is here summarized:

1. For the estimation of the "almost-true" stress distribution, the FEA model of each patient was loaded with a uniform peak systolic pressure distribution of 120 mmHg in a very stiff aortic wall ($\mathrm{E}=2\times10\text{^}4\ \mathrm{GPa}$ and $\mathrm{v}=0.49$);
2. The resulting "almost-true" stress distribution was adopted to optimize the population-average material descriptors of Yeoh and Fung constitutive relationships. This step allowed us to find the optimal material parameters for patient-specific;
3. The second set of simulations was performed using the optimal material properties and the diastolic-to-systolic displacement to find realistic deformation of ATAA wall.
4. The third set of simulations was carried out using the displacement field as the boundary condition but using the experimental material properties from test Then, results were compared to those observed for the second set of simulations.

4.3. Results

Experimental raw data from equibiaxial testing are shown as Piola-Kirchhoff stress versus engineering-strain plots for ATAAs in both circumferential and longitudinal directions (Figure 27).

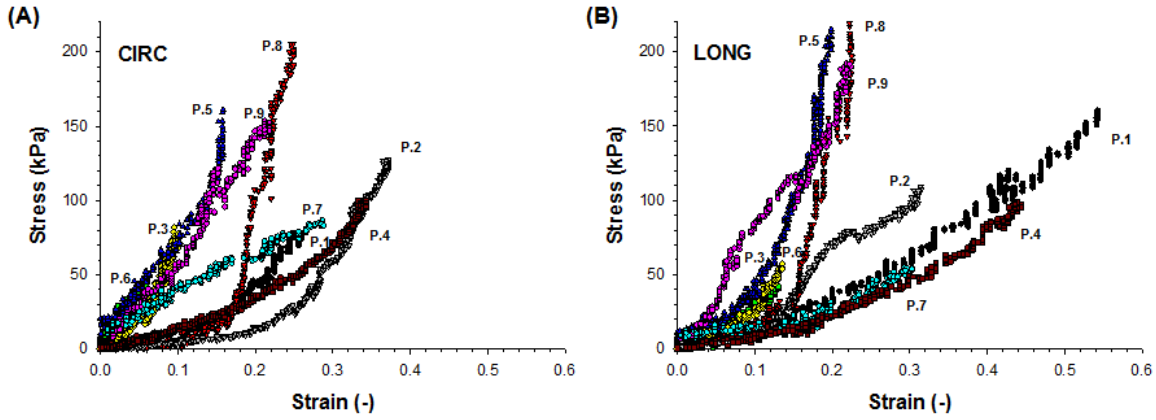

Figure 27 – Equibiaxial raw stress-strain data for ATAA specimens in (A) circumferential (CIRC) and (B) longitudinal (LONG) directions; labels indicate specimens obtained from the same patient.

Most of the stress-strain data presented a linear part, related to the elastic properties of the aneurysmal aortic tissue, followed by an exponential part related to the collagen fibre recruitment. These parts were separated by the "yield point", which is more likely to define the in-vivo stress range.

For a given tissue specimen, there was no remarkable difference in material response between longitudinal and circumferential directions, suggesting isotropic mechanical behaviour for ATAA wall as previously found [97].

Stress-strain data were successfully fit by both the isotropic and anisotropic constitutive models, and the material parameters for each patient were estimated (Table 4)

Patient ID		*Yeoh*			*Fung*				
		C_{10} (kPa)	C_{20} (kPa)	R^2	C	A1	A2	A3	R^2
P.1	exp	13.1	147.9	0.990	5.6	6.7	6.6	4.7	0.970
	pre	10.6	149.1		46.5	6.9	6.7	5.2	
P.2	exp	31.1	42.6	0.990	29.9	32.3	53.2	12.4	0.984
	pre	38.6	44.1		13	24.8	52.8	-3.4	
P.3	exp	64.9	134.5	0.980	42.0	15.4	1.0	1.4	0.990
	pre	39.2	118.6						
P.4	exp	38.4	101.1	0.990	55.8	3.1	10.6	0.1	0.991
	pre	5.9	106.7		25.9	2.7	10.5	0.7	
P.5	exp	75.6	884.0	0.970	14.5	29.2	31.1	1.7	0.982
	pre	93.5	882.0		16.1	18.0	31.0	-7.2	
P.6	exp	50.4	75.1	0.998	32.8	8.1	12.7	1.2	0.978
	pre	20.7	73.1		49.4	9.5	12.7	1.5	
P.7	exp	3.8	86.7	0.990	99.7	2.5	3.8	-0.2	0.998
	pre	41.1	105.3		219.9	14.1	16.7	-13.6	
P.8	exp	15.4	242.0	0.974	5.8	21.9	20.5	-7.8	0.935
	pre	18.2	241.9		3.4	10.2	20.5	6.4	
P.9	exp	121.8	446.8	0.968	55.6	11.0	0	0.0	0.914
	Pre	23.4	249.7		26.8	7.4	0.1	1.0	

Table 4 – Constitutive material parameters as obtained by the fitting of experimental biaxial testing (exp) and by the inverse method (opt); coefficient of determination (R^2) refer to experimental data

Fitting was able to accurately reproduce the non-linear behaviour of experimental data (R^2 > 0.91 in all cases) so that material descriptors can be considered as determinants of the biomechanical behaviour of ATAA wall. After running the elastostatic optimization analysis, material parameters were found close to those obtained from the fitting of the experimental stress-strain curves. We observed that even a variation of 10% on the initial guess of the constitutive parameter set did not determine remarkable changes on the optimal material parameters.

Strain analysis

Figure 28 shows the distribution of the diastolic-to-systolic strain field as well as the experimental stress-strain curve from biaxial testing of the aortic tissue specimen cut from

the same patient. It can be observed that the range of "true" strain in the circumferential direction is below the yield strain, which is the value of the strain at yield point before reaching the steep increase in the stress-strain response of tested aortic tissue specimen.

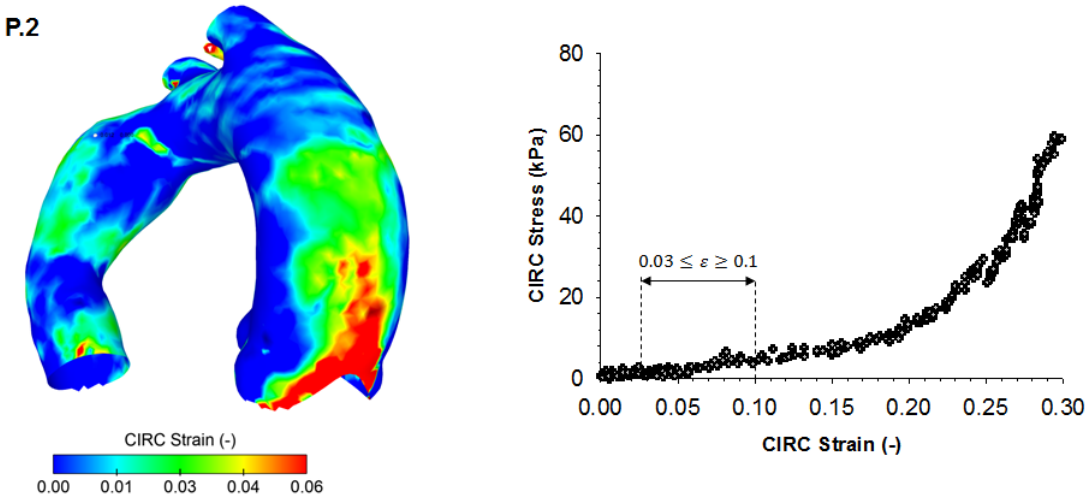

Figure 28 – Representative distribution of circumferential strain for patient P.2 as obtained after optimization procedure and raw stress-strain data in the circumferential direction showing the range of strain.

Most patients experienced low strain at CT imaging, except for patients P.6 and P.9 who experience strains remarkably above the yield strain.

	P.1		*P.2*		*P.3*		*P.4*		*P.5*		*P.6*		*P.7*		*P.8*		*P.9*	
	min	max	min	min	min	min	min	max	min	max	max	min	min	max	max	max	max	min
ε_{circ}	0.01	0.15	0.01	0.03	0.04	0.04	0.05	0.01	0.02	0.18	0.01	0.16	0.01	0.13	0.05	0.10	0.01	0.13
ε_{yiel}	0.16		0.24		0.25		0.17		0.15		0.09		0.21		0.17		0.08	

Table 5 – Range of "true" strain determined for each patient and corresponding yield strain extrapolated from raw stress-strain data of biaxial testing

This can be determined by high blood pressure induced by hypertension, increased stretch and twist of the aortic vessel due to heart beating and local changes of material properties or tissue thickness, exposing the aneurysmal aorta at greater risk of complications than other patients.

"Almost-true" stress computation

The distribution of "almost-true" stress determined by the simple linear-elastic FEA with the stiff elastic modulus was compared to that obtained at the end of an optimization procedure for each patient simulation. Specifically, the maximum principal stress exerted on the ATAA wall was used as an indicator of intramural stress of aneurysmal aorta. Figure 29 shows that the stiff ATAA model had a stress distribution similar to that of Fung model but different from that shown by the Yeoh model.

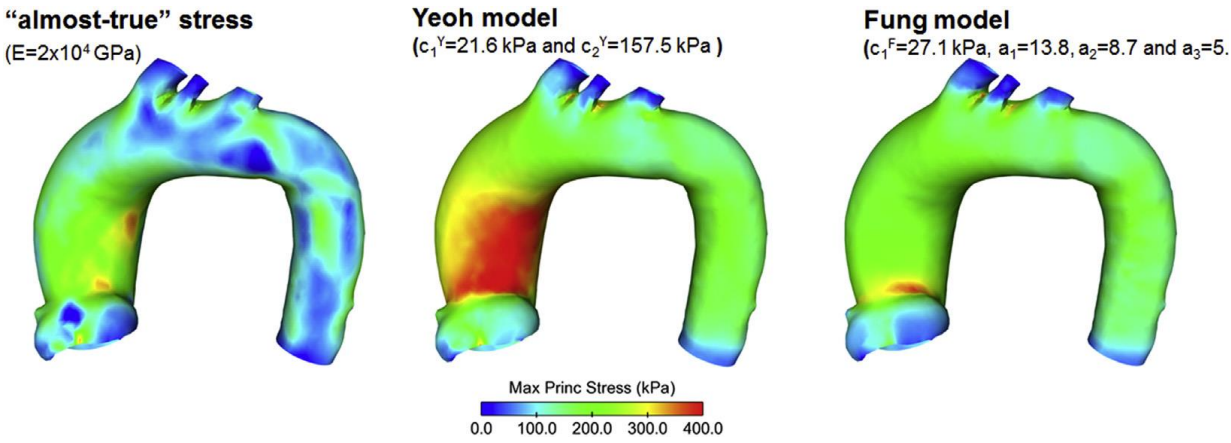

Figure 29 – Distribution of "almost-true" stress determined using a very stiff material for the aortic wall as compared to stress from the optimal material properties for the Yeoh and Fung constitutive models of P.1.

The mean absolute percentage error (MAPE) was calculated for each patient as a measure of differences among simulation approaches. For the patient P.1 shown in Figure 29, the MAPE was nearly 30% between the "almost-true" and Yeoh models and 8.5% between the "almost-true" and Fung models. For other patient cases, we found errors in the range of 6–18%.

Biaxial testing of optimal vs experimental material parameters

Optimized material parameters obtained from elastostatic analysis were used to determine the stress-strain response under equibiaxial loading conditions in an FEA reproducing the experimental testing of the aortic tissue sample. Then, the stress-strain curves were plotted together with the experimental testing data (see Figure 30). P.2 with small strain field exhibited a practically equivalent stress-strain response with both experimental and elastostatic material descriptors. At strain of 14%, P.6 had the largest discrepancy of 24% in stress predictions between optimized and experimental material descriptors of two-term Yeoh constitutive model.

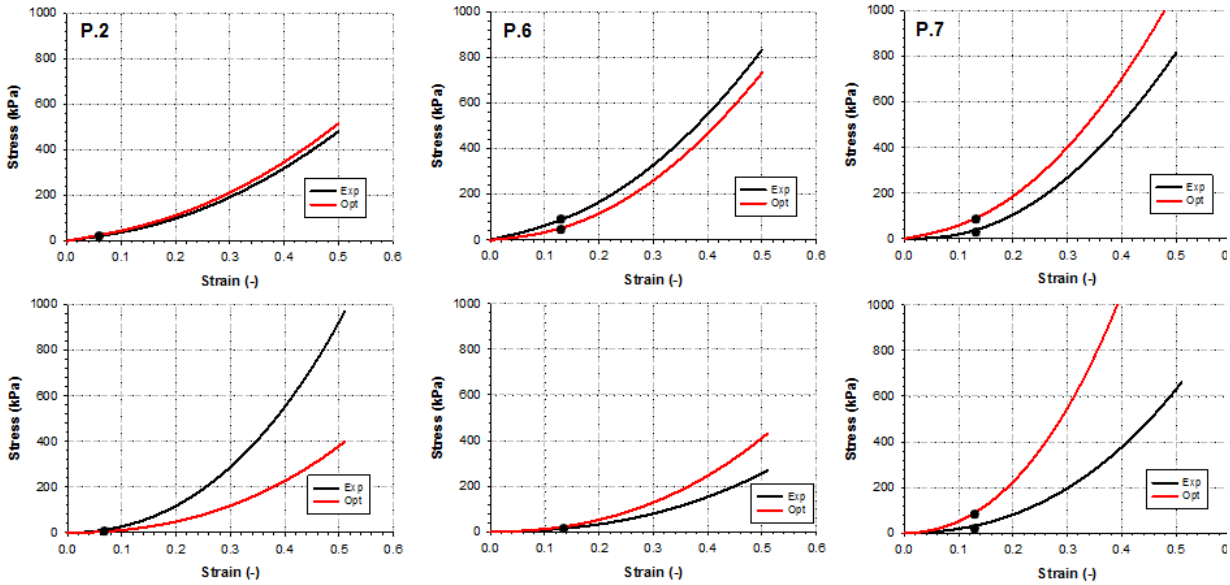

Figure 30 – Comparison of stress-strain response curves under equibiaxial loading condition for three representative patients as modelled with two-term Yeoh constitutive model (top row) and Fung-exponential model (bottom row) using experimental and optimized material parameters; dots indicate the maximum value of peak systolic strain.

Patient-specific FEA of optimal vs experimental material parameters

Figure 31 illustrates predicted wall stress distributions computed by patient-specific material descriptors determined from experimental biaxial testing of Yeoh model. Local maxima of wall

stress were mainly placed near the maximum curvature of the ascending aorta, just above the sino-tubular junction.

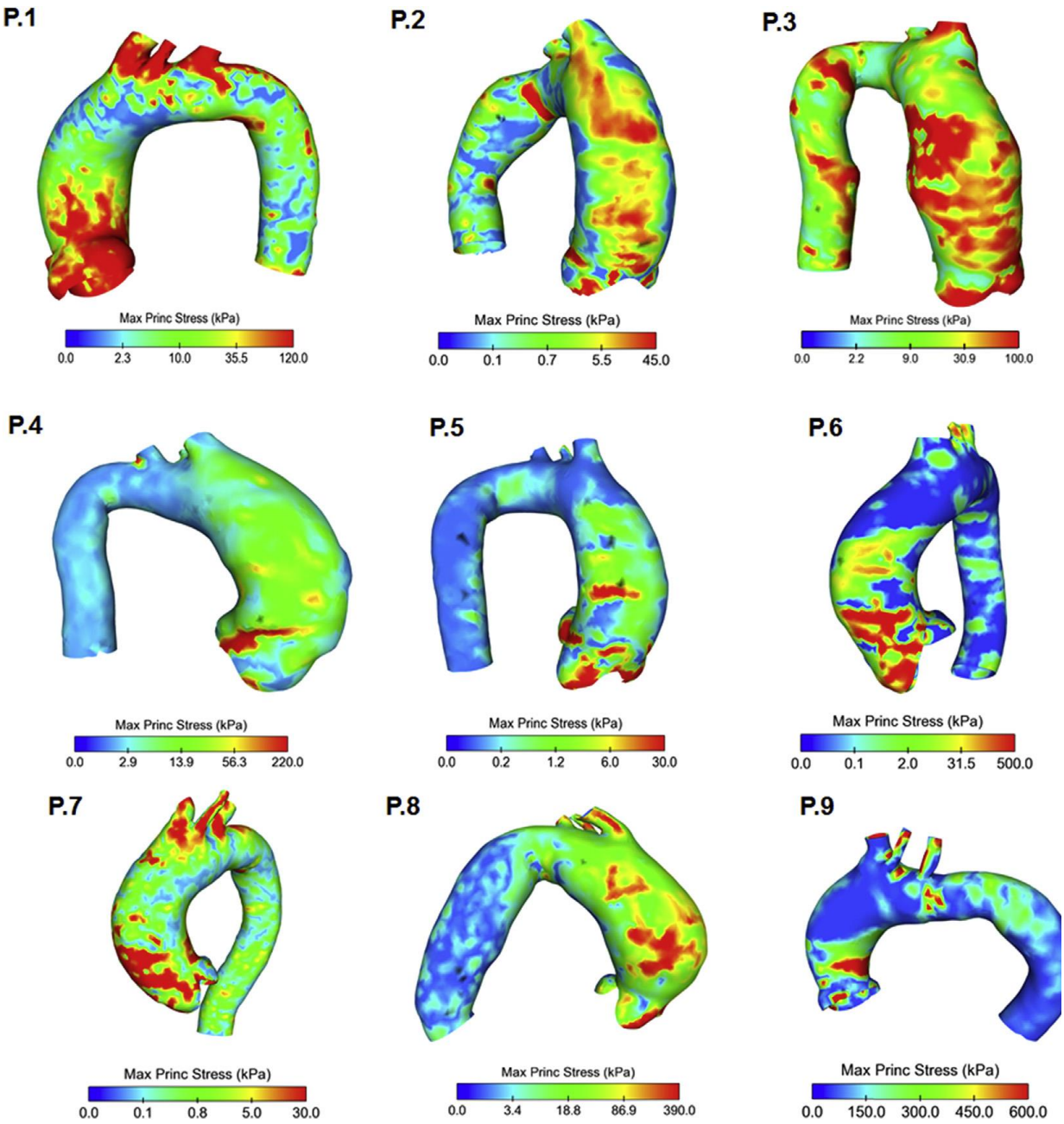

Figure 31 – Distribution of patients-specific stress as quantified by the maximum principal stress at peak systole for all patients using the Yeoh constitutive material formulation based on the fitting of experimental data.

Similarly, Figure 32 shows predicted wall stress maps resulting from the experimentally-based material fitting using the Fung model. It can be observed that stress distributions are similar

among constitutive formulations (ie, Yeoh versus Fung model) when patient-specific material parameters are adopted.

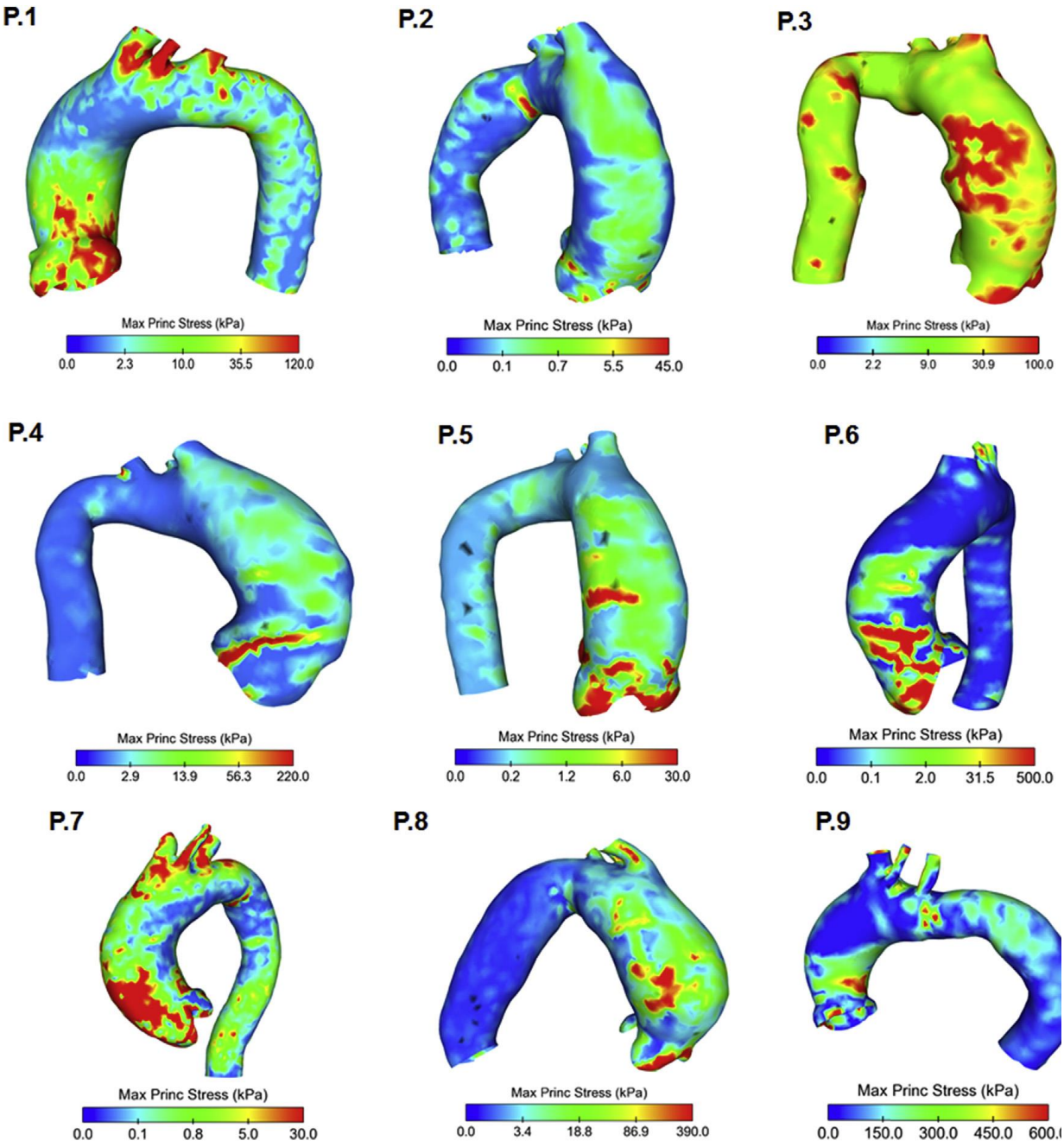

Figure 32 – Distribution of patients-specific stress as quantified by the maximum principal stress at peak systole for all patients using the Fung constitutive material formulation based on the fitting of experimental data.

Although biaxial testing results of optimal versus experimental material parameters are encouraging, we found considerable discrepancies for the patient-specific stress predictions between the optimal material parameter set versus the experimentally-derived set (Figure

33). The MAPE was calculated for each patient and evinced highly variable differences from patient to patient and the type of constitutive formulation (see Table 6).

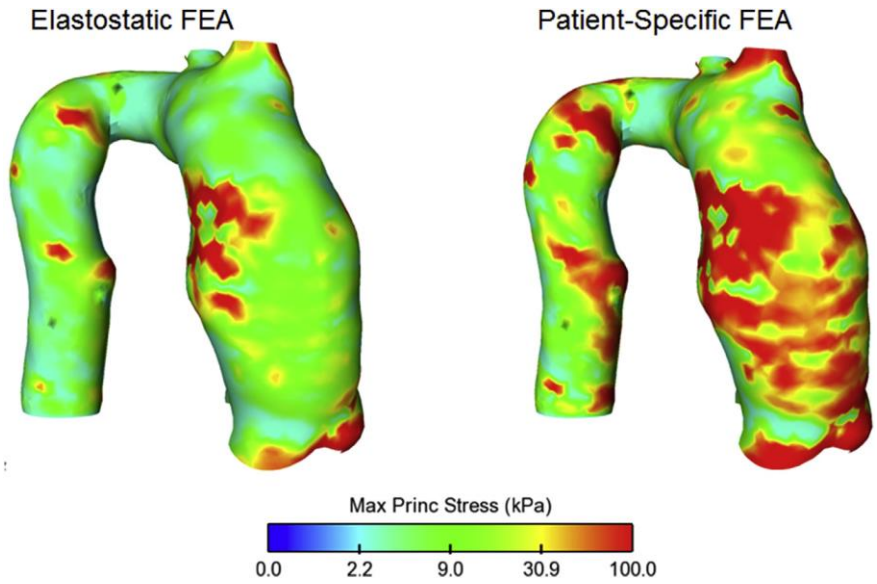

Figure 33 – Comparisons of stress distribution for P.3 using the material parameters obtained by the FEA using the statically-determinate optimization procedure versus the FEA using patient-specific material parameters.

	P.1	*P.2*	*P.3*	*P.4*	*P.5*	*P.6*	*P.7*	*P.8*	*P.9*
Yeoh	0.7105	0.7398	0.7575	0.4520	0.5303	0.7034	0.2138	0.1754	0.3245
Fung	0.7683	0.1140	0.6022	0.3241	0.7539	0.7130	0.0349	0.2198	0.7034

Table 6 – Mean absolute percentage error (MAPE) of maximum principal stress between experimentally-derived and optimized material parameters

4.4. Discussion

In this study, we exploited the appealing concept of obtaining reasonably and accurate stress solutions of aneurysm mechanics using an inverse approach, and thus without invoking accurate material descriptors that are hard to know before surgical management of ATAAs. We optimized population-average material parameters with respect to a "the "almost-true"

stress fields obtained with an infinitesimal linear elastic model based on a sufficiently stiff Young modulus [94]. The so-recovered material parameters were implemented in FEAs, and then stress distributions of nine ATAA geometries were compared to those predicted when patient-specific material descriptors are estimated from the fitting of ex-vivo testing data of aortic tissue specimens collected from the same patient. We observed that the stress-strain response under equibiaxial loading predicted by the elastostatic analysis was consistent with the experimental material behaviour if strain was low (the largest difference of 24% at the strain of 14%). This was in agreement with findings documented by Liu et al. [94]. However, the discrepancy on predicted stress distributions was considerable, depending on the adopted constitutive model and ATAA shape, when FEAs were performed on patient anatomies. Although the stress analysis of abdominal aortic aneurysms did not depend on material properties [99], the modelling of the ascending aorta as a statically-determinate structure needs further understanding so that the role of material properties is still important for realistic and accurate stress predictions.

Identification of patient-specific material parameters of ATAAs deserves important interest as FEAs rely on population-average values of material properties for those patients undergoing close monitoring of the aneurysm size. In risk predictions of aneurysm failure, FEAs based on patient-specific material descriptors were carried out in very few studies restricted to patients who underwent elective surgical repair of ATAA wall to derive the material behaviour from uniaxial or bulge inflation tests [100 - 101]. The role of material properties in computational growth and remodelling analyses maybe even more remarkable as stress estimations are strongly dependents on local material changes [102]. To avoid ex-vivo material testing, inverse approaches allows to estimate material descriptors; however, inverse analysis involves a complex non-linear problem [103]. Most of the inverse approaches

are commonly time-consuming due to continuous interaction with the FEA solver [39]. For the ascending aorta, Trabelsi et al. [38] proposed an inverse method in which the target variable was the volume variation of the aorta measured from ECG-gated CT scans. They assumed a linear relationship between the constitutive material parameter and the volume of the aortic luminal surface and then carried out eight FEA analyses for each patient to build datasets for several CT measurements of ATAA volume at systole and mid-cardiac phase. The error attributed to this approach was 0.6% on estimated CT volume and 9.6% on the predicted stress response under equibiaxial test simulations [104]. In agreement with our findings, the statically determinate inverse approach proposed by Liu et al. [94] for the Gasser-Holzapfel-Ogden constitutive model elastostatic analyses and experimental tests estimated in a previous investigation of the same group [100]. In their patient study group, patient-specific FEAs on ATAA anatomies were not done because of lack of both CT and tissue data, without quantification of stress changes computed with either experimental or elastostatic-based material parameters.

Generally, the stress of a deformable body depends not only on its geometry, load and boundary conditions but also on the mechanical properties of constituents. One of the obstacles standing before the biomechanics community is the difficulty in obtaining patient-specific properties of tissues given the absence of a methodology to non-invasively estimate stress in-vivo. Notwithstanding, there is an emerging interest from several groups in reformulating computational mechanics in a new paradigm so that computational stress predictions are weakly sensitive to the variation of mechanical properties when the deformed configuration is given [95]. This paradigm can apply to the non-linear elastic material because the stress in such material depends on the relative deformation among two definite configurations. If one of them is known, the other can be solved from equilibrium, which is

dominated by in-plane stress for thin-walled structure treated as a membrane. From the analysis of ECG-gated CT images, we observed that strain at deformed configuration bears to the linear-elastic part of the experimental stress-strain response, thereby supporting in part the static determinacy of the aneurysmal wall. In this way, the inverse problem can be directly formulated using the constitutive law as here presented or shown by other studies [94][105] and without the need of continuous interaction with the FEA solver. Using the Fung model, Miller et al. [95] investigated the sensitivity of the stress solution with respect to material parameters and constitutive model in three intracranial aneurysm geometries under static determinacy. The inverse stress solution was far less sensitive to the material description as, for instance, the 100 times increase in the stiffness parameter *C* of the Fung model led to a 2.9% error in the maximum principal stress prediction. The major limitation of this study is that comparisons of stress predictions were carried out assuming the experimentally-derived material parameters as the true material descriptors of the ATAA wall, but these can be indeed different from the in-vivo condition. However, there is no methodology to in-vivo estimate the material behaviour so that experimental material parameters are the most accurate ATAA material descriptors. FEAs were based on homogenous thickness and material properties for the whole aorta but there exist evidence of regional changes in the material properties and thickness along the vessel circumference [106] and from the aortic root to the distal ascending aorta [107]. It should be mentioned that the optimization procedure can be modified to account for heterogenous thickness and regionally-dependent material properties by slightly altering the workflow and evaluating the objective function element-by-element. Disregarding the presence of residual stresses and considering the arterial wall as a 3D membrane with a uniform thickness can be considered as additional limitations of the current work. It was assumed that the aortic wall behaves as a membrane with no bending

moments or no through thickness-shear, although regions near the branches may not satisfy the membrane assumption. The orientation of elastic fibre was not considered in FEAs, and this may alter the stress distribution. Calliper-based measurements of tissue thickness can lead to errors which in turn affect aortic wall stress predictions.

4.5. Conclusion

We conclude that the modelling of the ascending aorta as a statically determinate can lead to errors on wall stress predictions in patient-specific FEAs since aortic wall stress was found to depend on the type of constitutive model and ATAA geometry. Static determinacy needs a better understanding of its application to determine ascending aortic aneurysm mechanics so that patient-specific material descriptors as determined by ex-vivo material testing are advocated for reliable accurate stress predictions of ATAA wall mechanics.

Acknowledgements

This work was supported by a “Ricerca Finalizzata” grant from the Italian Ministry of Health (GR-2011-02348129). Federica Cosentino thanks the Fondazione RiMED and Ministry of Education, University and Research (MIUR) for supporting her PhD programme.

5. Multiscale Biomechanical investigation of ATAA

This chapter presents unpublished data and analyzes carried out with the contribution of Prof. Gerhard A. Holzapfel. My contribution to the work relates to image processing, to extract fibre orientations, to performing experimental tests, data processing and writing.

Ascending thoracic aortic aneurysms (ATAAs) are characterized by abnormal dilation of the ascending aorta, where the vessel exceeds its normal diameter of 2-3 cm [20].

Aneurysms are often affected by wall thinning, structural disorganization, loss of vascular smooth muscle cells, and extracellular matrix components such as elastin, collagen and fibrillin [Humphrey, 2013 [108]]. Current risk assessment and patient diagnosis are based primarily on vessel diameter. If the ATAA diameter exceeds a threshold of approximately 5-6 cm [Davies et al.,2002 [109], Elefteriades, 2002 [110], Coady et al., 1999 [111] or a growth rate of 0.5 cm/year [Saliba and Sia, 2015 [112]], surgical intervention is recommended. When ATAA risk is assessed solely with measurement-based techniques, however, mechanical and structural changes, which are well-known to occur in the ATAA pathology [Isselbacher, 2005 [113], Garcia-Herrera et al., 2012 [114], Vorp et al., 2003 [115], Okamoto et al., 2002 [116]], cannot be considered. The inefficiency of measurement-based diagnosis was shown by Vorp et al. [Vorp et al., 2003 [117]], who reported a 5-year mortality rate of 39% for ATAAs below the 6 cm diameter threshold and 62% for those above the 6 cm diameter threshold. Furthermore, Vorp et al. found no correlation between aneurysm diameter and tensile strength. Failure contributors in the ATAA pathology must be better understood to help inform physician decisions and improve patient outcomes. It is also widely agreed that the mechanical environment and properties of arteries play an important role in the origin and progression of CVD. Therefore, detailed knowledge of their mechanical behaviour is essential

for the improvement of surgical and non-surgical procedures, as well as for the development of prosthetic materials and artificial tissue equivalents.

Recent studies have quantised non-aneurysmal and aneurysmal aortic tissue mechanical response through various loading configurations including bulge inflation [85–86], uniaxial extension [87–90], biaxial extension [119], [91–93], peel [94–95], and shear [124] testing regimes. As a general rule, those studies found significant anisotropy, with the tissue stronger in the circumferential than in the axial direction [97–99],[121]. Aneurysm tissue is generally stiffer [115][126, Ch. 3] but weaker [115][127] than healthy tissue, perhaps due to elastin degradation in the aneurysm pathology. Regional heterogeneity has also been observed, with differences between the lesser and greater curvature wall mechanics [21][105–106]. Although none of these trends was absolute, they provide extensive insight into aneurysm mechanics. For stress estimation, finite-element modelling has been the most popular approach [101][103–106]. These models, taken collectively, describe a complex, heterogeneous stress field in the tissue.

Despite much progress in understanding ATAA mechanics using experimental testing and computational model, the comprehensive mechanic of ATAA tissue and his connection with the microenvironment, has not been well documented. In the pathological case of ATAAs, remodelling of the microstructural components occurs. Typically, along with diameter enlargement and wall thinning, the pathology is accompanied by disorganization or loss of elastin, collagen, VSMCs, and fibrillin [Campa et al., 1987 [133], Humphrey, 2013 [108]]. Due to the complex nature of the ATAA pathology, it is difficult to understand how mechanical loading changes on the tissue, and thus its underlying components. Changes in the structural components of aortic walls such as the ground matrix and the embedded families of collagen fibres have been shown to play a significant role in the pathogenesis of aortic degeneration.

This study aimed to assess the relationship between the mechanical behaviour and microstructure of the human aorta. The tissue samples from 10 human ascending thoracic aortas (ATA) are systematically analysed and compared with respect to their structural and mechanical differences. The collagen microstructure is examined by analysing data from second-harmonic generation imaging after optical clearing. Samples from ATAA are mechanically investigated using biaxial stretching tests. A bivariate von Mises distribution was used to represent the continuous fibre dispersion throughout the entire thickness, and to provide two independent dispersion parameters to be used in a recently proposed material model. A novel set of three structural and three material parameters is provided. With the structural parameters fixed, the material model was fitted to the mechanical experimental data, giving a very satisfying fit although there are only three material parameters involved.

The biaxial mechanical properties and collagen fibre architecture were studied in different regions of the aortic ring. Understanding the underlying mechanisms, incorporating important structural features, will help to improve our understanding of congenital defects of the ATAA and lay the basis for functional duplication in their repair and replacement. Also, the preliminary results highlight the need to incorporate the structural differences into finite-element simulations as otherwise, simulations of ATAA tissues might not be good predictors for the actual in a Vivo stress state.

5.1. Materials and Methods

In order to yield high-quality measurement results, it is necessary to define a strict approach for the specimen's origin and the measurement data acquisition. In addition, also a defined setup and a well-structured test protocol are required. This chapter describes exactly the steps from the origin of the samples, transport and transport conditions, the storage of the

tissue, preparation and processing and the data analysis. To stay on top of things, the steps from the specimen‘s origin up to the data analysis, are documented chronologically in the following sections.

5.1.1. Ascending aorta aneurysm microstructure

5.1.1.1. Sample Preparation

Aortic samples were cut open along the longitudinal direction and small samples, approximately 7 x 11 mm in size, were acquired from aneurysmatic specimens, with the longer side marking the longitudinal direction. Subsequently, the samples were cleared using a protocol according to [134]. First, the specimens were dehydrated by submerging them into a graded ethanol series, consisting of 50, 70, 95 and twice 100% concentrated ethanol solutions. Subsequently, the specimens were stored in 100% benzyl alcohol–benzyl benzoate (BABB) for at least 12 h after initially submerging them into a 1:2 solution of ethanol: BABB for 4 h. All steps were performed at room temperature.

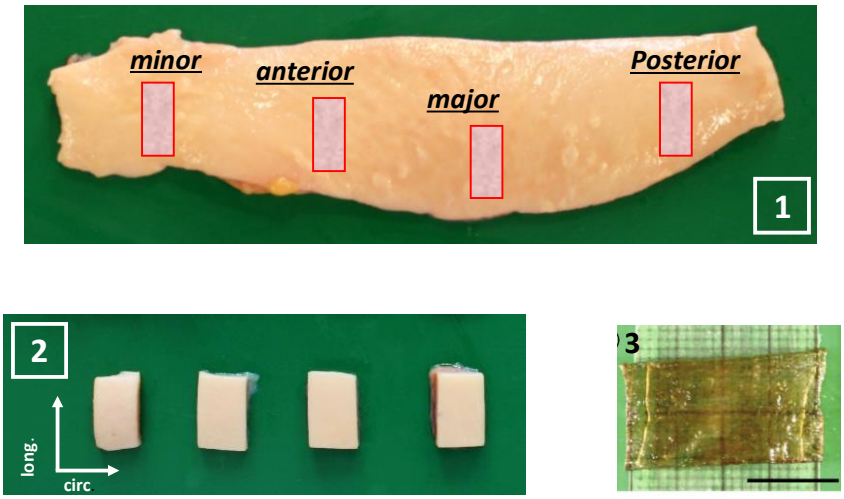

Figure 34 – Steps of preparing ATAA tissue for MTP: (1) Cutting of sample along longitudinal direction; (3) separation of minor, anterior, major and posterior curvature for MTP, (3) sample after dehydration and optical clearing.

5.1.1.2. Second Harmonic generation imaging

To identify the three-dimensional collagen structure of the samples, SHG imaging was performed at the Institute of Science and Technology in Austria. An imaging set-up consisting of a picoseconds laser source and an optical parametric oscillator (OPO; pics emerald; APE, Germany; HighQ Laser, Austria) integrated into a Leica SP5 confocal microscope (Leica Microsystems, Inc., Austria). The excitation wavelength was tuned to 880 nm and the detection of the backscattered signal was achieved using a gallium arsenide- phosphide detector and a BP 460/50 emission filter. Image acquisition was performed using a Leica HCX IRAPO L 25x0.95 water objective with a working distance of 1.5 mm for deep tissue imaging; z-stacks (three-dimensional image stacks) of the cleared aorta specimens were acquired using 0.62 x 0.62 x 1 mm sampling (x–y–z).

5.1.1.3. Microstructural analysis of collagen fibre orientation

Morphological collagen data were extracted from three-dimensional images (z-stack) by combining Fourier power spectrum analysis and wedge filtering, as described in [134 - 135]. The analysis yielded discrete angular distributions of relative amplitudes, which resembled the fibre orientations. To describe a general fibre direction, a coordinate system characterized by the unit rectangular Cartesian basis vectors $\mathbf{e}_1$, $\mathbf{e}_2$ and $\mathbf{e}_3$, as shown in Figure 35, was used [136], with the unit vector $\mathbf{N}$ representing a general fibre direction in the (unloaded) reference configuration, defined by the two angles $\Phi[\ [0,2\ \pi]$ and $\Theta[-\pi/2,\ \pi/2]$. For a circular cylinder, $\mathbf{e}_1$ is taken to be the circumferential direction and $\mathbf{e}_3$ the longitudinal direction, and therefore we refer to the angles Φ and Θ as the in-plane and out-of-plane angle, respectively. The in-plane and out-of-plane collagen fibre orientations were fitted using a bivariate von Mises distribution $\rho(\theta,\Phi) = \rho_{ip}(\Phi)\rho_{op}(\Theta)$ for the probability density ρ of $\mathbf{N}$

(in-plane and out-of-plane dispersions are essentially independent [137]), with the particular choice [136].

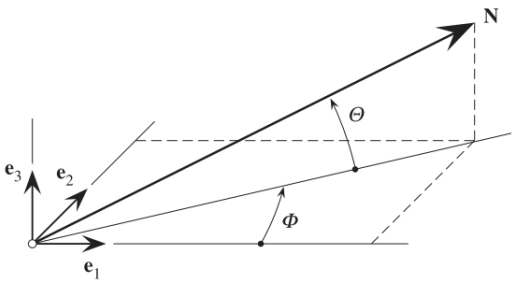

*Figure 35 – Unit vector **N** representing a general fibre direction defined by the two angles θ and Φ with respect to rectangular Cartesian unit basis vectors $\boldsymbol{e}_1$, $\boldsymbol{e}_2$, $\boldsymbol{e}_3$* [136].

$$\rho_{ip}(\Phi) = \frac{exp\lfloor a \cos 2(\Phi \pm \alpha)\rfloor}{I_0(a)} \qquad \textit{Equation 69}$$

$$\rho_{op}(\theta) = 2\sqrt{\frac{2b}{\pi}}\frac{exp\lfloor b \cos(2\theta - 1)\rfloor}{\mathrm{erf}(\sqrt{2b})} \qquad \textit{Equation 70}$$

where $\rho_{ip}(\Phi) = \rho_{ip}(\Phi + \theta)$ and $\rho_{op}(\theta) = \rho_{op}(-\theta)$ describe the in-plane and out-of-plane dispersions, respectively. In Equation 69Equation 70, a and b are (constant) concentration parameters, i.e. fitting parameters, which define the shape of the von Mises distributions, $I_0(a)$ is the modified Bessel function of the first kind of order 0 and α is the angle between the mean fibre direction and the circumferential direction e_1.

According to [136], we introduce the two scalar quantities κ_{ip} and κ_{op} which measure the in-plane and out-of-plane dispersion, respectively.

$$\kappa_{ip} = \frac{1}{2} - \frac{I_1(a)}{2I_0(a)} \qquad \textit{Equation 71}$$

$$\kappa_{op} = \frac{1}{2} - \frac{1}{8b} + \frac{1}{4}\sqrt{\frac{2}{\pi b}}\frac{\exp(-2b)}{\mathrm{erf}(\sqrt{2b})} \qquad \textit{Equation 72}$$

where $0 \leq \kappa_{ip} \geq 1$ and $0 \leq \kappa_{ip} \geq 1/2$. If both concentration parameters a and b become infinite the collagen fibres are perfectly aligned. Layer-specific thicknesses were measured from out-of-plane images using FIJI [138].

5.1.2. Ascending aorta aneurysm mechanics

5.1.2.1. Sample preparation

Aortic tissue samples were obtained from patients who underwent repair of the aneurysmal ascending aorta at IRCCS ISMETT, as part of their clinical care and not for the study. Indication for aortic surgery was based on aortic size measurement, predisposing risk factors, bicuspid aortopathy and familiarities. In total, human aortic tissue from 10 subjects with age (74.4 ± 6.82 yrs, mean ± SD, ranging from 67 to 88 yrs, 3 female and 7 male) were tested. Information about the ATAAs patients investigated is summarized in Table 7.

	Age	***Gender***	***D (mm)***
Patient n.	***(years)***		***(mm)***
ATAA-1	80	F	50
ATAA-2	68	F	47
ATAA-3	68	M	43
ATAA-4	78	M	54
ATAA-5	88	M	58
ATAA-6	71	M	49
ATAA-7	67	M	54
ATAA-8	78	F	55
ATAA-9	79	M	56
ATAA-10	67	M	54

Table 7 – Patient information of all tested ATAA specimens: age, gender (F, female; M, male), maximum diameter D[mm].

Immediately after excision, the ATAAs were frozen and stored at −80°C. Before mechanical testing, the frozen samples were slowly thawed at 4°C and then prepared at room temperature (20 °C). All tests were conducted for one sample within 24 hours after defrosting and all samples were tested within 14 days after excision. The cryopreservation was applied to neglect the influence of the muscular response on mechanical behaviour, hence the behaviour of the arterial wall is governed mainly by elastin and collagen components [108].

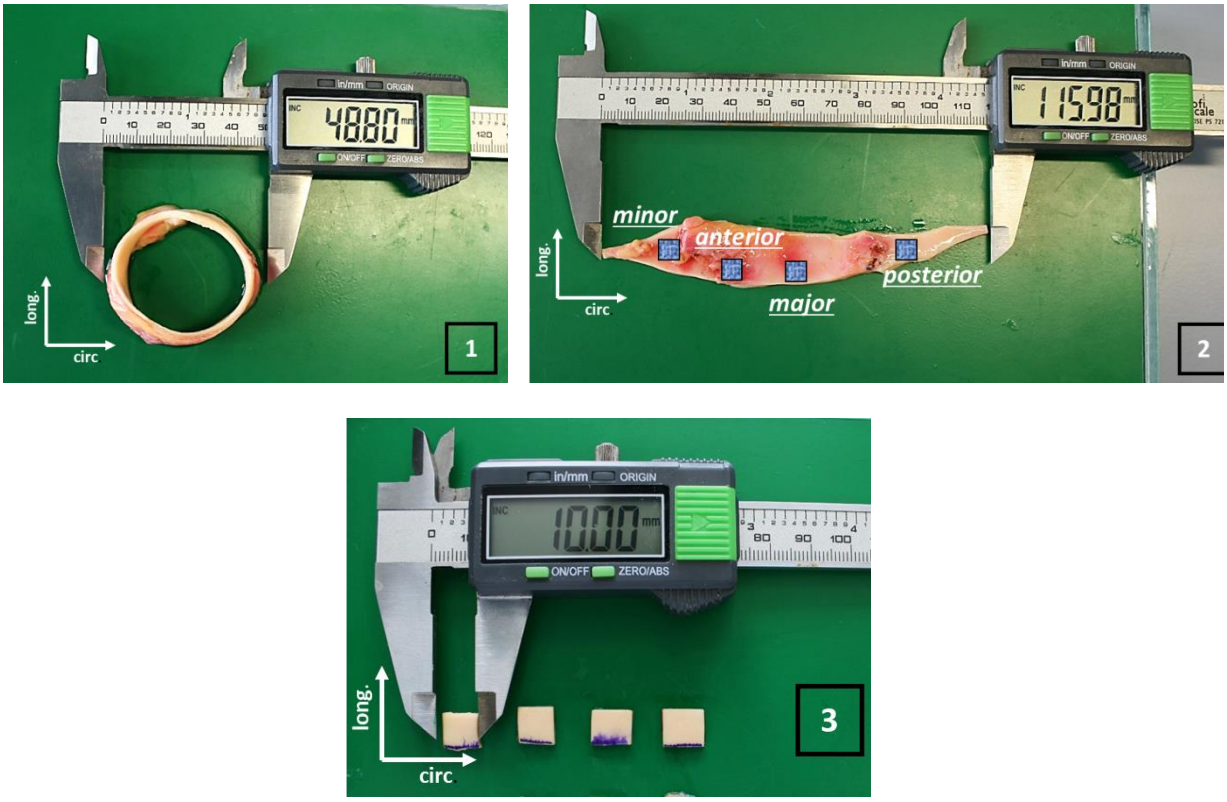

Figure 36 – Steps of preparing ATAA tissue for layer-specific biaxial testing: (1) Ring of intact aortic wall; (2) Cutting of sample along longitudinal direction; (3) separation of minor, anterior, major and posterior curvature for biaxial tests.

Loose connective tissue was carefully removed from the whole aortic surface. The average thickness of these strips was measured by means of a video extensometer to compare it with the photometrical method. For a detailed description of the video extensometer thickness measurement method (VTMM), see [19]. With the video-extensometer, It was obtained the total wall thickness. Along the longitudinal direction of ascending aorta, the harvested tissue ring was cut into squared specimens from each quadrant as a following: (a) anterior, (b) posterior, (c) major curvature and (d) minor curvature of the aorta with dimensions of 12 x 12 mm (Figure 36). Subsequently, black tissue markers were applied by spraying on the surface of each sample generating a scattered pattern suitable for optical tracking. A solid line blue was used to mark the circumferential direction.

5.1.2.2. Biaxial Tensile test

A stretch-driven protocol was used for testing, and executed with a stepwise increase of 0.05 stretch until rupture, starting with 5% deformation. Each sample was tested using the following protocol for each stretch increment: $\lambda_{long}:\lambda_{circ} = 1:1, 1:0.75, 0.75:1, 1:0.5, 0.5:1$, where λ_{long} denotes the stretch in the longitudinal direction while λ_{circ} is the stretch in the circumferential direction. After each increase in stretch four preconditioning cycles were conducted and the fifth was then used for data recording and analysis. Throughout the test, the samples were loaded quasi-statically at a rate of 2 mm min^{-1}. It is worth noting that the used biaxial testing protocol covers a large range of deformations including the in vivo situation, and hence provides data for a unique set of material parameters. As the results, especially for the adventitial samples, were very sensitive to initial preloads, zero strain was defined at a tissue configuration under 0.005 N load.

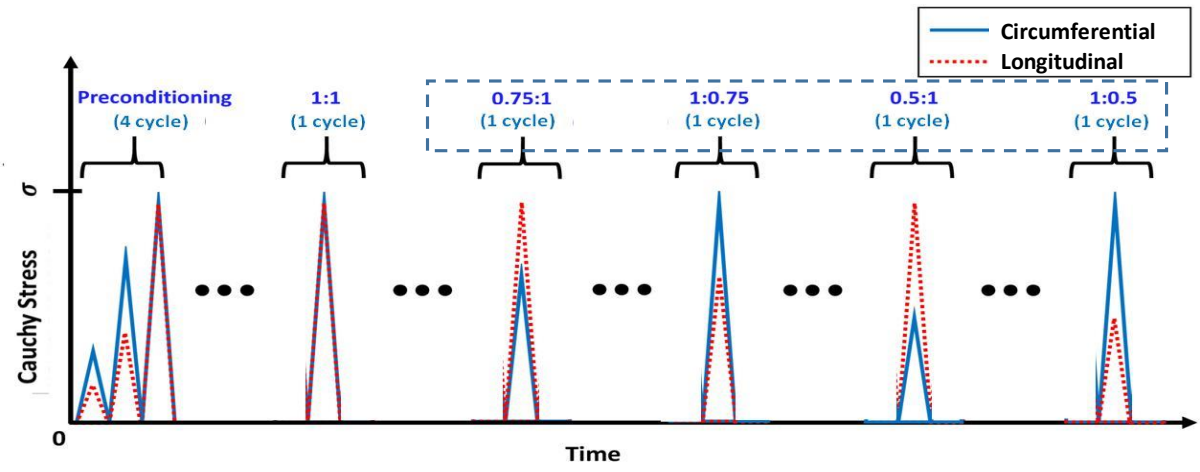

Figure 37 — Schematic of different loadings according to the loading protocols.

5.1.2.2.1. Biaxial testing device and test equipment

Biaxial tensile tests are done with a measurement device developed by the Institute of Biomechanics from the Technical University of Graz in cooperation with the Messphysik Company (a division of Zwick and Roell). The developed testing device is based on the principle of the testing system developed by Yin et al. (1987) [139]. In general, the machine consists of n.4 main parts: four independently controlled traverses with independent loading cells for each traverse, a vessel system including a heating circuit, the optical detection system consisting of a video extensometer and the computer-based measurement data acquisition. A schematic of the system developed by Yin et al. (1987) [139] is shown in Figure 38. The new biaxial testing device used for biaxial tensile tests was specially designed for mechanical testing of natural and artificial elastic tissues. The four high-resolution linear actuators can be controlled independently by position, force or elongation (stress) using a stretch controlled testing algorithm. The position control is handled by an individual computing and control unit for each traverse.

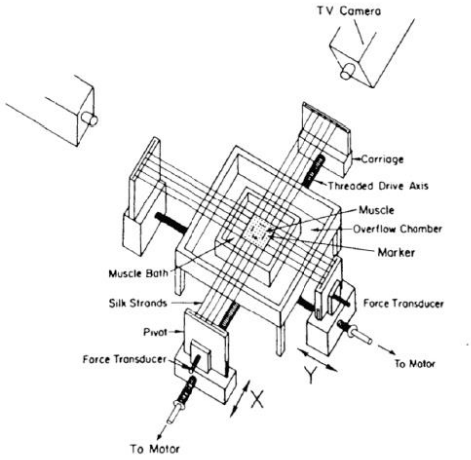

Figure 38 — Schematic of the biaxial testing device from Yin et al. (1987) including an optical detection system, bath for the testing solution and the motor controlled carriage system. The specimen is placed in the middle of the bath and connected with each slide using silk cords.

5.1.2.2.2. Principle of measuring with the biaxial testing device

The specimen is equipped with four markers before fitted into the testing device. After the fitting, the video extensometer gets calibrated according to the location of the specimens and the positions of the markers on the specimen. After the calibration of video detection, the zero position is getting defined. The zero position defines the distance between the markers at a not loaded state of the specimen and the starting position for each of the four sledges. During the measurement cycle, the video extensometer detects the position of the markers located on the specimen and compares the position with the different force information from the loading cells of the four traverses.

The Doli software is calculating the position data for the control unit of each linear actuator using a stretch controlled protocol. This stretch controlled protocol makes it possible to define the parameters for the traverse speed in a form that the stretch ratios for each axis (x-axis and y-axis) are kept at a constant defined level. A principle of the biaxial measurement device is shown in Figure 39.

A measuring cycle consists of two different parts: a loading curve, and a strain relief. The advantage of this measuring method is the real-time acquisition of all relevant data, which is necessary for a high-quality measurement result. The data is stored in form of an excel-sheet, including the forces collected from the loading cell of each traverse (F1, F2, F3, F4), the position of the four traverses (according to the defined zero-position), the distance of the markers at zero-position and the sampling time for each data point.

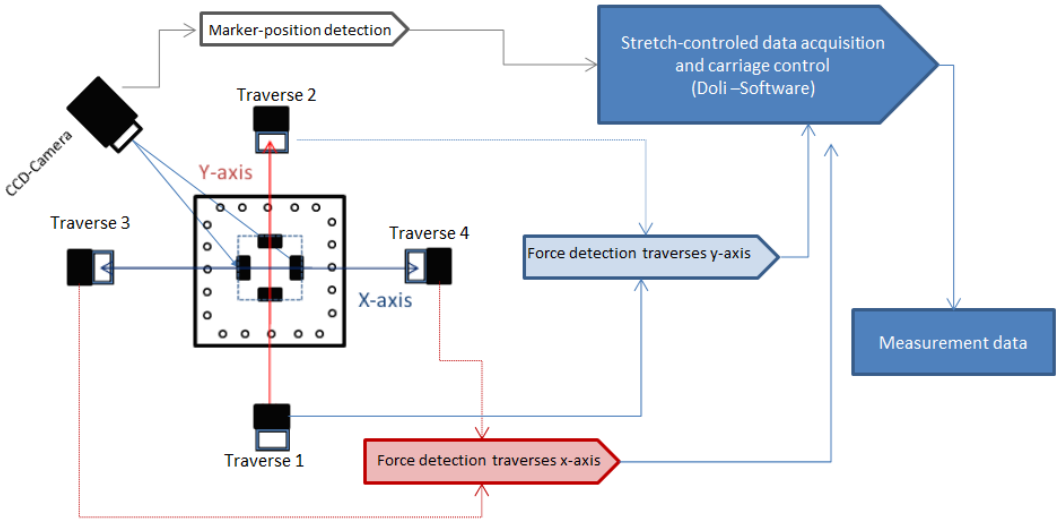

Figure 39 — Principle of the data acquisition and data collection according to the biaxial testing device developed by the Institute of Biomechanics and the Messphysik Company

5.1.2.2.3. Carriage devise, hooks and cords

Depending on the softness of the tested aortic tissue, the carriage device, the hooks and cords play a major role. According to the slight deformation and ductility of aortic tissue, residual stresses and elasticity of the cords are highly undesirable and would occur a falsification of the test resulting data. Another problem is the traverse “nonlinear” forces according to the form of the carriage device depending on the attachment of the cords onto the provided bolts of the carriage devices. As demonstrated in Figure 40 the cords provide forces along the traverse axis because of their assembly on the carriage.

These traverse forces prevent a linear force distribution on the specimen during the tensile testing. To countervail these shear forces, new carriage devices were developed, to get more linear tensile forces. As shown in Figure 41, the traverse forces in contrast to the standard carriage devices shown in Figure 40 are much smaller. Another problem during the biaxial tensile tests is the loosening of the cords from the anchorage. With the new anchorage, the cords are fixed with the bolt to prevent this.

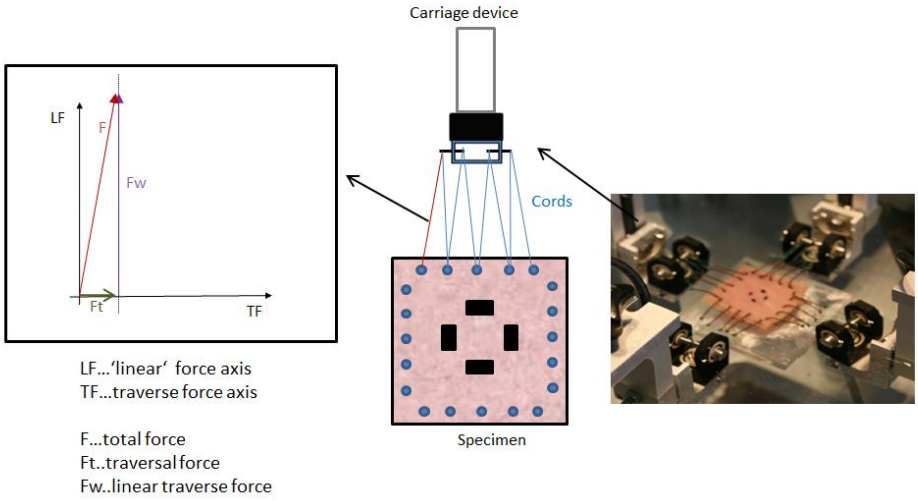

Figure 40 – Non-linear stress force on the cords according to the carriage device depending on the attachment of the cords. The diagram shows the undesirable traverse force Ft, which occurs as a non-homogeneous force-displacement on the specimen

The cords which fasten the specimen to the carriages should not be stretchable. A stretchable cord would hardly falsify the results of the tensile tests because the expansion of the cords would be included in the measured data. Therefore a surgery cord was used. A surgery cord has the advantage, that it provides an even good stress behaviour during the tensile tests with nearly being unstretchable.

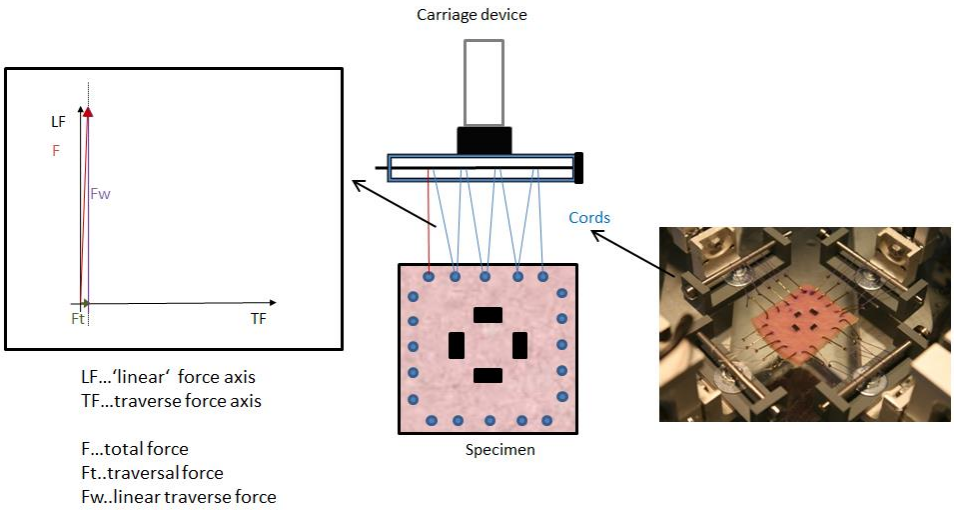

Figure 41 – New developed carriage device with almost 'linear' forces. The new attachment system also provides the detach of the cords during the measurement cycles.

Figure 42 – Picture of the surgery cords and fishing hooks used for fitting the specimen into the biaxial testing device

The hooks used were commercially used fishhooks, which were strung on the cords for the fitting of the specimen into the biaxial measuring device. A picture of the surgical cord and the hooks for the testing setup is shown in Figure 42.

5.1.2.2.4. Overview of the solutions used for the biaxial tensile tests

According to the biaxial tensile test and the highly specific behaviour of the tissue at a non-body milieu, the use of specific solutions is recommended. The main target is to seek a nearly similar milieu as given in the body of the donor with consideration to the inactivated state of the aortic tissue. To ensure that, during this experimental part different solutions were used, to get a realistic measurement data as possible.

PBS solution

The PBS solution (Phosphate buffered saline) is a buffer solution which is used during biological research. The solution offers a similar Ph-value (7.2 PH) as the one in the human body's milieu. This solution is a water-based salt solution containing potassium chloride and potassium phosphate and sodium chloride. This solution is isotonic and non-toxic to cells. A list of all components included in the PBS solution is shown in Table 8. Potassium chloride is an essential salt in the body's cell life-circle. Due to its antiseptic property, it is capable of fighting germs. It can even prevent the decay of body tissue. Potassium phosphate and sodium phosphate are essential salts that are used for human body ph-value regulation and play several roles as an addition in the ATP cycle and as components in several cell membranes.

Component	**Formula weight** $[g * mol^{-1}]$	**Amount** $[g]$	**Weight** $[g]$
Sodium phosphate (NaH2PO4 * 2H2O)	178.01	1.44	
Potassium phosphate (KH2PO4)	136.09	0.24	
Potassium chloride (KCL)	74.55	0.2	
dissolve in distilled water			1000

Table 8 — Recipe of PBS solution used for solution bath

PBS is a very good buffer solution for tests at a defined ph-value. For the tests, the solution was heated to body temperature at 37°C.

5.1.2.2.5. Setup and mounting the specimen into the biaxial testing device

To allow clamping of the aortic tissue to the testing device for the biaxial tensile tests, the carrier cords are attached to the specimen. One carrier cord consists of a surgery cord where

four hooks are strung on it (used cords and hooks are shown in Figure 42). For high-quality measurement results, this step must be done very carefully, because influences like false pretension of the specimen between the four carrier devices or false hook position falsify the received data strongly.

5.1.2.2.6. Attaching the hooks to the specimen

The positioning of the hooks on the specimen plays a major role. The implementation of the hooks into the specimen must be carefully set according to the marked positions from the template, to achieve a nearly homogeneous distribution of the tensile forces during the biaxial tensile tests Yin et al. (1987) [139]. Picture 1 of Figure 43 shows the solaced hooks onto the specimen from human aortic tissue of one patient. Because of the softness of the aortic tissue, the attachment of the hooks to the specimen onto the marked positions is not exactly possible as seen in picture one of Figure 43.

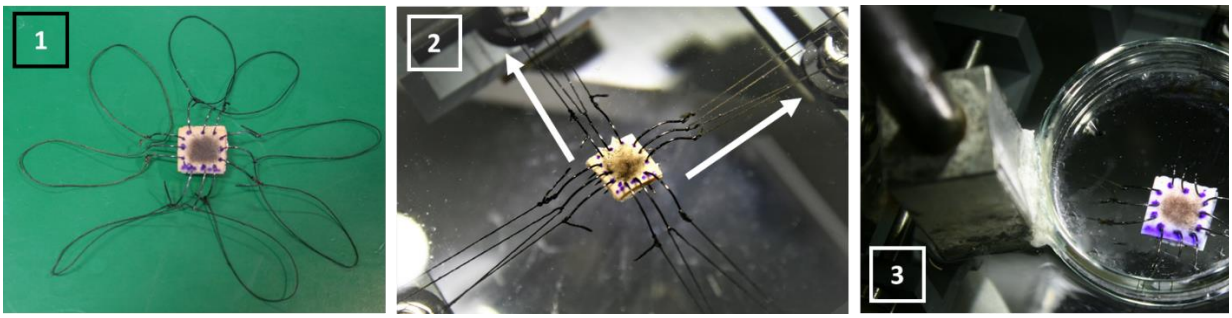

Figure 43 – Cutting sequence for the specimen out of the pathological tissue of ATAA.

5.1.2.2.7. Marker and marker position

A black powder is used as a material for markers (see picture 1 of Figure 43). This material was chosen because of its good contrast according to the optical detection by the CCD-camera. The area of marker dimension should be about 5 mm x 5 mm (length x width). The

region between the markers represents the homogeneous area to which the measured data from the tensile tests are referred.

5.1.2.2.8. Inserting the specimen into the testing device and calibration of the optical measuring system for the marker detection

The inserting of the specimen into the biaxial testing device requires a lot of experience. During the fixing of the specimen using the carrier cords between the carriage devices, the tissue may not be injured by excessive stretching forces. Excessive stretching of the tissue would damage the tissue before the biaxial tensile tests and would render the tissue as useless. It is also important to place the specimen exactly central between the carriage devices to provide linear traction forces during the tensile tests. The selection of the proper preload of the cords stretch is also very essential for defining a non-loaded state for the specimen at zero position for biaxial tensile testing setup as shown in picture two of Figure 43.

Since the optical marker detection is very sensitive to surface contamination of the solution bath, a transparent plexiglass lens was used to avoid them. Because of the dissolve of the fat deposits in the human aortic tissue due to the temperature of the solution bath, there was fat floating on the solution baths surface and caused a loss of the markers. The plexiglass lens has a circular form that is dipped into the solution bath to prevent artefacts according to the reflection of solution surface contamination, which can be responsible for a loss of the marker by the video detection system during the tensile tests. The setup for the lens above the specimen is shown in picture three of Figure 43. After defining the zero position for the specimen and the glass, the video extensometer system gets calibrated, using a film with defined marked intervals placed on the surface of the specimen.

5.1.2.3. Data acquisition, data analysis and mathematical background

Actuator control and data acquisition are achieved by using the software Test Motion Version 2:0 by 2.4 Section 2 41 'Doli' Elektronik Gmbh, Munich, Germany. For the non-contacting strain-measurements the software Laser Speckle Extensometer Version 2:23:3:0 by MESSPHYSIK Materials Testing, Fuerstenfeld, Austria was used. The analysis of data obtained from the biaxial tensile tests is realized by the use of a custom-written Matlab application for the used stretch protocol. The application includes computation, smoothing algorithm and a plotting option for calculated data. The assessment of the data occurs, using plots, showing the calculated Cauchy-stress σ depending on the measured stretch λ for each specimen during the biaxial tensile tests under different loading conditions.

5.1.2.4. Data analysis and smoothing

Biological tissue, like the aortic, shows a non-linear stress behaviour and is assumed to be incompressible, anisotropic and viscoelastic. Non-linear stress behaviour means that the stiffness of the aortic tissue is increasing due to the increasing stress exerted on the tissue. Due to the assumption of incompressibility, the volume of aortic tissue, according to the stress-strain relation is constant.

5.1.2.4.1. Stretch-controlled protocol

While using a stretch-controlled measurement protocol, the regulating values are the stretch ratios of the different axis (fibre axis and cross-fibre axis), where the stretch ratio for x-direction is written as λ_x and in the y-direction as λ_y. The stretch ratios are calculated as shown in Equation 73 from the collected measuring data.

$$\lambda_x = \frac{x_{x^*}}{X_x} \qquad \lambda_y = \frac{x_{y^*}}{X_y}$$ *Equation 73*

Here X_x and X_y are the defined marker distances for each direction (X_x in cross-fibre direction and X_y in fibre direction) which include the homogeneous area and x_{x^*} and x_{y^*} are the measured distance changes between the markers on the specimen according to the stretch acting on the specimen for each direction. For each protocol as described in 5.1.2.2, the stretch ratios λ_x and λ_y are held constant depending on the ratio.

5.1.2.4.2. Cauchy-stress calculation

In order to quantify the mechanical behaviour of aortic tissue, the Cauchy-stress ('true stress') is used as a significant value. The Cauchy-stress σ can be calculated for each direction by the formula shown in Equation 74 where t is the mean thickness of the tissue in the current configuration and x_x and y_y indicates the current dimensions of the specimen for the x-direction and y-direction of the specimen according to the traverse position independence of the defined zero-position of the biaxial testing device.

$$\sigma_{xx} = \frac{f_x}{t * x_y} \qquad \sigma_{yy} = \frac{f_y}{t * x_x}$$ *Equation 74*

Because of the assumed incompressibility of the aortic tissue, the volume during deformation is constant. For this incompressible state of the aortic tissue the values from the undeformed configuration t,x_x y_y and the deformed configuration T, X_x, X_y can be written as shown in Equation 75.

$$t * x_x * x_y = T * X_x * X_y$$ *Equation 75*

$$\sigma_{xx} = \frac{f_x * \lambda_x}{T * X_x} \qquad \sigma_{yy} = \frac{f_y * \lambda_y}{T * X_x}$$ *Equation 76*

The tissue stretches are defined as λ_x for x-direction and λ_x for y-direction, shown in Equation 73, whereas the Cauchy stress can be rewritten from Equation 74, Equation 75 and Equation 73 to Equation 76. The optical marker detection system and the loading cells of each traverse provide the relevant data for the Cauchy-stress calculation.

5.1.2.4.3. Material Model

We introduce the deformation gradient $\mathbf{F}$, the right Cauchy– Green tensor $\mathbf{C} = \mathbf{F}^T\mathbf{F}$, and two symmetric fibre families with the (in-plane) mean fibre directions, i.e.

$$\boldsymbol{M}_4 = \cos\alpha\boldsymbol{e_1} + \sin\alpha\boldsymbol{e_2} \qquad \boldsymbol{M}_6 = \cos\alpha\boldsymbol{e_1} - \sin\alpha\boldsymbol{e_2}$$ *Equation 77*

where the mean fibre directions M_4 and M_6 make an angle α with the circumferential direction $\mathbf{e_1}$. In addition, we introduce the invariants I_1, I_4, I_6 and I_n according to:

$$\boldsymbol{I}_1 = tr\boldsymbol{C} \quad \boldsymbol{I}_i = \boldsymbol{C}:\boldsymbol{M_i} \otimes \boldsymbol{M_i} \quad i = 4{,}6 \qquad \boldsymbol{I}_n = \boldsymbol{C}:\boldsymbol{M_n} \otimes \boldsymbol{M_n}$$ *Equation 78*

where $\mathbf{M_n}$ is a unit out-of-plane vector (Figure 44). To mathematically quantify the fibre dispersion, we use the generalized structure tensors $\mathbf{H_4}$ and $\mathbf{H_6}$, which describe the material behaviour [136], i.e.

$$\boldsymbol{H}_i = AI + B\boldsymbol{M_i} \otimes \boldsymbol{M_i} + (1 - 3A - B)\boldsymbol{M_n} \otimes \boldsymbol{M_n} \quad i = 4{,}6$$ *Equation 79*

where the constants A and B are:

$$A = 2\kappa_{ip}\kappa_{op} \;\; and \; B = 2\kappa_{op}(1 - 2\kappa_{ip})$$ *Equation 80*

Assuming that the aorta can be modelled as a purely elastic, incompressible and fibre-reinforced material, the structure tensors $\mathrm{H_i}$ are incorporated into the decoupled strain-energy function $\boldsymbol{\Psi}$ according to:

$$\psi = \psi_g(\boldsymbol{C}) + \sum_{i=4,6} \psi_{fi}(\boldsymbol{C}, \mathbf{H_i})$$ *Equation 81*

The strain-energy function ψ_g represents the ground matrix, i.e.:

$$\psi_g(\boldsymbol{C}) = \frac{c}{2}(I_1 - 3)$$ *Equation 82*

where $\mathrm{c}>0$ is a stress-like material parameter and ψ_{fi} represents the contribution of the two fibre families, i.e.

$$\psi_{fi}(\boldsymbol{C}, \mathbf{H_i}) = \frac{k_1}{2k_2} \sum_{i=4,6} \{\exp[\, k_2(I_i^* - 1)^2] - 1\} \;\; i = 4{,}6$$ *Equation 83*

with $\mathrm{k_1}>0$ is a stress-like material parameter and $\mathrm{k_2}>0$ is a dimensionless parameter and the generalized invariants I_i^* according to:

$$I_i^* = tr(\mathbf{H_i}\boldsymbol{C}) = AI_1 + BI_i + (1 - 3A - B)I_n \quad i = 4{,}6$$ *Equation 84*

which includes the mean fibre directions $\mathbf{M_i}$ in the form of the invariants $\mathrm{I_i}$ and the two dispersion parameters κ_{ip} and κ_{op}, which will be better described later, in the form of the constants A and B. The material model uses three structural parameters (κ_{ip}, κ_{op}, α) which can be determined by structural analysis (in this study using SHG images) and three material

parameters (c, k_1, k_2), which are determined by fitting the model to the mechanical data (in this study to the data obtained from biaxial stretching tests).

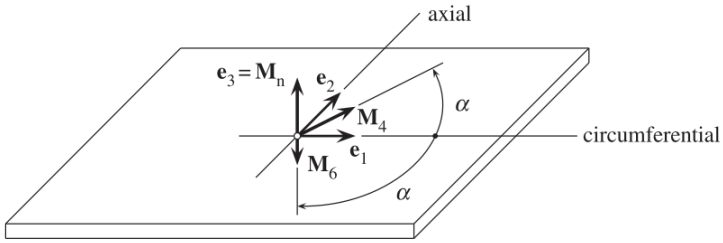

Figure 44 – Sample with two symmetric fibre families with mean fibre directions $\boldsymbol{M_4}$ *and* $\boldsymbol{M_6}$*, each making an angle a with the circumferential direction* $\boldsymbol{e_1}$*. The normal direction of the plane is* $\boldsymbol{M_n}$ [136].

5.1.2.4.4. Data analysis with Matlab

The data calculation is done with an individually designed program, including fitting algorithm, offset correction and plotting option. It offers the possibility to overlay multiple curves simultaneously or to plot a single curve for data analysis. The main problem getting meaningful data for plotting are the artefacts from the loading cells since the loads are in the very lower measuring range. This noise falsifies the measured data achieved from the loading cells, and cause very noisy plots. Especially during the biaxial tensile test of the human aortic tissue, which consistence is very soft, the magnitudes of the residual stresses of the cords are relatively high in comparison to the calculated stress-strain components. Therefore a variable smoothing filter was implemented. Figure 45 shows a screenshot of the GUI (Graphical User Interface) for data analysis.

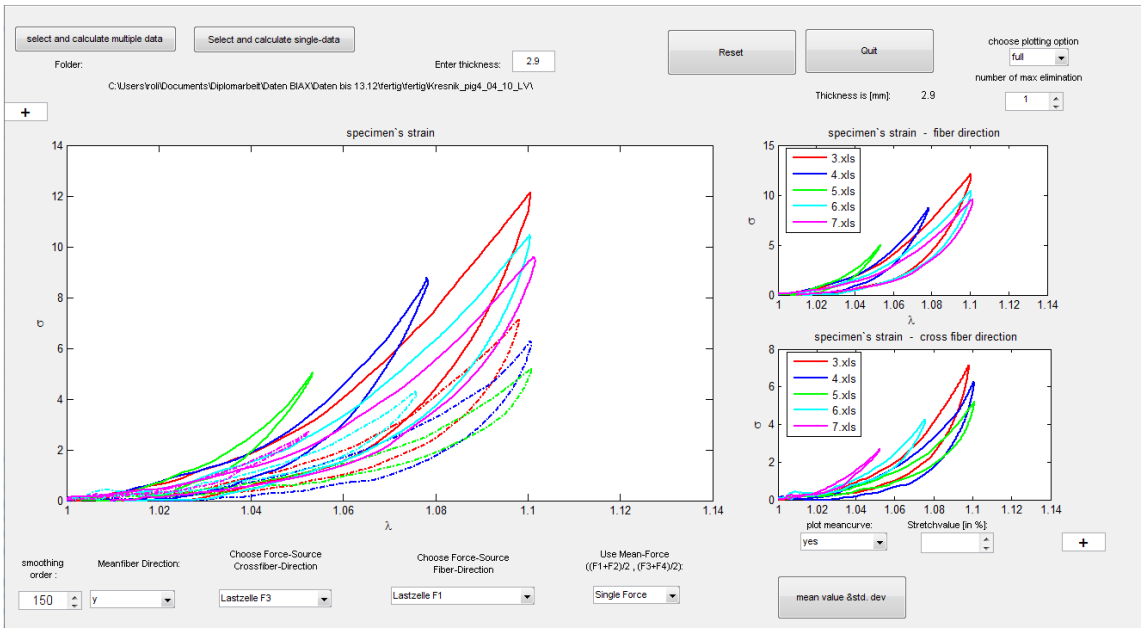

Figure 45 – GUI (Graphical User Interface) created in Matlab 2009a for data analysis received from the biaxial testing system. MFD (Mean-fiber direction) and CFD (Cross-fiber direction) are plotted separately in the left two plots and an overlapping plot of both for analyzing the mechanical behaviour in the centre of the GUI.

After the structural parameters have been determined as 5.1.1.3, fitting of the material model to the biaxial experimental data was performed. Data from all five testing protocols (1:1, 1:0.75, 0.75:1, 1:0.5, 0.5:1) in both longitudinal and circumferential directions were fitted simultaneously, using the optimization toolbox lsqnonlin in Matlab (The MathWorks, Inc., MA, USA). As the structural parameters (κ_{ip}, κ_{op} , α) were known from structural analysis, and hence kept constant throughout the fitting procedure, the only three fitting parameters were ($\mathbf{c}, \mathbf{k}_1, \mathbf{k}_2$). It minimized the objective function:

$$e = \sum_{\substack{d=1:1,\\ 1:0.75\\ \dots}} \sum_{i=1}^{n} \left[\left(\sigma_{11,i}^{mod,d} - \sigma_{11,i}^{exp,d}\right) - \left(\sigma_{22,i}^{mod,d} - \sigma_{22,i}^{exp,d}\right)^2 \right] \qquad \textit{Equation 85}$$

where n is the number of considered data points, and $\mathbf{d}$ is the data set, e.g., different ratios of a biaxial tension test, and:

$$\sigma_{11,i}^{mod} = (\lambda_{11}\frac{\partial\Psi}{\partial\lambda_{11}}) \qquad \sigma_{22,i}^{mod} = (\lambda_{22}\frac{\partial\Psi}{\partial\lambda_{22}})$$ *Equation 86*

are the Cauchy stresses in the circumferential and longitudinal directions of the aortic tissues predicted by the function Ψ for the i–th data record. The associated experimental Cauchy stresses, σ_{11} and σ_{22}, are calculated directly from the original data (Equation 76). As a measure for the 'goodness of fit, It calculated the coefficient of determination R^2:

$$R^2 = 1 - \frac{SS_{err}}{SS_{tot}}$$ *Equation 87*

where SS_{err} and SS_{tot} are the sums of squares of the differences between model/experiment and the mean of experiment/experiment.

5.2. Results

5.2.1. Multi-photon imaging and analysis (Structural data)

Figure 46 shows one example of image analysis of multi-photon microscopy of the collagen and elastin fibre network of the aneurysmal aorta. In the red show the signal of elastin in two-photon excitation fluorescence and the channel of collagen in green in the second harmonic generation and on the right the overlap image.

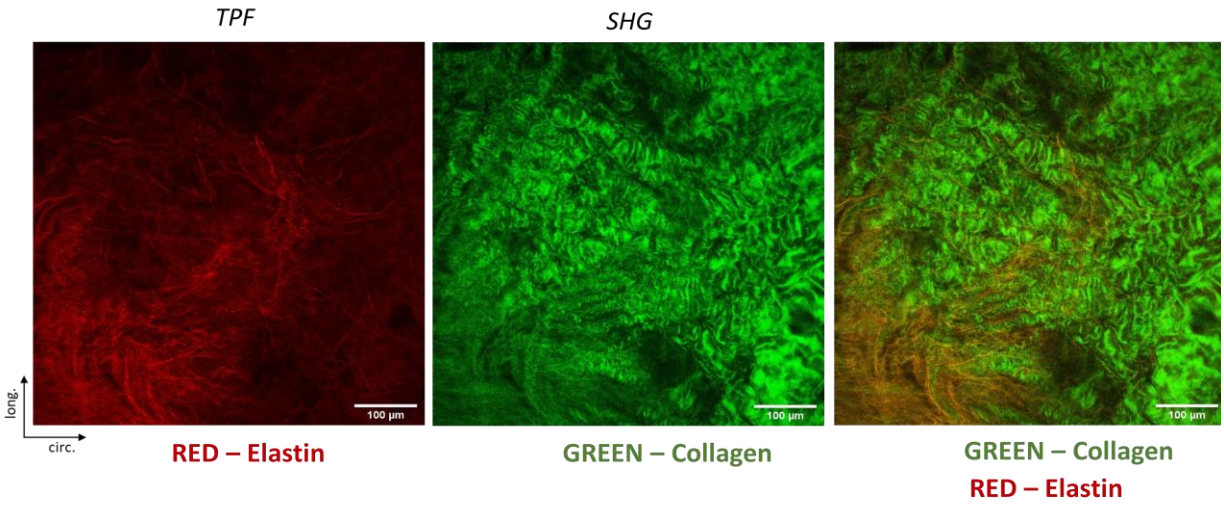

Figure 46 – Example of multi-photon microscopy images (stack of 600 µm) of elastin (red) and collagen (green) fibers in the aneurysmal aorta

Figure 47 shows SHG images of a representative sample; the two images on the top display in-plane sections of the intima (I), media (M) while on the bottom adventitia (A) and image through-the-thickness is displayed. This sample exhibited a strikingly healthy architecture. It showed a rather isotropic intimal side, two fibre families oriented more towards the circumferential direction in the media and show wavy and thicker fibre bundles more oriented towards the axial direction in the adventitia. The image through-the-thickness displays the intima on the right and the highly oriented media and then, the wavy collagen of the adventitia. The intensity plot (Figure 47-b) depicts the collagen fibre orientation and dispersion through the thickness of the aortic wall. A fibre angle 0 denotes the circumferential direction, whereas 90° denotes the longitudinal direction. The dark red depicts the existence of fibre, whereas blue shows no fibres.

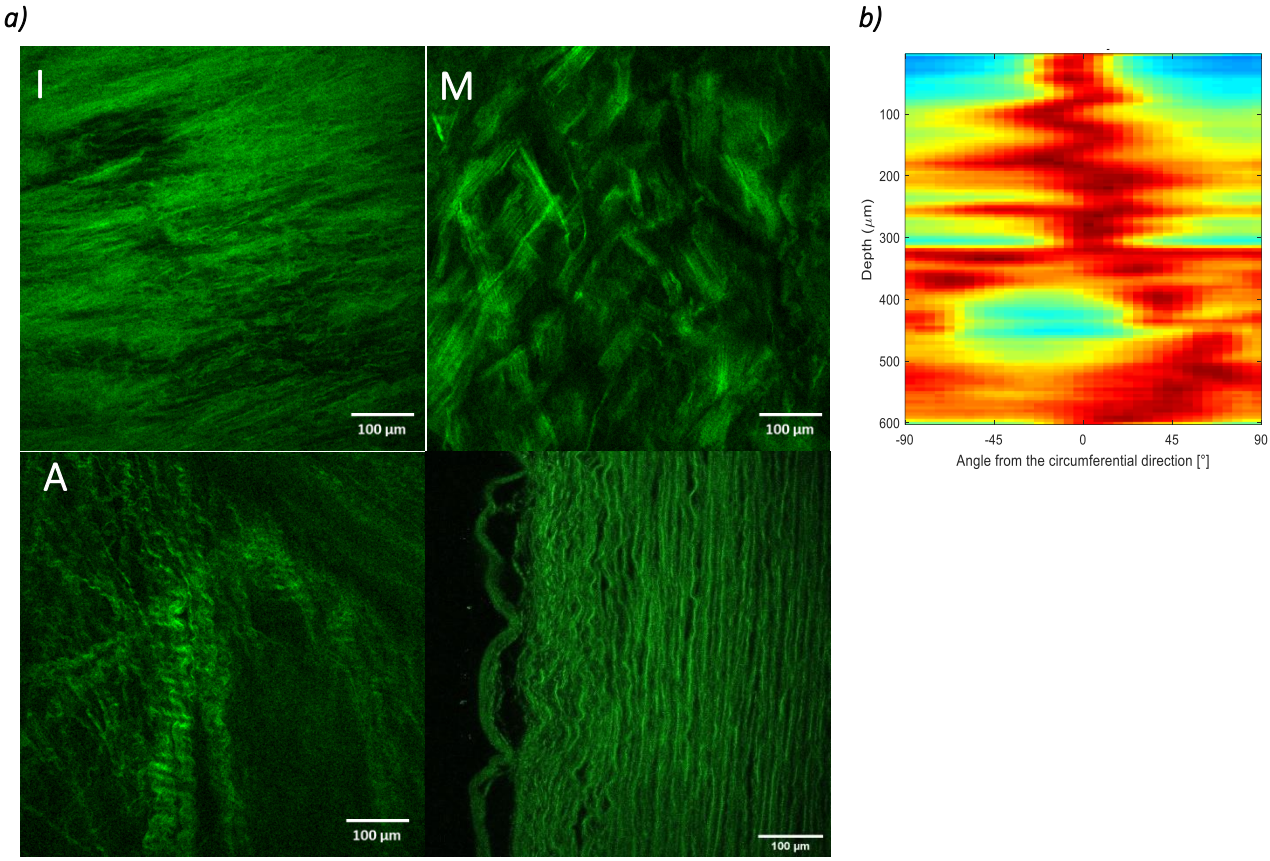

Figure 47 – Layered structure of a representative ATAA-4. (a) Three SHG images showing in-plane sections of the intima (I), media (M) and adventitia (A), while on the bottom an image through-the-thickness is displayed. Scale bar, 100 mm. (b) Intensity plot showing collagen fibre orientation and dispersion through the depth of the aortic wall starting with the intima, followed by the media and the adventitia.

Analyzing other ATAA samples it was not possible to visualize the sample into different layers (intima (I), media (M), adventitia (A)) except for the sample shown in Figure 47.

In general, in the analyzed samples we observed a degenerated structure with calcification and sometimes small fat cells, and thin straight struts of collagen oriented more towards the circumferential direction. Sample ATAA-3, in-plane images of the intima explains the rather isotropic structure seen in the intensity plot at the bottom (Figure 48-a), while the media showed straight collagen fibres oriented in disorder way. In adventitia, the collagen fibres lost their waviness and exhibited rather straight struts of collagen, characteristic of damaged tissue. The intensity plot (Figure 48,a.1) shows fibres preferably orientated towards the circumferential direction throughout the wall, ending with some more anisotropic structure, resembling the degeneration tissue.

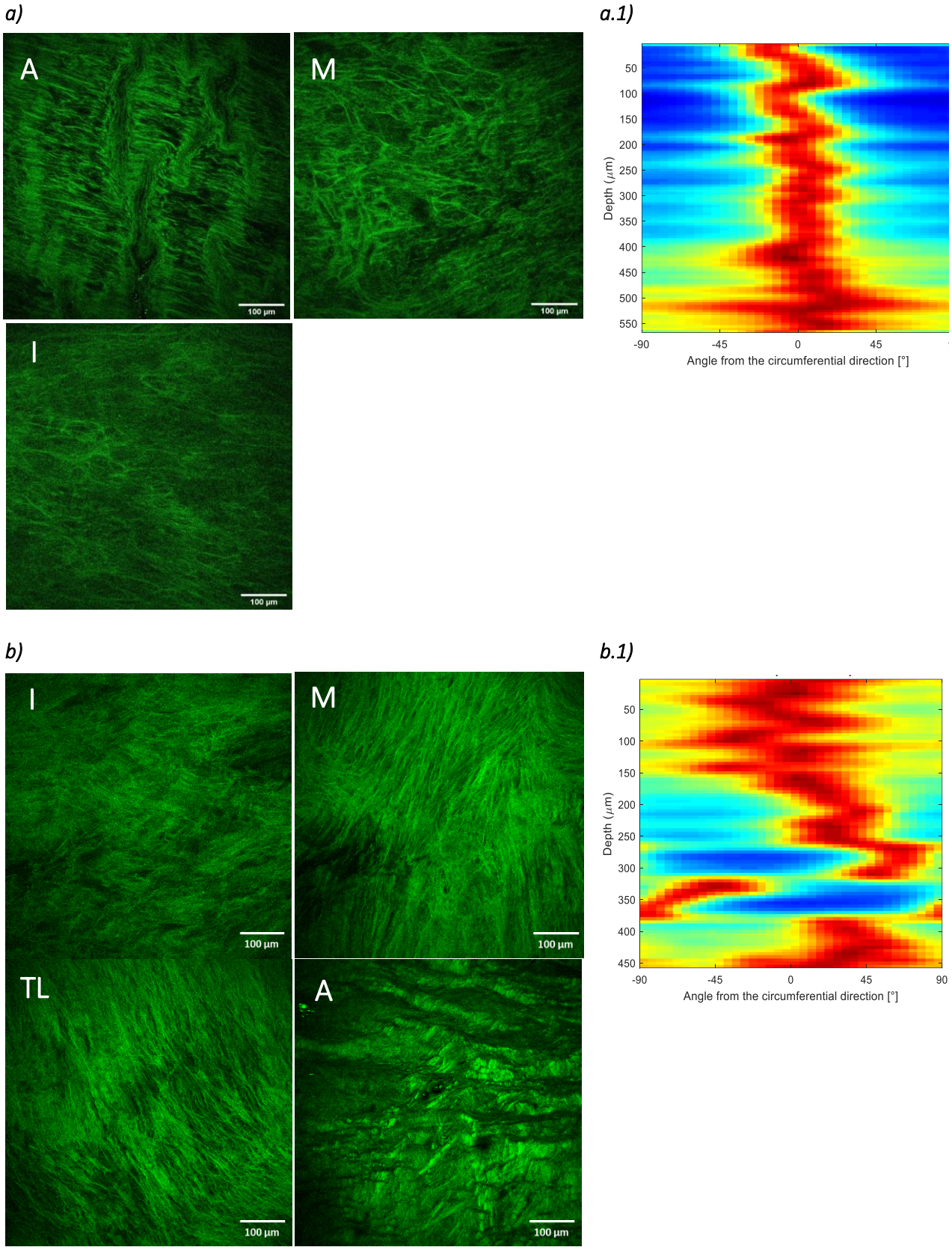

Figure 48 – SHG images and intensity plots for ATAA samples. (a) Layered structure of sample ATAA-3 (minor region) (I, intima; M, media; A, adventitia). a.1) intensity plot for ATAA-3 sample. (b) Sample ATAA-2. Scale bar, 100 mm. b.1) intensity plot for ATAA-2 sample.

Samples ATAA-2 (Figure 48-b), ATAA-1 and ATAA-5 exhibited a similar collagen structure throughout the thickness. Intima layer (I) presents isotropic aspect. Towards the media (M), the fibres became thinner.

It is present a transition layer TL that observed as a (rapid) orientation change of collagen fibres towards two directions and back again in the circumferential direction. The adventitia layer (A) showed thickened collagen struts still wavy but oriented more towards the circumferential direction (Figure 48-b).

Values for the material parameters are reported as the medians and interquartile ranges (the middle fifties), as we cannot assume a normal distribution due to the small sample cohort and outliers can affect the mean and standard deviation severely. (see Table 9).

	Minor			***Anterior***			***Major***			***Posterior***		
	n=5			**n=5**			**n=6**			**n=6**		
	Median	**[Q1 ; Q3]**		**Median**	**[Q1 ; Q3]**		**Median**	**[Q1 ; Q3]**		**Median**	**[Q1 ; Q3]**	
k_{ip}	0.29	0.25	0.32	0.32	0.27	0.34	0.26	0.2	0.3	0.32	0.27	0.35
k_{op}	0.47	0.47	0.49	0.48	0.47	0.49	0.49	0.48	0.49	0.48	0.45	0.48
α (°)	21	21	27	49	40	54	25.5	13.5	45	44	28.5	62.64

Table 9- Structural parameters (kip, kop, a) for the minor, anterior, major and posterior of the ascending aortas determined from SHG images; n indicates the number of samples

For a summary of the dispersion parameters kip, kop and the angle a in the form of box-and-whisker plots, see Figure 49 (a-c).

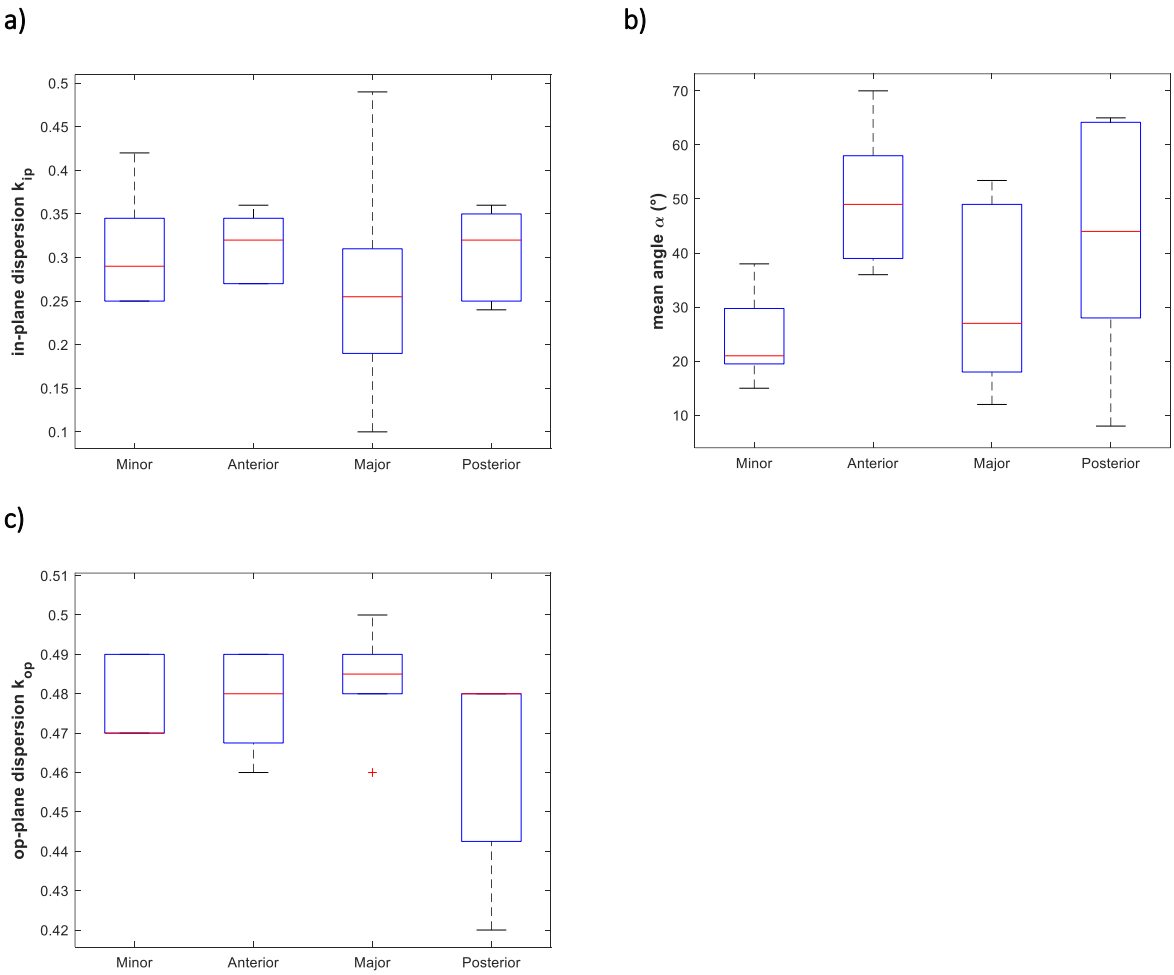

Figure 49 — Box-and-whisker plots of the structural parameters for the ATAA along circumferential direction: (a) in-plane dispersion parameter κ_{ip};(b) out-of-plane dispersion parameter κ_{op};(c) mean fibre angle α.

All samples analysed showed similarly alignment of collagen fibres with a median of κ_{ip} similar in each region. This is visible in Figure 49(a) characterize by the same median value (κ_{ip}=0.305±0.025). The angle α between the mean fibre direction and circumferential direction were smaller in the minor region than another region. For κ_{op} seem that non significant statistically is present κ_{op}=0.49±0.005.

5.2.2. Biaxial testing and constitutive parameters

A non-linear mechanical response was exhibited by the experimental tissue of the aneurysmal aorta ATAAs (Figure 50) for n.6 ATAAs specimens. These are the result of row data of equi-biaxial Cauchy stress vs. stretch behaviour, from different regions: (a) minor, (b) anterior, (c)

major and (d) posterior curvature. The biaxial mechanical behaviour seems to shows wide variability, which underline the importance of patients specific modelling to assess for example the rupture.

The Cauchy stress–stretch curves were fit by the fibre-reinforced constitutive model with the structural parameters fixed at values quantified by multi-photon imaging analysis (Table 9). Figure 51 reported results of fitting the model to four biaxial tension tests of one sample (ATAA-3), considering the major region. With a solid line, it identified the curves fitted.

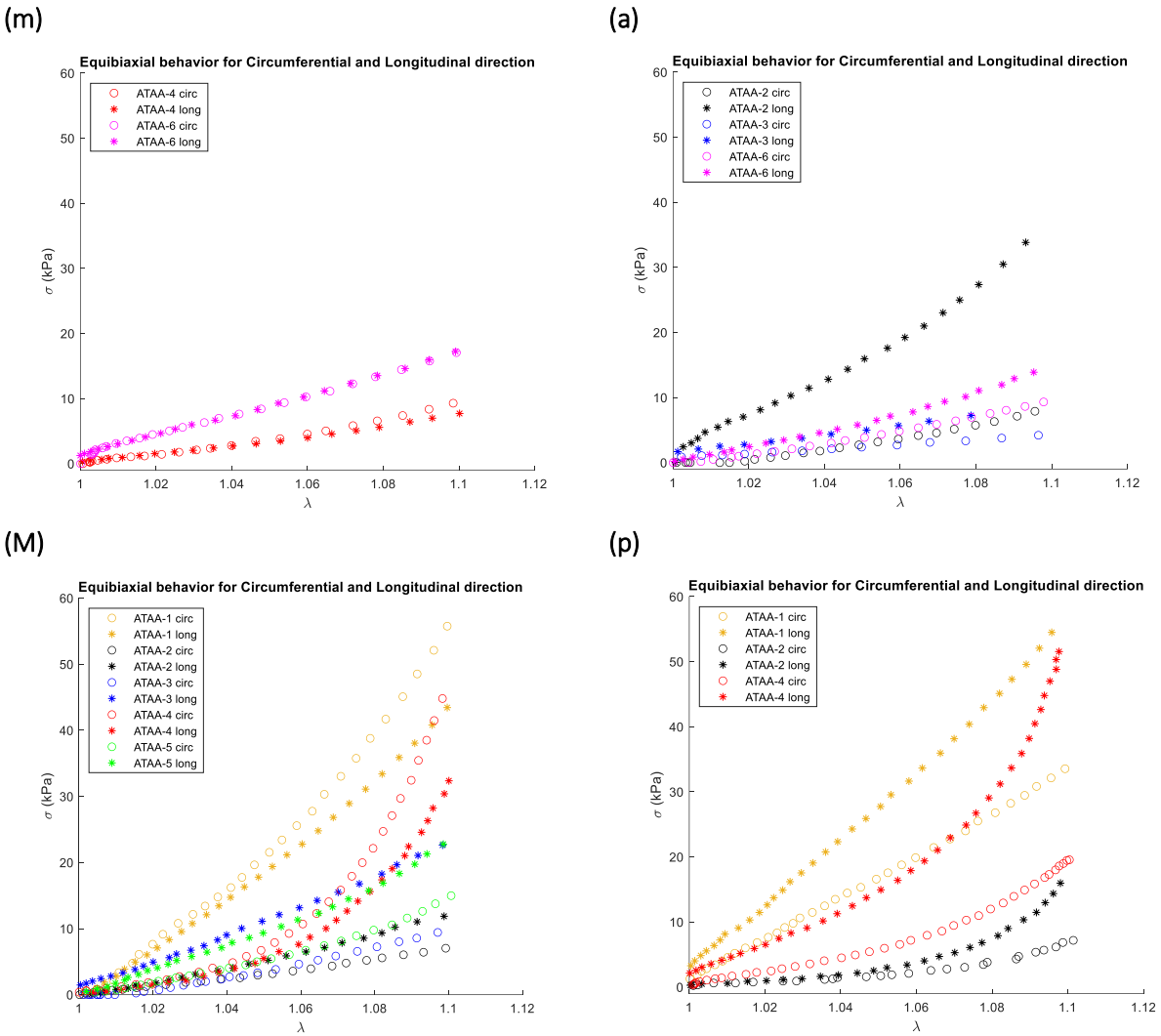

Figure 50 – Cauchy stress versus stretch behaviour of 6 ATAA samples obtained from equibiaxial mechanical tests in the circumferential and longitudinal directions: (m) minor; (a) anterior; (M) major;(p) posterior (p) region for six samples. The data refers to raw data obtained from the biaxial machine.

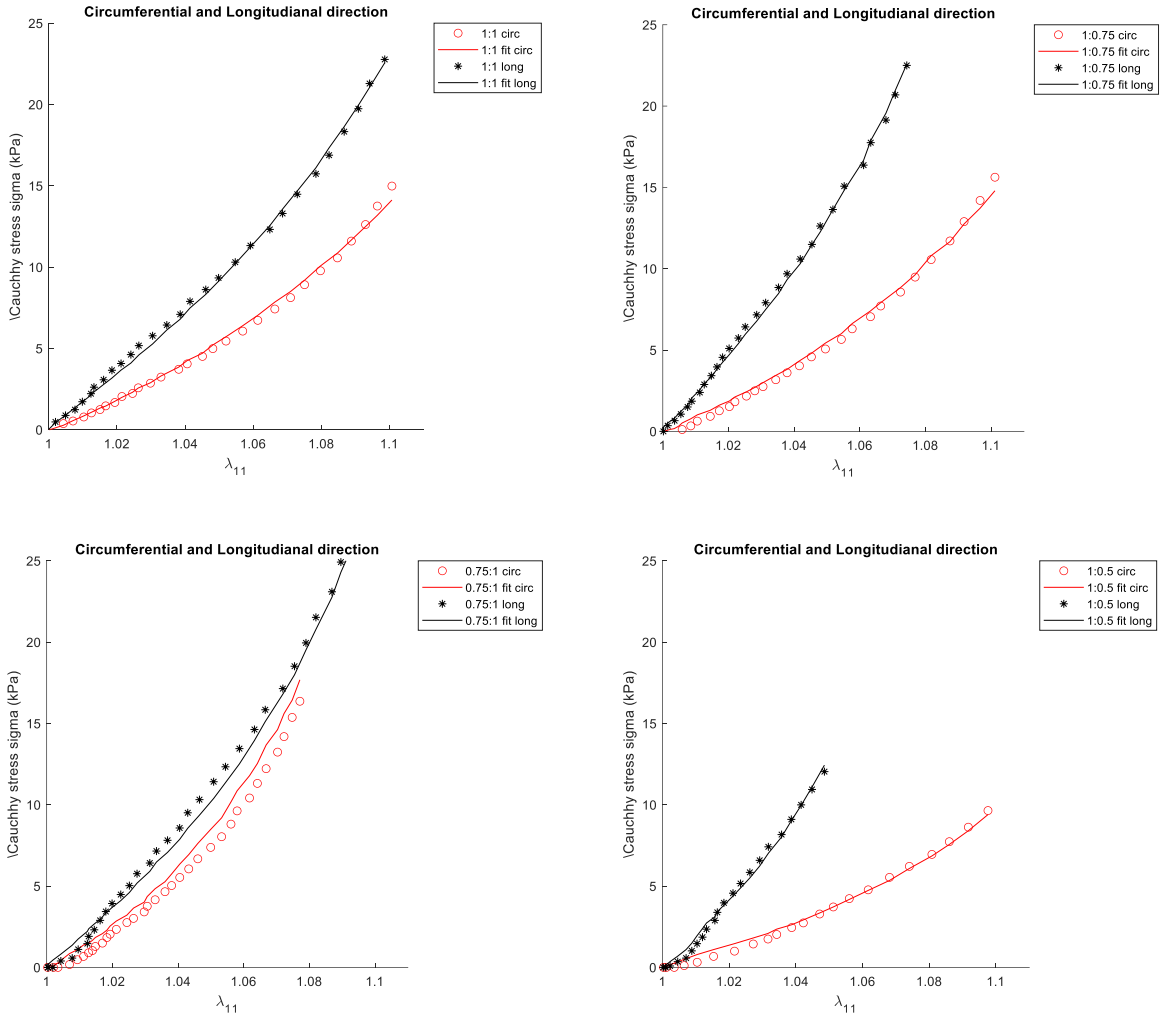

Figure 51 – Representative fitting curve and corresponding stress–stretch data. Black=longitudinal, red=circumferential. Experimental data (and o) are compared with numerical results obtained from the strain-energy function (solid line)*

The material parameters (c, k_1, k_2) for the ATAA samples are summarized in Table 10 respectively. The median of R^2 was $0.98+0.011$, $0.98+ 0.27$, $0.91+0.16$, $0.98+0.061$ for the minor, anterior, major, posterior region, respectively. It was obtained a good fit with R^2 very hight (see Table 10). for each region. Although there are only three material parameters involved, the model agrees very well with experimental data of all samples.

	Minor			Anterior			Major			Posterior		
	n=3			n=5			n=5			n=5		
	Median	[Q1 ; Q3]		Median	[Q1 ; Q3]		Median	[Q1 ; Q3]		Median	[Q1 ; Q3]	
c [kPa]	1.89	1.82	17.14	11.22	7.07	24.78	3.67	0	13.84	7.16	0	25
k_1 [kPa]	8.9	4.45	11.82	13.15	5.44	13.4	34	27.87	43.39	9.06	3.65	49.26
k_2 [-]	2.78	1.39	6.26	8.72	8.08	66.1	5.35	1.32	9.71	16.47	0	23.77
R^2	**0.984**	0.979	0.99	**0.984**	0.779	0.986	**0.913**	0.826	0.993	**0.975**	0.918	0.979

Table 10 – Material parameters (c, k_1, k_2) and related coefficient of determination (R^2) for the minor, anterior, major and posterior region and the intact wall of the ascending aortas determined from biaxial stretching tests; n indicates the number of samples.

In addition, Figure 52, shows box-and-whisker plots for material parameters. The parameters c and k_2 for ATAAs, not a significant correlation between regions (Figure 52). The dimensionless parameter k_1, resembling the exponential stiffening of the loading curves due to the collagen fibres, was significantly higher than for major regions (k_1=34+15.55, p =0.025). Interestingly, by comparing the regions of aortic tissue, the k_2 value was not significantly different between each group.

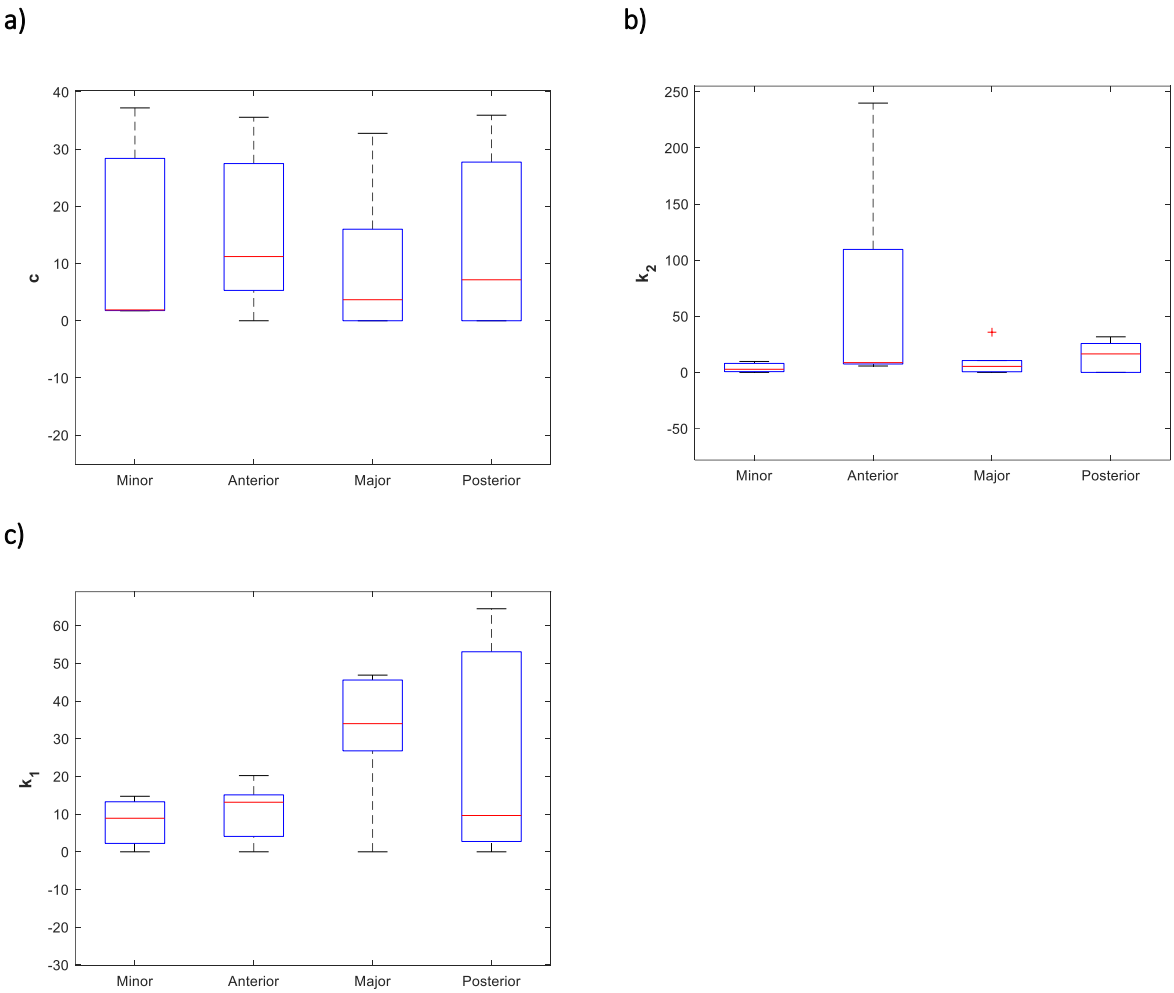

Figure 52 — Box-and-whisker plots of the material parameters (c, k_1,k_2) for the individual regions

To compare the biaxial mechanics in the different regions of the aortic ring, the one way ANOVA was applied to compare the maximum stress for each sample. Results are considered statistically significant when $p < 0.05$. These analyses revealed that the major region is correlated with the anterior region, showing greater stiffness than the other regions in circumferential directions. This result can be explained and confirmed by analysing the structural results from MTP (see Figure 55). Greater stiffness leads to less realignment of the collagen fibres. Statistically, the study carried out for structural parameters show a significant correlation between major and anterior region, show fewer fibres distribution in major is present. The increase in stress in the major region, major curvature, may be responsible for

the realignment of the collagen fibres towards the circumferential direction. Although the samples were not pre-stretched in our study, the fibres in the ATAA samples often appeared straight and much thicker. Six other samples will be analysed in the following study, which allows to define and improve the first results found.

a)

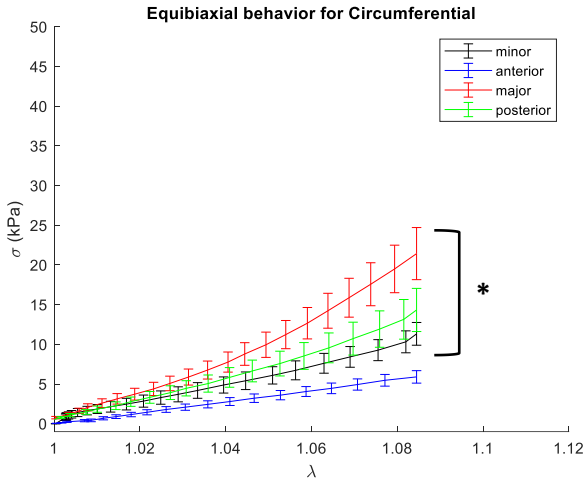

b)

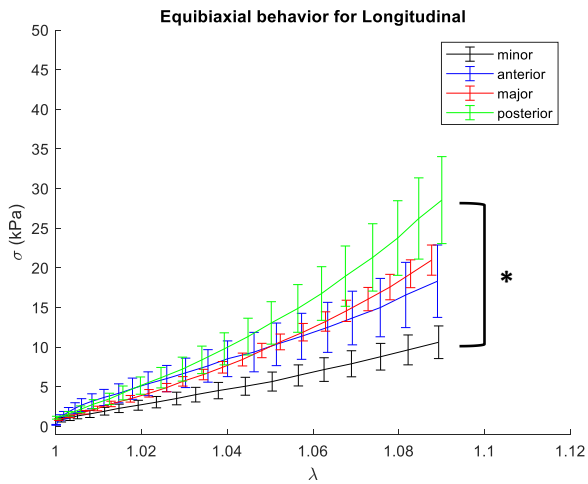

Figure 54 (a,b) – Average results for biaxial samples. Error bars indicated 95% confidence Intervals

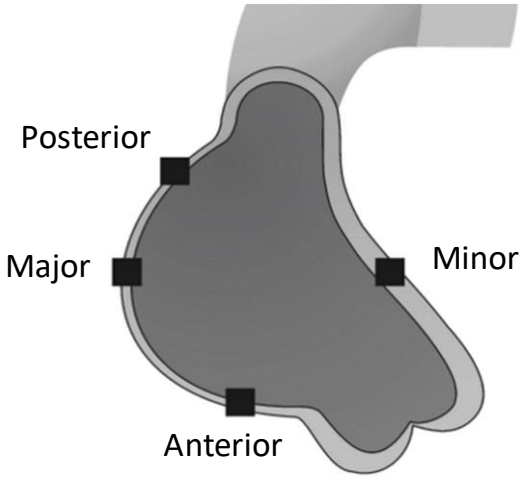

Figure 53 — Visualization of different region in ascending aneurysm aorta tissue. Source from:

a) b)

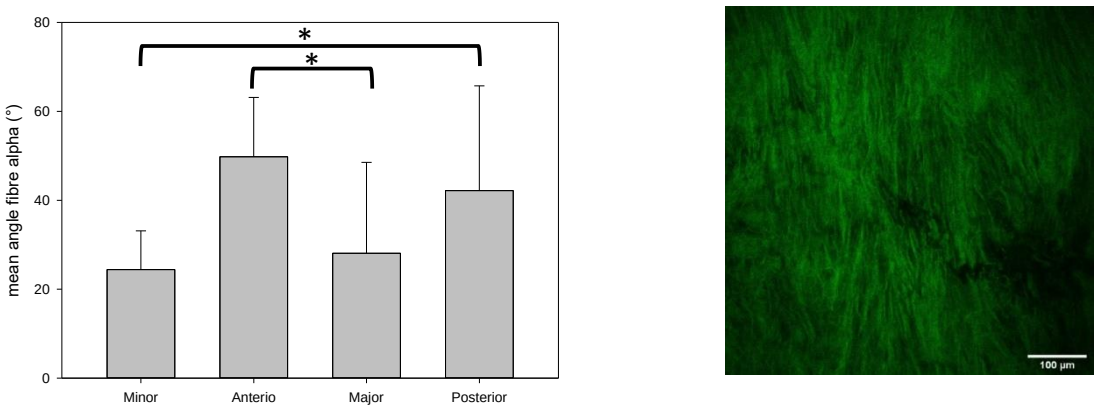

Figure 55 — Anova Test for six cases

5.3. Discussion

The study tends to provide structural data for pathological human ascending aortic tissues in combination with mechanical data for studying the physiology and pathology of human aortas such as ATAAs. In this study, we utilized fibre distribution quantified from multi-photon microscopy to demonstrate an influence of aortic tissues microstructural features on the resulting of mechanics of patient-specific ATAA. A combination of optical clearing and SHG imaging was used to analyse the three-dimensional microstructure without damaging the tissue structure, and mechanical data were obtained from biaxial tests.

The material model used that takes into account the identified non-symmetrical arrangement of collagen fibres (Table 9), documented in [136], was able to provide good adaptations for the ATAA samples although there are only three material parameters involved.

A novel set of structural and material parameters for the material model is provided that could be used in FE simulations. In the following sections, we discuss the obtained structural and mechanical data of the two groups of tissues

5.3.1. Structural Data

In this study, the aortic tissues were not pre-stretched, the structures of the tissues were analysed in the (unloaded) reference configuration and SHG imaging was used. For a short and recent summary of imaging modalities that can reveal the fibrous microstructure including an original investigation of optical polarization tractography to visualize the fibre structure in the bovine carotid artery, see[140]. The study [141] also performed an analysis of AAA collagen fibre dispersion to gain structural data in the unloaded reference configuration. However, that study has some drawbacks, which we could avoid. For example, the measurements were performed manually during histological imaging using polarized light microscopy, which requires embedding the sample in paraffin and mechanical sectioning and staining with picrosirius red so that only a very small thin slice of a fixed sample can be imaged. Our approach has the advantages that tissue clearing does not change the dimensions of the sample in contrast with [141]. In this study, we were able to attain a continuous three- dimensional dispersion of the collagen fibre orientations throughout the entire thickness.

ATAA wall samples showed a large variation in tissue composition. This observation is in accordance with the study [128], which shows a complete loss of the normal architecture and loss of the distinction between medial and adventitial collagen organization.

Although in the dispersion parameters of collagen fibres were not found statistically significant in this study, It found differences in fibres orientation have a profound impact on biaxial behaviour. Moreover, we observed that specimens from aneurysmal ascending aorta in the major region were found to exhibit a majority of fibre angles symmetrically oriented in the circumferential direction which was consistent with other reports [142][137]. Collectively, these data on the deranged collagen fibre architecture might explain the reduced

biomechanical strength of the aneurysmal aorta compared to the normal ascending aorta found previously [122].

As the significant influence of the collagen structure on the mechanics of healthy and diseased collagenous tissues has long been known, the different microstructure in different regions of a sample may explain the diversity in local AAA stress states. We found no significant influence of the aneurysm diameter on the structural and material parameters, which strengthens the hypothesis that the diameter criterion is insufficient, which is in line with previous findings.

5.3.2. Mechanical data

Biaxial tensile tests have demonstrated a non-linear and stiffer behaviour of ATAAs [143] with the major region having greater stiffness [144] respect other regions aortic location [116][119][106].

Haskett and collaborators [142] demonstrated that the increased stiffness of abdominal aorta is associated with decreased collagen fibre alignment in the circumferential direction, and this may predispose to aneurysm development. Such a result is consistent with the decreased circumferential fibre directionality found in our study for the experimentally aneurysmal aorta (Figure 54 Figure 55).

There is a growing interest in moving from basic phenomenological constitutive modelling to a microstructurally- based approach to provide constitutive parameters with a more natural and physical interpretation. Rodriguez et al. [145] compared the ability of the anisotropic purely-phenomenological model and an anisotropic structurally motivated Gasser-type model to fit data for abdominal aortic aneurysms reported by Vande Geest et al. [115]. The latter demonstrated that the Fung-type model was unable to fit the more isotropic behaviour of young abdominal aortic tissues. Therefore, there is need for a new paradigm for

stress analyses including microstructurally-based models since finite element stress estimation can provide better indicators of the likelihood for rupture or dissection than the clinically used maximum diameter criterion [82]. Towards this end, we emphasize the use of fibre-reinforced constitutive modelling to incorporate the micro structural defect of collagen fibres inherent to the aneurysmal ascending aorta.

We observed an inverse relationship between the maximum Cauchy stress (Figure 54a) and the mean fibre angle (Figure 55). Specifically, the higher the mean fibre angle from the loading direction the lower the Cauchy stress. Further investigation is needed to clarify the possible influence of the structural parameters other than the mean fibre direction even though the failure properties did not show any clear dependencies on these parameters.

Concerning the mean curve for each specimen, the behaviour of major specimens along circumferential direction showed the highest Cauchy stress and the lowest mean fibre angle an (8°). It is likely that this very high Cauchy stress is not only a result of the mean fibre angle but also due to the presence of the adventitia (20% of the thickness). It is well accepted that the adventitia acts as a protective layer against tissue failure due to its high collagen content.

Not a significant difference in the parameter c, relating to the ground matrix, and k_2, relating to the stiffness of the collagen tissue was observed. The median parameter c is similar in each region. As can be seen from Figure 50, the biaxial mechanical AAA behaviour shows wide variability, which underlines the importance of patient-specific modelling to assess rupture risk. Any difference in the finding to previous studies could be due to this variability, which again highlights the need to acquire structural data in combination with mechanical data in each case. The fits of the used material model to the experimental data were very good throughout all AAA samples. Despite the small number of available samples,

we report significant correlations between material and structural parameters. Our results show a striking dependence on local fibre orientation and degree of alignment. These results support the conclusion that mechanics aneurysm depends on the underlying fibre orientation and degree of alignment, which affect the tissue behaviour and tissue failure on a whole.

5.4. Conclusion

The present study will provide a unique set of mechanical and structural data that highlight the strong influence of the aortic microstructure tissues on its mechanics properties under biaxial test. The preliminary data presented show that the mean collagen fibre angle has a clear influence on the mechanics properties of the specimens subjected to the biaxial test. Furthermore, contents of collagen and elastic fibres should also be considered – especially in the cases where they are extremely high/low. In line with recent studies on aortic tissue [146] and bovine pericardium [147], the results of this work suggest that the microstructure should be taken into account when developing a mechanical approach. This study should be considered as a basis for further research that focuses on the predictive capabilities of the microstructural parameters for the failure properties of soft biological tissues, and it is a step towards realistic modelling of tissue failure. In addition, it might help to address clinical challenges of rupture prediction of dilated aortas with appropriate imaging techniques.

5.5. Future work

In the future, more effort should be made to better investigate collagen fibre undulation and thickness measurement, as straight and thick collagen struts were spotted on several samples throughout the thickness. Improved imaging of the aorta may provide in vivo information regarding aortic geometry, structure and anisotropy, and when combined with a

hemodynamic assessment it may have the potential to identify patients at high risk and to access rupture risk individually thereby facilitating prophylactic treatment of aneurysms. These data shown in this chapter will be increased and improved with other samples.

Future studies will be undertaken to incorporate more refined constitutive formulations including further descriptors of tissue microstructure [148] or based on multiscale homogenization approaches that couple microscale histological features with nanoscale biochemical properties. Indeed, the use of more refined constitutive formulations can lead to better quantitative predictions of aortic wall stresses and thus to improved risk stratifications of ATAAs

5.6. Acknowledgements

The authors are indebted to Professor G.A. Holzapfel for the experimental research on the aneurysm of the ascending thoracic aorta at the University of Graz and his collaboration in the use of his constitutive models. The author gratefully acknowledges the excellent support and valuable discussions of Dr Selda Scherifiva, and Prof. Gerhard Sommer. Financial support for this research was provided by an "Ernst March worldwide" scholarship, by funds of the Austrian Federal Ministry of Education, Science and Research (BMBWF). This support is gratefully acknowledged.

Bibliography

[1] E. J. Benjamin *et al.*, *Heart Disease and Stroke Statistics-2019 Update: A Report From the American Heart Association*, vol. 139, no. 10. 2019.

[2] W. D. Clouse *et al.*, "Acute Aortic Dissection: Population-Based Incidence Compared with Degenerative Aortic Aneurysm Rupture," *Mayo Clin. Proc.*, vol. 79, no. 2, pp. 176–180, 2004, doi: 10.4065/79.2.176.

[3] BHF, "Heart and Circulatory Disease Statistics 2019," *2019 Stat. Compend.*, no. April, pp. 94–96, 2019, [Online]. Available: https://www.bhf.org.uk/what-we-do/our-research/heart-statistics/heart-statistics-publications/cardiovascular-disease-statistics-2019.

[4] G. A. Holzapfel and R. W. Ogden, *Biomechanics of Soft Tissue in Cardiovascular Systems*, vol. XXXIII, no. 2. 2003.

[5] M. E. Nimni, *Collagen: Biochemistry, Volume 1*. .

[6] Y. Bernard *et al.*, "False lumen patency as a predictor of late outcome in aortic dissection," *Am. J. Cardiol.*, vol. 87, no. 12, pp. 1378–1382, 2001, doi: 10.1016/S0002-9149(01)01556-9.

[7] Y. C. Fung., *Biomechanics. Mechanical Properties of Living Tissues*, 2nd editio., vol. 24, no. 4. New York, 1993.

[8] M. J. Buehler, "Nanomechanics of collagen fibrils under varying cross-link densities: Atomistic and continuum studies," *J. Mech. Behav. Biomed. Mater.*, vol. 1, no. 1, pp.

59–67, 2008, doi: 10.1016/j.jmbbm.2007.04.001.

[9] Gerhard A. Holzapfel, *Nonlinear Solid Mechanics A Continuum Approach for Engineering*. 2000.

[10] D. Wu, Y. H. Shen, L. Russell, J. S. Coselli, and S. A. Lemaire, "Molecular mechanisms of thoracic aortic dissection," *J. Surg. Res.*, vol. 184, no. 2, pp. 907–924, 2013, doi: 10.1016/j.jss.2013.06.007.

[11] R. V. Iozzo and L. Schaefer, "Proteoglycan form and function: A comprehensive nomenclature of proteoglycans," *Matrix Biol.*, vol. 42, pp. 11–55, 2015, doi: 10.1016/j.matbio.2015.02.003.

[12] T. N. Wight, M. G. Kinsella, and E. E. Qwarnström, "The role of proteoglycans in cell adhesion, migration and proliferation," *Curr. Opin. Cell Biol.*, vol. 4, no. 5, pp. 793–801, 1992, doi: 10.1016/0955-0674(92)90102-I.

[13] M. G. Kinsella and T. N. Wight, "Modulation of sulfated proteoglycan synthesis by bovine aortic endothelial cells during migration," *J. Cell Biol.*, vol. 102, no. 3, pp. 679–687, 1986, doi: 10.1083/jcb.102.3.679.

[14] J. E. Wagenseil and R. P. Mecham, "Vascular ECM and arterial mechanics," *Physiol. Rev.*, vol. 89, no. 3, pp. 957–989, 2009, doi: 10.1152/physrev.00041.2008.Vascular.

[15] G. S. Gupta, A. Gupta, and R. K. Gupta, "Animal lectins: Form, function and clinical applications," *Anim. Lectins Form, Funct. Clin. Appl.*, vol. 9783709110, pp. 1–1108, 2012, doi: 10.1007/978-3-7091-1065-2.

[16] C. A. Conti *et al.*, "Biomechanical implications of the congenital bicuspid aortic valve: A finite element study of aortic root function from in vivo data," *J. Thorac. Cardiovasc. Surg.*, vol. 140, no. 4, pp. 890-896.e2, 2010, doi: 10.1016/j.jtcvs.2010.01.016.

[17] T. M. Tadros, M. D. Klein, and O. M. Shapira, "Ascending aortic dilatation associated with bicuspid aortic valve. Pathophysiology, molecular biology, and clinical implications," *Circulation*, vol. 119, no. 6, pp. 880–890, 2009, doi: 10.1161/CIRCULATIONAHA.108.795401.

[18] Alain Carpentier; David H. Adams; Farzan Filsouf, *Reconstructive Valve Surgery. From Valve Analysis to Valve Reconstruction*, vol. 6, no. 2. Jeff Patterson, 1991.

[19] C. A. J. Schulze-Bauer, P. Regitnig, and G. A. Holzapfel, "Mechanics of the human femoral adventitia including the high-pressure response," *Am. J. Physiol. - Hear. Circ. Physiol.*, vol. 282, no. 6 51-6, pp. 2427–2440, 2002, doi: 10.1152/ajpheart.00397.2001.

[20] P. A. Iazzo, *Handbook of cardiac anatomy, physiology, and devices*, Springer S., vol. 53, no. 9. 2009.

[21] F. Gao, Z. Guo, M. Sakamoto, and T. Matsuzawa, "Fluid-structure interaction within a layered aortic arch model," *J. Biol. Phys.*, vol. 32, no. 5, pp. 435–454, 2006, doi: 10.1007/s10867-006-9027-7.

[22] D. Litmanovich, A. A. Bankier, L. Cantin, V. Raptopoulos, and P. M. Boiselle, "CT and MRI in diseases of the aorta," *Am. J. Roentgenol.*, vol. 193, no. 4, pp. 928–940, 2009, doi: 10.2214/AJR.08.2166.

[23] J. A. Elefteriades, "Thoracic aortic aneurysm: Reading the enemy's playbook," *Yale J.*

Biol. Med., vol. 81, no. 4, pp. 175–186, 2008, doi: 10.1016/j.cpcardiol.2008.01.004.

[24] J. A. Elefteriades, A. Sang, G. Kuzmik, and M. Hornick, "Guilt by association: paradigm for detecting a silent killer (thoracic aortic aneurysm)," *Open Hear.*, vol. 2, no. 1, p. e000169, 2015, doi: 10.1136/openhrt-2014-000169.

[25] J. F. F. John W. Joyce, "Aneurysms of the thoracic aorta. A Clinical Study with Special Reference to Prognosis," *Helv. Chir. Acta*, vol. 29, pp. 75–89, 1962.

[26] M. A. Coady *et al.*, "What is the appropriate size criterion for resection of thoracic aortic aneurysms?," *J. Thorac. Cardiovasc. Surg.*, vol. 113, no. 3, pp. 476–491, 1997, doi: 10.1016/S0022-5223(97)70360-X.

[27] A. Della Della Corte *et al.*, "The ascending aorta with bicuspid aortic valve: A phenotypic classification with potential prognostic significance," *Eur. J. Cardio-thoracic Surg.*, vol. 46, no. 2, pp. 240–247, 2014, doi: 10.1093/ejcts/ezt621.

[28] B. M. Schaefer *et al.*, "The bicuspid aortic valve: An integrated phenotypic classification of leaflet morphology and aortic root shape," *Heart*, vol. 94, no. 12, pp. 1634–1638, 2008, doi: 10.1136/hrt.2007.132092.

[29] S. Verma and S. C. Siu, "Aortic dilatation in patients with bicuspid aortic valve," *N. Engl. J. Med.*, vol. 370, no. 20, pp. 1920–1929, 2014, doi: 10.1056/NEJMra1207059.

[30] C. S. Roy, "The Elastic Properties of the Arterial Wall," *J. Physiol.*, vol. 3, no. 2, pp. 125–159, 1881, doi: 10.1113/jphysiol.1881.sp000088.

[31] D. H. Bergel, "The visco-elastic properties of the arterial wall.," *Pulse*, vol. 1960, 1960.

[32] Y. C. Fung, *A First Course in Continuum Mechanics_ for Physical and Biological Engineers and Scientists-Prentice Hall (1994) (1).pdf*, Third Edit. 1994.

[33] C. J. Chuong and Y. C. Fung, "On residual stress in arteries," *J. Biomech. Eng.,* vol. 108, no. May, pp. 189–192, 1986.

[34] and S. G. A. Sani, C. Berry, "Effect of age and sex on residual stress in the aorta," *J. Vasc. Res*, pp. 32:398–405, 1995.

[35] R. S. Lakes and R. Vanderby, "Interrelation of creep and relaxation: A modeling approach for ligaments," *J. Biomech. Eng.*, vol. 121, no. 6, pp. 612–615, 1999, doi: 10.1115/1.2800861.

[36] S. Q. L. and Y. C. Fung., "Zero-stress states of arteries," vol. 110:82–84, 1988.

[37] S. E. Greenwald, J. E. Moore, A. Rachev, T. P. C. Kane, and J. J. Meister, "Experimental investigation of the distribution of residual strains in the artery wall," *J. Biomech. Eng.*, vol. 119, no. 4, pp. 438–444, 1997, doi: 10.1115/1.2798291.

[38] G. A. Holzapfel, G. Sommer, M. Auer, P. Regitnig, and R. W. Ogden, "Layer-specific 3D residual deformations of human aortas with non-atherosclerotic intimal thickening," *Ann. Biomed. Eng.*, vol. 35, no. 4, pp. 530–545, 2007, doi: 10.1007/s10439-006-9252-z.

[39] T. Matsumoto, T. Goto, and M. Sato, "Microscopic residual stress caused by the mechanical heterogeneity in the Lamellar unit of the porcine thoracic aortic wall," *JSME Int. Journal, Ser. A Solid Mech. Mater. Eng.*, vol. 47, no. 3, pp. 341–348, 2004, doi: 10.1299/jsmea.47.341.

[40] K. Takamizawa and K. Hayashi, “Strain energy density function and uniform strain hypothesis for arterial mechanics,” *Journal of Biomechanics*, vol. 20, no. 1. pp. 7–17, 1987, doi: 10.1016/0021-9290(87)90262-4.

[41] W. W. von Maltzahn, R. G. Warriyar, and W. F. Keitzer, “Experimental measurements of elastic properties of media and adventitia of bovine carotid arteries,” *J. Biomech.*, vol. 17, no. 11, pp. 839–847, 1984, doi: 10.1016/0021-9290(84)90142-8.

[42] C. J. Chuong and Y. C. Fung, “Three–dimensional stress distribution in arteries,” *J. Biomech. Eng.*, vol. 105, no. 3, pp. 268–274, 1983, doi: 10.1115/1.3138417.

[43] G. A. Holzapfel and H. W. Weizsäcker, “Biomechanical behavior of the arterial wall and its numerical characterization,” *Comput. Biol. Med.*, vol. 28, no. 4, pp. 377–392, 1998, doi: 10.1016/S0010-4825(98)00022-5.

[44] A. I. Arroyave G., R. G. Lima, P. A. L. S. Martins, N. Ramião, and R. M. N. Jorge, “Methodology for mechanical characterization of soft biological tissues: Arteries,” *Procedia Eng.*, vol. 110, pp. 74–81, 2015, doi: 10.1016/j.proeng.2015.07.012.

[45] R. J. Minns, P. D. Soden, and D. S. Jackson, “The role of the fibrous components and ground substance in the mechanical properties of biological tissues: A preliminary investigation,” *J. Biomech.*, vol. 6, no. 2, pp. 153–165, 1973, doi: 10.1016/0021-9290(73)90084-5.

[46] S. C. Cowin, *Mechanics Tissue*. 2007.

[47] R. W. Odgen, *Non-Linear Elastic Deformations*, Dover Publ. 2013.

[48] R. W. Odgen and Y. B. Fu, *Non-Linear Elastic Deformations*, Cambridge. 2001.

[49] G. A. Holzapfel, T. C. Gasser, and R. W. Ogden, “A new constitutive framework for arterial wall mechanics and a comparative study of material models,” *J. Elast.*, vol. 61, no. 1–3, pp. 1–48, 2000, doi: 10.1023/A:1010835316564.

[50] S. Roy, C. Boss, R. Rezakhaniha, and N. Stergiopulos, “Experimental characterization of the distribution of collagen fiber recruitment,” *J. Biorheol.*, vol. 24, no. 2, pp. 84–93, 2010, doi: 10.1007/s12573-011-0027-2.

[51] H. Chen *et al.*, “Biaxial deformation of collagen and elastin fibers in coronary adventitia,” *J. Appl. Physiol.*, vol. 115, no. 11, pp. 1683–1693, 2013, doi: 10.1152/japplphysiol.00601.2013.

[52] and R. L. G. Ruoya Wang, Luke P. Brewster, “In-Situ Characterization of the Uncrimping Process of Arterial Collagen Fibers Using Two-Photon Confocal Microscopy and Digital Image Correlation,” *Physiol. Behav.*, vol. 176, no. 1, pp. 139–148, 2017, doi: 10.1016/j.jbiomech.2013.08.001.In-Situ.

[53] B. Fata *et al.*, “Regional structural and biomechanical alterations of the ovine main pulmonary artery during postnatal growth,” *J. Biomech. Eng.*, vol. 135, no. 2, pp. 1–11, 2013, doi: 10.1115/1.4023389.

[54] L. H. Timmins, Q. Wu, A. T. Yeh, J. E. Moore, and S. E. Greenwald, “Structural inhomogeneity and fiber orientation in the inner arterial media,” *Am. J. Physiol. - Hear. Circ. Physiol.*, vol. 298, no. 5, pp. 1537–1545, 2010, doi: 10.1152/ajpheart.00891.2009.

[55] F. Helmchen and W. Denk, “Deep tissue two-photon microscopy,” *Nat. Methods*, vol. 2,

no. 12, pp. 932–940, 2005, doi: 10.1038/nmeth818.

[56] and W. W. W. Denk, W., J. H. Strickler, “Two-photon laser scanning fluorescence microscopy,” *Science (80-.).*, vol. 278, pp. 73–76, 1990.

[57] B. R. Masters and P. T. C. So, “Multi-photon excitation microscopy and confocal microscopy imaging of in vivo human skin: A comparison,” *Microsc. Microanal.*, vol. 5, no. 4, pp. 282–289, 1999, doi: 10.1017/S1431927699990311.

[58] P. T. C. So, H. Kim, and I. E. Kochevar, “Two-photon deep tissue ex vivo imaging of mouse dermal and subcutaneous structures,” *Opt. Express*, vol. 3, no. 9, p. 339, 1998, doi: 10.1364/oe.3.000339.

[59] J. M. Squirrell, D. L. Wokosin, J. G. White, and B. D. Bavister, “Long-term two-photon fluorescence imaging of mammalian embryos without compromising viability,” *Nat. Biotechnol.*, vol. 17, no. 8, pp. 763–767, 1999, doi: 10.1038/11698.

[60] A. Diaspro and M. Robello, “Two-photon excitation of fluorescence for three-dimensional optical imaging of biological structures,” *J. Photochem. Photobiol. B Biol.*, vol. 55, no. 1, pp. 1–8, 2000, doi: 10.1016/S1011-1344(00)00028-2.

[61] B. R. Masters and P. T. C. So, “Confocal microscopy and multi-photon excitation microscopy of human skin in vivo,” *Opt. Express*, vol. 8, no. 1, p. 2, 2001, doi: 10.1364/oe.8.000002.

[62] Y. Guo *et al.*, “Second-harmonic tomography of tissues,” *Opt. Lett*, vol. 22, no. 9, p. 733, 1997, doi: 10.1364/ol.23.000733.

[63] R. Gauderon, P. B. Lukins, and C. J. R. Sheppard, “Three-dimensional second-harmonic generation imaging with femtosecond laser pulses,” *Opt. Lett.*, vol. 23, no. 15, p. 1209, 1998, doi: 10.1364/ol.23.001209.

[64] P. J. Campagnola, H. A. Clark, W. A. Mohler, A. Lewis, and L. M. Loew, “Second-harmonic imaging microscopy of living cells,” *J. Biomed. Opt.*, vol. 6, no. 3, p. 277, 2001, doi: 10.1117/1.1383294.

[65] L. Moreaux, O. Sandre, and J. Mertz, “Membrane imaging by second-harmonic generation microscopy,” *J. Opt. Soc. Am. B*, vol. 17, no. 10, p. 1685, 2000, doi: 10.1364/josab.17.001685.

[66] P. J. Campagnola, A. C. Millard, M. Terasaki, P. E. Hoppe, C. J. Malone, and W. A. Mohler, “Three-dimensional high-resolution second-harmonic generation imaging of endogenous structural proteins in biological tissues,” *Biophys. J.*, vol. 82, no. 1, pp. 493–508, 2002, doi: 10.1016/S0006-3495(02)75414-3.

[67] Zoumi A., A. Yeh, and B. J. Tromberg, “Imaging cells and extracellular matrix in vivo by using second-harmonic generation and two-photon excited fluorescence,” *Proc. Natl. Acad. Sci. U. S. A.*, vol. 99, no. 17, pp. 11014–11019, 2002, doi: 10.1073/pnas.172368799.

[68] R. Richards-Kortum and E. Sevick-Muraca, “Quantitative optical spectroscopy for tissue diagnosis,” *Annu. Rev. Phys. Chem.*, vol. 47, pp. 555–606, 1996, doi: 10.1146/annurev.physchem.47.1.555.

[69] M. Goppert-Mayer, “Uber elementarekte mit zwei quantensprunger,” *Ann. Phys.*, vol.

9, no. 273, 1931.

[70] W. R. Zipfel, R. M. Williams, and W. W. Webb, “Nonlinear magic: Multiphoton microscopy in the biosciences,” *Nat. Biotechnol.*, vol. 21, no. 11, pp. 1369–1377, 2003, doi: 10.1038/nbt899.

[71] A. Zoumi, X. Lu, G. S. Kassab, and B. J. Tromberg, “Imaging coronary artery microstructure using second-harmonic and two-photon fluorescence microscopy.,” *Biophys. J.*, vol. 87, no. 4, pp. 2778–2786, 2004, doi: 10.1529/biophysj.104.042887.

[72] U. A. S. K.Konig, K.Schenke-Layland, I.Riemann, “Multiphoton autofluorescence imaging of intratissue elastic fibers,” *Office*, vol. 26, pp. 495–500, 2005, doi: 10.1016/j.biomaterials.

[73] R. T. A. Megens *et al.*, “Two-photon microscopy of vital murine elastic and muscular arteries: Combined structural and functional imaging with subcellular resolution,” *J. Vasc. Res.*, vol. 44, no. 2, pp. 87–98, 2007, doi: 10.1159/000098259.

[74] T. Parasassi *et al.*, “Two-photon microscopy of aorta fibers shows proteolysis induced by LDL hydroperoxides,” *Free Radic. Biol. Med.*, vol. 28, no. 11, pp. 1589–1597, 2000, doi: 10.1016/S0891-5849(00)00275-6.

[75] K. Schenke-Layland, I. Riemann, U. A. Stock, and K. König, “Imaging of cardiovascular structures using near-infrared femtosecond multiphoton laser scanning microscopy,” *J. Biomed. Opt.*, vol. 10, no. 2, p. 024017, 2005, doi: 10.1117/1.1896966.

[76] Z. Deyl, K. Macek, M. Adam, and Vancikova, “Studies on the chemical nature of elastin fluorescence,” *Biochim. Biophys. Acta*, vol. 625, no. 2, pp. 248–254, 1980, doi:

10.1016/0005-2795(80)90288-3.

[77] J. B, *Design and Assembly of a Multimodal Nonlinear Laser Scanning Microscope*. 2006.

[78] R. . Quimby, *Photonics and Lasers: An Introduction*. 2006.

[79] R. M. Williams, W. R. Zipfel, and W. W. Webb, "Interpreting Second-Harmonic Generation Images of Collagen I Fibrils," *Biophys. J.*, vol. 88, no. 2, pp. 1377–1386, 2005, doi: 10.1529/biophysj.104.047308.

[80] R. Sanders, A. Draaijer, H. C. Gerritsen, P. M. Houpt, and Y. K. Levine, "Quantitative pH imaging in cells using confocal fluorescence lifetime imaging microscopy," *Analytical Biochemistry*, vol. 227, no. 2. pp. 302–308, 1995, doi: 10.1006/abio.1995.1285.

[81] H. Szmacinski and J. R. Lakowicz, "Optical Measurements of pH Using Fluorescence Lifetimes and Phase-Modulation Fluorometry," *Anal. Chem.*, vol. 65, no. 13, pp. 1668–1674, 1993, doi: 10.1021/ac00061a007.

[82] J. R. Lakowicz, "Fluorescence Lifetime Imaging," *Anal Biochem*, vol. 202, no. 2, pp. 316–330, 1992, doi: 10.1016/0003-2697(92)90112-k.

[83] S. B. Bambot *et al.*, "Sensing oxygen through skin using a red diode laser and fluorescence lifetimes," *Biosens. Bioelectron*, vol. 10, no. (6-7), pp. 643–652, 1995, doi: 10.1016/0956-5663(95)96941-q.Sensing.

[84] F. S. Wouters, P. J. Verveer, and P. I. H. Bastiaens, "Imaging biochemistry inside cells," *Trends Cell Biol.*, vol. 11, no. 5, pp. 203–211, 2001, doi: 10.1016/S0962-8924(01)01982-1.

[85] M. Peter and S. M. Ameer-Beg, “Imaging molecular interactions by multiphoton FLIM,” *Biol. Cell*, vol. 96, no. 3, pp. 231–236, 2004, doi: 10.1016/j.biolcel.2003.12.006.

[86] A. Peyker, O. Rocks, and P. I. H. Bastiaens, “Imaging activation of two Ras isoforms simultaneously in a single cell,” *ChemBioChem*, vol. 6, no. 1, pp. 78–85, 2005, doi: 10.1002/cbic.200400280.

[87] E. Gratton, “Fluorescence lifetime imaging for the two-photon microscope: time-domain and frequency-domain methods,” *J. Biomed. Opt.*, vol. 8, no. 3, p. 381, 2003, doi: 10.1117/1.1586704.

[88] K. Suhling *et al.*, “Imaging the environment of green fluorescent protein,” *Biophys. J.*, vol. 83, no. 6, pp. 3589–3595, 2002, doi: 10.1016/S0006-3495(02)75359-9.

[89] S. Pelet, M. J. Previte, L. H. Laiho, and P. T. So, “A fast global fitting algorithm for fluorescence lifetime imaging microscopy based on image segmentation.,” *Biophys. J.*, vol. 87, no. 4, pp. 2807–2817, 2004, doi: 10.1529/biophysj.104.045492.

[90] P. J. Verveer, A. Squire, and P. I. H. Bastiaens, “Global analysis of fluorescence lifetime imaging microscopy data,” *Biophys. J.*, vol. 78, no. 4, pp. 2127–2137, 2000, doi: 10.1016/S0006-3495(00)76759-2.

[91] A. H. A. Clayton, Q. S. Hanley, and P. J. Verveer, “Graphical representation and multicomponent analysis of single-frequency fluorescence lifetime imaging microscopy data,” *J. Microsc.*, vol. 213, no. 1, pp. 1–5, 2004, doi: 10.1111/j.1365-2818.2004.01265.x.

[92] G. I. Redford and R. M. Clegg, “Polar plot representation for frequency-domain analysis

of fluorescence lifetimes," *J. Fluoresc.*, vol. 15, no. 5, pp. 805–815, 2005, doi: 10.1007/s10895-005-2990-8.

[93] E. Gratton, "The Phasor approach : Application to FRET analysis and Tissue autofluorescence," *13th LFD Work.*, 2018.

[94] M. Liu, L. Liang, and W. Sun, "A new inverse method for estimation of in vivo mechanical properties of the aortic wall," *J. Mech. Behav. Biomed. Mater.*, vol. 72, no. May, pp. 148–158, 2017, doi: 10.1016/j.jmbbm.2017.05.001.

[95] K. Miller and J. Lu, "On the prospect of patient-specific biomechanics without patient-specific properties of tissues," *J. Mech. Behav. Biomed. Mater.*, vol. 27, pp. 154–166, 2013, doi: 10.1016/j.jmbbm.2013.01.013.

[96] G. R. Joldes, K. Miller, A. Wittek, and B. Doyle, "A simple, effective and clinically applicable method to compute abdominal aortic aneurysm wall stress," *J. Mech. Behav. Biomed. Mater.*, vol. 58, pp. 139–148, 2016, doi: 10.1016/j.jmbbm.2015.07.029.

[97] S. Pasta *et al.*, "Constitutive modeling of ascending thoracic aortic aneurysms using microstructural parameters," *Med. Eng. Phys.*, vol. 38, no. 2, pp. 121–130, 2016, doi: 10.1016/j.medengphy.2015.11.001.

[98] A. N. Azadani *et al.*, "Biomechanical properties of human ascending thoracic aortic aneurysms," *Ann. Thorac. Surg.*, vol. 96, no. 1, pp. 50–58, 2013, doi: 10.1016/j.athoracsur.2013.03.094.

[99] G. R. Joldes, K. Miller, A. Wittek, and B. Doyle, "A simple, effective and clinically applicable method to compute abdominal aortic aneurysm wall stress," *J. Mech. Behav.*

Biomed. Mater., vol. 58, pp. 139–148, 2016, doi: 10.1016/j.jmbbm.2015.07.029.

[100] J. E. Caitlin Martina, Wei Suna, Thuy Phama, "Predictive biomechanical analysis of ascending aortic aneurysm rupture potential," *Acta Biomater*, 2013, doi: 10.1016/j.actbio.2013.07.044.

[101] O. Trabelsi, F. M. Davis, J. F. Rodriguez-Matas, A. Duprey, and S. Avril, "Patient specific stress and rupture analysis of ascending thoracic aneurysms," *J. Biomech.*, vol. 48, no. 10, pp. 1836–1843, 2015, doi: 10.1016/j.jbiomech.2015.04.035.

[102] G. Martufi, T. C. Gasser, J. J. Appoo, and E. S. Di Martino, "Mechano-biology in the thoracic aortic aneurysm: a review and case study," *Biomech. Model. Mechanobiol.*, vol. 13, no. 5, pp. 917–928, 2014, doi: 10.1007/s10237-014-0557-9.

[103] J. Biehler, M. W. Gee, and W. A. Wall, "Towards efficient uncertainty quantification in complex and large-scale biomechanical problems based on a Bayesian multi-fidelity scheme," *Biomech. Model. Mechanobiol.*, vol. 14, no. 3, pp. 489–513, 2015, doi: 10.1007/s10237-014-0618-0.

[104] A. Wittek *et al.*, "Cyclic three-dimensional wall motion of the human ascending and abdominal aorta characterized by time-resolved three-dimensional ultrasound speckle tracking," *Biomech. Model. Mechanobiol.*, vol. 15, no. 5, pp. 1375–1388, 2016, doi: 10.1007/s10237-016-0769-2.

[105] M. Peirlinck, M. De Beule, P. Segers, and N. Rebelo, "A modular inverse elastostatics approach to resolve the pressure-induced stress state for in vivo imaging based cardiovascular modeling," *J. Mech. Behav. Biomed. Mater.*, vol. 85, no. March, pp. 124–

133, 2018, doi: 10.1016/j.jmbbm.2018.05.032.

[106] D. C. Iliopoulos *et al.*, “Regional and directional variations in the mechanical properties of ascending thoracic aortic aneurysms,” *Med. Eng. Phys.*, vol. 31, no. 1, pp. 1–9, 2009, doi: 10.1016/j.medengphy.2008.03.002.

[107] A. N. Azadani *et al.*, “Comparison of mechanical properties of human ascending aorta and aortic sinuses,” *Ann. Thorac. Surg.*, vol. 93, no. 1, pp. 87–94, 2012, doi: 10.1016/j.athoracsur.2011.08.002.

[108] J. D. Humphrey, *Cardiovascular solid mechanics: cells, tissues, and organs.* New York, 2002.

[109] R. R. Davies *et al.*, “Yearly rupture or dissection rates for thoracic aortic aneurysms: Simple prediction based on size,” *Ann. Thorac. Surg.*, vol. 73, no. 1, pp. 17–28, 2002, doi: 10.1016/S0003-4975(01)03236-2.

[110] J. A. Elefteriades, “Natural history of thoracic aortic aneurysms: Indications for surgery, and surgical versus nonsurgical risks,” *Ann. Thorac. Surg.*, vol. 74, no. 5, 2002, doi: 10.1016/S0003-4975(02)04147-4.

[111] M. A. Coady, J. A. Rizzo, G. L. Hammond, G. S. Kopf, and J. A. Elefteriades, “Surgical intervention criteria for thoracic aortic aneurysms: A study of growth rates and complications,” *Ann. Thorac. Surg.*, vol. 67, no. 6, pp. 1922–1926, 1999, doi: 10.1016/S0003-4975(99)00431-2.

[112] E. Saliba and Y. Sia, “The ascending aortic aneurysm: When to intervene?,” *IJC Hear. Vasc.*, vol. 6, pp. 91–100, 2015, doi: 10.1016/j.ijcha.2015.01.009.

[113] E. M. Isselbacher, “Thoracic and abdominal aortic aneurysms,” *Circulation*, vol. 111, no. 6, pp. 816–828, 2005, doi: 10.1161/01.CIR.0000154569.08857.7A.

[114] C. M. García-Herrera *et al.*, “Mechanical behaviour and rupture of normal and pathological human ascending aortic wall,” *Med. Biol. Eng. Comput.*, vol. 50, no. 6, pp. 559–566, 2012, doi: 10.1007/s11517-012-0876-x.

[115] D. A. Vorp, B. J. Schiro, M. P. Ehrlich, T. S. Juvonen, M. A. Ergin, and B. P. Griffith, “Effect of aneurysm on the tensile strength and biomechanical behavior of the ascending thoracic aorta,” *Ann. Thorac. Surg.*, vol. 75, no. 4, pp. 1210–1214, 2003, doi: 10.1016/S0003-4975(02)04711-2.

[116] R. J. Okamoto, J. E. Wagenseil, W. R. DeLong, S. J. Peterson, N. T. Kouchoukos, and T. M. Sundt, “Mechanical properties of dilated human ascending aorta,” *Ann. Biomed. Eng.*, vol. 30, no. 5, pp. 624–635, 2002, doi: 10.1114/1.1484220.

[117] J. P. Vande Geest, M. S. Sacks, and D. A. Vorp, “The effects of aneurysm on the biaxial mechanical behavior of human abdominal aorta,” *J. Biomech.*, vol. 39, no. 7, pp. 1324–1334, 2006, doi: 10.1016/j.jbiomech.2005.03.003.

[118] A. Romo, P. Badel, A. Duprey, J. P. Favre, and S. Avril, “In vitro analysis of localized aneurysm rupture,” *J. Biomech.*, vol. 47, no. 3, pp. 607–616, 2014, doi: 10.1016/j.jbiomech.2013.12.012.

[119] N. Choudhury *et al.*, “Local mechanical and structural properties of healthy and diseased human ascending aorta tissue,” *Cardiovasc. Pathol.*, vol. 18, no. 2, pp. 83–91, 2009, doi: 10.1016/j.carpath.2008.01.001.

[120] J. P. Vande Geest, M. S. Sacks, and D. A. Vorp, “Age dependency of the biaxial biomechanical behavior of human abdominal aorta,” *J. Biomech. Eng.*, vol. 126, no. 6, pp. 815–822, 2004, doi: 10.1115/1.1824121.

[121] A. Duprey, O. Trabelsi, M. Vola, J. P. Favre, and S. Avril, “Biaxial rupture properties of ascending thoracic aortic aneurysms,” *Acta Biomater.*, vol. 42, pp. 273–285, 2016, doi: 10.1016/j.actbio.2016.06.028.

[122] S. Pasta, J. A. Phillippi, T. G. Gleason, and D. A. Vorp, “Effect of aneurysm on the mechanical dissection properties of the human ascending thoracic aorta,” *J. Thorac. Cardiovasc. Surg.*, vol. 143, no. 2, pp. 460–467, 2012, doi: 10.1016/j.jtcvs.2011.07.058.

[123] C. Noble *et al.*, “Controlled peel testing of a model tissue for diseased aorta,” *J. Biomech.*, vol. 49, no. 15, pp. 3667–3675, 2016, doi: 10.1016/j.jbiomech.2016.09.040.

[124] G. Sommer *et al.*, “Mechanical strength of aneurysmatic and dissected human thoracic aortas at different shear loading modes,” *J. Biomech.*, vol. 49, no. 12, pp. 2374–2382, 2016, doi: 10.1016/j.jbiomech.2016.02.042.

[125] J. D. Humphrey, “Continuum biomechanics of soft biological tissues,” *Proc. R. Soc. A Math. Phys. Eng. Sci.*, vol. 459, no. 2029, pp. 3–46, 2003, doi: 10.1098/rspa.2002.1060.

[126] A. Gefen, Ramat Aviv, and Israel, *Studies in Mechanobiology, Tissue Engineering and Biomaterials*, vol. 7. Ireland, 2011.

[127] A. Duprey, K. Khanafer, M. Schlicht, S. Avril, D. Williams, and R. Berguer, “In Vitro Characterisation of Physiological and Maximum Elastic Modulus of Ascending Thoracic Aortic Aneurysms Using Uniaxial Tensile Testing,” *Eur. J. Vasc. Endovasc. Surg.*, vol. 39,

no. 6, pp. 700–707, 2010, doi: 10.1016/j.ejvs.2010.02.015.

[128] M. P. Poullis, R. Warwick, A. Oo, and R. J. Poole, “Ascending aortic curvature as an independent risk factor for type A dissection, and ascending aortic aneurysm formation: a mathematical model,” *Eur. J. Cardio-thoracic Surg.*, vol. 33, no. 6, pp. 995–1001, 2008, doi: 10.1016/j.ejcts.2008.02.029.

[129] M. Liu, L. Liang, and W. Sun, “Estimation of in vivo mechanical properties of the aortic wall: A multi-resolution direct search approach,” *J. Mech. Behav. Biomed. Mater.*, vol. 77, no. August 2017, pp. 649–659, 2018, doi: 10.1016/j.jmbbm.2017.10.022.

[130] J. H. Kim, S. Avril, A. Duprey, and J. P. Favre, “Experimental characterization of rupture in human aortic aneurysms using a full-field measurement technique,” *Biomech. Model. Mechanobiol.*, vol. 11, no. 6, pp. 841–853, 2012, doi: 10.1007/s10237-011-0356-5.

[131] D. P. Nathan *et al.*, “Pathogenesis of acute aortic dissection: A finite element stress analysis,” *Ann. Thorac. Surg.*, vol. 91, no. 2, pp. 458–463, 2011, doi: 10.1016/j.athoracsur.2010.10.042.

[132] S. Pal, S., Tsamis, A., Pasta, S., D’Amore, A., Gleason, T. G., Vorp, D. A., and Maiti, “A mechanistic model on the role of ‘radially-running’ collagen fibers on dissection properties of human ascending thoracic aorta,” *J. Biomech.*, vol. 47, no. 5, pp. 981–988, 2014, doi: 10.1016/j.jbiomech.2014.01.005.A.

[133] J. S. Campa, R. M. Greenhalgh, and J. T. Powell, “Elastin degradation in abdominal aortic aneurysms,” *Atherosclerosis*, vol. 65, no. 1–2, pp. 13–21, 1987, doi:

10.1016/0021-9150(87)90003-7.

[134] A. J. Schriefl, H. Wolinski, P. Regitnig, S. D. Kohlwein, and G. A. Holzapfel, “An automated approach for three-dimensional quantification of fibrillar structures in optically cleared soft biological tissues,” 2013.

[135] A. J. Schriefl and G. A. Holzapfel, “Quantitative assessment of collagen fibre orientations from two-dimensional images of soft biological tissues,” no. July 2014, 2012, doi: 10.1098/rsif.2012.0339.

[136] G. A. Holzapfel, J. A. Niestrawska, R. W. Ogden, and A. J. R. and A. J. Schriefl1, “Modelling non-symmetric collagen fibre dispersion in arterial walls,” *J. R. Soc. Interface*, vol. 12, pp. 1275–1286, 2015, doi: http://dx.doi.org/10.1098/rsif.2015.0188.

[137] A. J. Schriefl, G. Zeindlinger, D. M. Pierce, P. Regitnig, and G. A. Holzapfel, “Determination of the layer-specific distributed collagen fibre orientations in human thoracic and abdominal aortas and common iliac arteries,” *J. R. Soc. Interface*, vol. 9, no. 71, pp. 1275–1286, 2012, doi: 10.1098/rsif.2011.0727.

[138] J. Schindelin *et al.*, “Fiji - an Open Source platform for biological image analysis,” vol. 9, no. 7, 2019, doi: 10.1038/nmeth.2019.Fiji.

[139] F. C. P. Yin, R. K. Strumpf, P. H. Chew, and S. L. Zeger, “Quantification of the mechanical properties of noncontracting canine myocardium under simultaneous biaxial loading,” *J. Biomech.*, vol. 20, no. 6, pp. 577–589, 1987, doi: 10.1016/0021-9290(87)90279-X.

[140] L. Azinfar, M. Ravanfar, Y. Wang, K. Zhang, D. Duan, and G. Yao, “High resolution imaging of the fibrous microstructure in bovine common carotid artery using optical

polarization tractography," *J. Biophotonics*, vol. 10, no. 2, pp. 231–241, 2017, doi: 10.1002/jbio.201500229.

[141] T. C. Gasser, S. Gallinetti, X. Xing, C. Forsell, J. Swedenborg, and J. Roy, "Spatial orientation of collagen fibers in the abdominal aortic aneurysm's wall and its relation to wall mechanics," *Acta Biomater.*, vol. 8, no. 8, pp. 3091–3103, 2012, doi: 10.1016/j.actbio.2012.04.044.

[142] D. Haskett, G. Johnson, A. Zhou, U. Utzinger, and J. Vande Geest, "Microstructural and biomechanical alterations of the human aorta as a function of age and location," *Biomech. Model. Mechanobiol.*, vol. 9, no. 6, pp. 725–736, 2010, doi: 10.1007/s10237-010-0209-7.

[143] A. N. Azadani *et al.*, "Biomechanical properties of human ascending thoracic aortic aneurysms," *Ann. Thorac. Surg.*, vol. 96, no. 1, pp. 50–58, 2013, doi: 10.1016/j.athoracsur.2013.03.094.

[144] J. E. Pichamuthu *et al.*, "Differential tensile strength and collagen composition in ascending aortic aneurysms by aortic valve phenotype," *Ann. Thorac. Surg.*, vol. 96, no. 6, pp. 2147–2154, 2013, doi: 10.1016/j.athoracsur.2013.07.001.

[145] J. F. Rodríguez, C. Ruiz, M. Doblaré, and G. A. Holzapfel, "Mechanical stresses in abdominal aortic aneurysms: Influence of diameter, asymmetry, and material anisotropy," *J. Biomech. Eng.*, vol. 130, no. 2, pp. 1–10, 2008, doi: 10.1115/1.2898830.

[146] J. R. Thunes, J. A. Phillippi, T. G. Gleason, D. A. Vorp, and S. Maiti, "Structural modeling reveals microstructure-strength relationship for human ascending thoracic aorta," *J.*

Biomech., vol. 71, pp. 84–93, 2018, doi: 10.1016/j.jbiomech.2018.01.037.

[147] A. Whelan *et al.*, "Collagen fibre orientation and dispersion govern ultimate tensile strength, stiffness and the fatigue performance of bovine pericardium," *J. Mech. Behav. Biomed. Mater.*, vol. 90, pp. 54–60, 2019, doi: 10.1016/j.jmbbm.2018.09.038.

[148] T. Shearer, "A new strain energy function for the hyperelastic modelling of ligaments and tendons based on fascicle microstructure," *J. Biomech.*, vol. 48, no. 2, pp. 290–297, 2015, doi: 10.1016/j.jbiomech.2014.11.031.

Website

World Heart Federation http://www.championadvocates.org/en/champion-advocates-programme/the-costs-of-CVD [Online] // World Heart Federation: Champion Advocates Programme. The costs of CVD.. - 2020.

Leica https://www.leica-microsystems.com/science-lab/topics/multiphoton-microscopy [Online].